MEASUREMENTS OF CHARGE RADII OF NEUTRON-DEFICIENT CALCIUM USING COLLINEAR LASER SPECTROSCOPY AT BECOLA

By

Andrew Jacob Miller

A DISSERTATION

Submitted to
Michigan State University
in partial fulfillment of the requirements
for the degree of

Physics - Doctor of Philosophy

2019

ProQuest Number: 22617044

All rights reserved

INFORMATION TO ALL USERS
The quality of this reproduction is dependent upon the quality of the copy submitted.

In the unlikely event that the author did not send a complete manuscript
and there are missing pages, these will be noted. Also, if material had to be removed,
a note will indicate the deletion.

ProQuest 22617044

Published by ProQuest LLC (2019). Copyright of the Dissertation is held by the Author.

All rights reserved.
This work is protected against unauthorized copying under Title 17, United States Code
Microform Edition © ProQuest LLC.

ProQuest LLC.
789 East Eisenhower Parkway
P.O. Box 1346
Ann Arbor, MI 48106 – 1346

ABSTRACT

MEASUREMENTS OF CHARGE RADII OF NEUTRON-DEFICIENT CALCIUM USING COLLINEAR LASER SPECTROSCOPY AT BECOLA

By

Andrew Jacob Miller

Calcium is a unique element, possessing two stable doubly-magic nuclei. Ca charge radii have been a challenge for nuclear theories to reproduce due to their unusual behavior. The chain of stable Ca isotopes spans from ^{40}Ca to ^{48}Ca, and although these differ by 8 neutrons, the nuclear charge radii are nearly identical. In addition to this peculiarity, there is a pronounced odd-even staggering in the charge radii, and an unexpected increase moving toward the neutron-rich isotopes. This work represents the first investigation of charge radii of these neutron-deficient calcium isotopes. Collinear laser spectroscopy (CLS) has been shown to be a valuable tool to investigate the fundamental properties of nuclei, such as nuclear spin, charge radii, magnetic dipole moments, and spectroscopic electric quadrupole moments. By probing the shift of the hyperfine spectra between isotopes, the nuclear charge radius can be extracted. In the case of non-zero nuclear and atomic spins, the nuclear magnetic dipole and electric quadrupole moment can also be obtained from the hyperfine splitting. In the present work, CLS was successfully performed on ^{36,37,38,39}Ca at the BEam COoler and LAser spectroscopy (BECOLA) facility at the National Superconducting Cyclotron Laboratory (NSCL) at Michigan State University. Improvements to the offline ion source and laser system, and a new photon detection system made it possible to study ^{36}Ca with only $\sim$50 ions/s despite the challenge of the short 102 ms half-life, the most sensitive measurement at BECOLA to date. First measurements were made of the charge radii of $^{36-38}$Ca, and the charge radius of ^{39}Ca is in agreement with previous results, while reducing uncertainty by a factor of 3. The charge

radii of these isotopes, especially the weakly-bound ^{36}Ca have required an advanced model of charge radii to understand the effects of loosely-bound protons on the pairing interaction, in the vicinity of the proton drip-line (^{35}Ca is the last bound calcium isotope). Despite the fact that the protons in these neutron-deficient systems are weakly-bound, the charge radii of $^{36-38}$Ca were found to be very compact and significantly smaller than predicted by previous theories. With Nuclear Density Functional Theory (DFT) using a novel Fayans interaction which contains novel nuclear-density gradient dependent surface and pairing terms, the complete chain of charge radii of $^{36-52}$Ca have now been reproduced and understood, and the DFT model best describing these new measurements on the neutron-deficient side also has improved agreement with data on the neutron-rich side.

Copyright by
ANDREW JACOB MILLER
2019

Dedicated to my wife, Elizabeth Claire Miller

ACKNOWLEDGMENTS

This dissertation could not be complete without thanking the many students, scientists, and family members who have helped me along the way.

I would like to thank all the members of the BECOLA group, especially my advisor Kei Minamisono. Thank you for your example in the lab, promoting safety, inviting questions, and being open to new ideas and improvements, even during online experiments. I must thank Dominic Rossi and Caleb Ryder who helped introduce me to the BECOLA system. Each of them spent many hours helping me align the laser system and learn to perform the data analysis. Other members of the BECOLA group, including David Garand, Jeremy Lantis, Skyy Pineda, and Robert Powel, thank you all for making our time working together both enjoyable and productive.

Thanks to the experimenters who traveled from near and far to help, especially the spokesperson of this experiment, Andrew Klose. I am also particularly grateful to those who helped design, manufacture, and install the new photon detection system used in this experiment: Bernhard Maaß, Wilfried Nörtershäuser, and Jacob Watkins. This experiment would not have been possible without the help of Chandana Sumithrarachchi and the others in the gas cell group working to provide the best beams possible to BECOLA. Others who helped make this experiment a success are Yuan Liu, Felix Sommer, and Andrea Tiegelhöfer.

Without the input from theorists, this work would never have had such an impact, so I would like to thank Witek Nazarewicz and Paul-Gerhard Reinhard for their invaluable contributions to the discussion and interpretation of the charge radii results and Alex Brown for his contributions regarding the nuclear moments.

Thank you to those who spent their time and energy serving on my committee: Kei

Minamisono, Matt Comstock, Paul Mantica, Witek Nazarewicz, and Jaideep Singh. Your comments and questions helped me progress smoothly through my time here, and your interest in my research and my success are greatly appreciated.

I would also like to thank my fellow students, especially those who spent long hours working through homework with me, playing video games, and throwing birthday parties in our office. Lisa Carpenter, Dennis Foren, Alicia Palmisano, Roy Ready, Zac Tilocco, and many others were always willing to join me in studying or relaxing.

Thank you to the many professors I had the privilege of learning from, both at Michigan State University and my *alma mater*, Abilene Christian University.

In addition to my academic comrades and mentors, I must also thank my family for their support. Thank you to my parents for dedicating so much of their time and efforts to my brothers and me through homeschooling. Although many people reminisce about their favorite gradeschool teacher, I am blessed to say that I had my favorite teachers with me every year, from preschool through high school, not to mention the phenomenal field trips we went on. Your hard work has allowed me to reach where I am today both academically and spiritually, and I cannot thank you enough for all of your continued sacrifices. Thank you to my brothers for your encouragement and support, even as you each continue with your own amazing achievements in the arts.

Most importantly, I thank my wife and son. Thank you for following me across the country for school and work, and for demonstrating how exciting learning new things can be. Thank you for going through life by my side, encouraging me, and keeping me focused on what really matters. Without your love and support, this would not have been possible.

There are many others, including family members, fellow students, and teachers who I don't have space to thank here by name. Thank you all for your support.

TABLE OF CONTENTS

LIST OF TABLES . . . . **x**

LIST OF FIGURES . . . . **xiii**

KEY TO ABBREVIATIONS . . . . **xxiv**

Chapter 1 Introduction **1**
- 1.1 Charge radii 2
- 1.2 Calcium 5
- 1.3 Collinear Laser Spectroscopy at BECOLA 8
- 1.4 Dissertation overview 9

Chapter 2 Experiment **11**
- 2.1 Basic principles 11
  - 2.1.1 Atomic transition 14
  - 2.1.2 Laser system 15
  - 2.1.3 Hyperfine interaction 17
  - 2.1.4 Bunched beam background suppression 20
  - 2.1.5 Doppler-shift 23
- 2.2 Isotope production 28
  - 2.2.1 Rare isotopes 28
- 2.3 System upgrades 31
  - 2.3.1 Reference isotopes 32
    - 2.3.1.1 PIG source upgrades 33
    - 2.3.1.2 Isotopic limitations 34
  - 2.3.2 Photon detection system 35
    - 2.3.2.1 Motivation 36
    - 2.3.2.2 Performance Studies 37

Chapter 3 Analysis **43**
- 3.1 Calibration 43
- 3.2 Hyperfine Spectra 45
  - 3.2.1 Fitting Function 45
  - 3.2.2 Fitting Procedure 47
    - 3.2.2.1 Hyperfine coupling constants 47
  - 3.2.3 Results 48
- 3.3 Nuclear Moments 49
- 3.4 Charge radii 53
  - 3.4.1 Isotope shift 53
  - 3.4.2 King plot 55

3.4.3 Results 58

Chapter 4 Discussion 61
4.1 Modeling charge radii 61
4.2 Empirical extrapolation 68

Chapter 5 Conclusion 72

APPENDICES 75
APPENDIX A Hardware 76
APPENDIX B Software tools 107
APPENDIX C Personal contributions 112

REFERENCES 116

LIST OF TABLES

Table 2.1: The set laser frequency and scanning voltage used for each measurement. The set laser frequency is the wavenumber of the Ti:Sapphire laser prior to the frequency doubler, while the scanning region indicates the range of the scanning potential applied to the detection region as the spectra were recorded. 29

Table 2.2: The half-life ($T_{1/2}$), bunching period (T_b), rates at the cooler/buncher for the rare isotopes, and the total measurement time used for each isotope. The bunching repetition rates for ^{36,37}Ca were chosen based on the short half-lives, while the bunching periods of ^{38,39}Ca were affected by the high ion rates and the space-charge limitations of the trap. Because the reference isotopes ^{40,44}Ca can be produced with high ion currents, they have different limitations, which are discussed in Section 2.3.1.2. 31

Table 3.1: The obtained hyperfine coupling constants of ^{37,39}Ca for the $4s\ ^2S_{1/2}$ and $4s\ ^2P_{3/2}$ states. The statistical and systematic uncertainties are reported in the first and second parentheses, respectively. The systematic uncertainty comes from the high voltage calibration, and also the deviation of the A^{hf}-factor ratio measured for ^{39}Ca from the literature value from ^{43}Ca. This unexplained discrepancy is the dominant source of systematic error. 49

Table 3.2: The nuclear moments of ^{37,39}Ca obtained in this work. The total uncertainty is reported in the parentheses. $Q(^{39}\mathrm{Ca})$ is in agreement with the previous experimental value of $3.6(7)\,e^2\mathrm{fm}^2$ [56], although the sign of $Q(^{39}\mathrm{Ca})$ is experimentally determined here for the first time. $\mu(^{39}\mathrm{Ca})$ reported here does not take into account the hf anomaly, which the previous and more precise β-NMR measurement, $+1.0217(1)\,\mu_N$ [57], is insensitive to. For more discussion of these results, see ref. [37]. 53

Table 3.3: Isotope shifts, deduced differential mean-square charge radii, and absolute charge radii. The numbers in parentheses are the statistical and systematic uncertainties, respectively. The differential ms charge radius of ^{39}Ca relative to ^{40}Ca is consistent with the previous value of $-0.127(20)\,\mathrm{fm}^2$ [64]. Rms charge radii were obtained using the charge radius of ^{40}Ca 3.4776(19) fm from ref. [4]. 59

Table 3.4: Sources of uncertainty in the differential ms charge radii, $\delta\langle r^2\rangle^{40,A}$. Statistical uncertainty comes from the fit of the spectra. The calibration uncertainty is from the fluctuations in the extracted calibration voltage, described in Section 3.1. Atomic factor uncertainty is due to the total uncertainty from the atomic factors, k and F as noted in Equations 3.13 and 3.14. 59

Table A.1: The design of the new PDS was compared to the existing system using simulations within FRED, a ray-tracing tool. Signal photons were simulated using rays emitted in all directions from random points within the volume of a cylinder, approximating the overlapping laser and ion beam. Background photons were approximated by rays originating from random points within a circle, and emanating in a random direction in the hemisphere facing the PDS. For the old system, this background source was simulated in two different positions (see Section A.1.1) leading to the ranges of background acceptance and SNR. Both systems were simulated with perfect reflectance. The fraction of signal and background reaching the detector were compared to several actual measurements using reference ions and the existing system, in order to determine the appropriate ratio of incoming signal and background photons. The SNR in the table are extrapolated from the simulations and these reference measurements, assigning the measurement from the existing system an SNR of 1. Due to the fact that the ^{56}Fe measurement requires the charge-exchange cell, there is an additional background source coming from the ion beam itself, which is collected in the same way as the signal. Because of this, the strategy employed by the new system, to minimize noise even at the cost of some signal, is not as effective, due to the fact that the noise from the charge-exchange process cannot be reduced this way. . . . 86

Table A.2: These channels are used to control the DVMs. Identical channels exist for `MTER_N0002`. `V_RD` is the channel where the voltage is actually displayed. `POLL_TXT` is the SCPI message sent to poll the device. Using a command other than the one shown here may inadvertently reset the measurement settings on the device. `V_RD.SCAN` is used to determine how often the voltage is read. `RST_CMD` must be set to `1` each time the DVM is power cycled, in order to run the `RST_TXT` commands. The `SCPI` channels can be used to send commands and queries to the DVM, if a query is sent the response is shown in the reply channel. The commands in the `RST_TXT` channels here reset the DVM, then configure the voltage range and precision, and finally enable the high impedance mode. Note that a higher precision and thus slower polling rate is used for the FuG, while a lower precision and faster polling rate is used for the Matsusada. For more details on the SCPI commands which are recognized by the DVMs, see the SCPI programming guide from Agilent. 102

LIST OF FIGURES

Figure 1.1: Figure modified from [16] highlighting nuclides which have been measured using optical spectroscopy. The nuclides are positioned with neutron number increasing toward the right, and proton number increasing vertically. Stable nuclei are highlighted in black, while blue squares indicate rare isotopes which have measurements from optical spectroscopy. Boxes in magenta indicate the rare isotopes which have been measured at BECOLA. The ability of spectroscopy to gain nuclear information from across all mass ranges and reach short lived isotopes far from stability is evident. For interpretation of the references to color in this and all other figures, the reader is referred to the electronic version of this thesis. 3

Figure 1.2: Single-particle levels of nucleons calculated from the nuclear shell model. On the left side are the energy states, and towards the right, the splitting from the spin-orbit interaction is included. The occupancy of these levels is noted above each. At shell closures where large gaps occur between one level and the next, magic numbers are observed. When moving away from stability, these levels shift, leading to the development of new magic numbers, and disappearance of others. 4

Figure 1.3: Examples of charge radii from Ne to Kr isotopes. Experimental data is from [4]. Neutron magic numbers are indicated by vertical dashed lines. A local minimum can be observed in many chains for $N = 28$ and $N = 50$, however this signature is not observed across $N = 20$. 6

Figure 1.4: Experimental calcium charge radii prior to this work. Stable and long-lived isotopes are plotted in black, while unstable isotopes are plotted in red. Data taken from [4, 26]. The parabolic shape between $A = 40$ and $A = 48$, odd even staggering, and the dramatic rise beyond $A = 48$ have been difficult for theories to reproduce [23, 24, 25, 21, 26, 27]. 7

Figure 2.1: The rare isotope production at the NSCL. For this experiment, stable ^{40}Ca were generated and then accelerated to 140 MeV/nucleon using the coupled cyclotrons, K500 and K1200. Following this acceleration, the beam was impinged on a beryllium target. A wide range of isotopes was produced, and these isotopes were then passed through the A1900 fragment separator, in order to select those of interest. Following this schematic, the fast beams (0.5 c) were passed to the gas cell, where the beam is thermalized. 12

Figure 2.2: The gas stopping layout at the NSCL. Fast beams of rare isotopes are brought in from the left and are introduced to the gas cell, following a solid degrader. The ions are then thermalized in the helium buffer gas. On extraction from the gas cell, the desired charge/mass ratio can be selected using a dipole magnet. The low energy beam is then transported to the BECOLA facility, where collinear laser spectroscopy is performed. 12

Figure 2.3: The collinear laser spectroscopy setup at BECOLA. Above is a cartoon showing the beam path of the laser and the ion beams. The radio-frequency quadrupole (RFQ) cooler/buncher is able to accept the beam from either the PIG offline source, or the radioactive "online" beam coming from the gas cell. As shown, the voltage at the detection region is scanned in order to scan the transition energy being probed, and the two photon detection systems collect the resonant photons. Below, a more true to life diagram is pictured, in order to give an accurate sense of scale. 13

Figure 2.4: Atomic states, and hyperfine splitting. On the left, the electronic levels for Ca II are drawn [41]. On the right, the selected transition is drawn, along with the hf splitting for $I = 3/2$, as in ^{37,39}Ca [42]. The allowed hf transitions are marked in red. 16

Figure 2.5: The laser setup used in this experiment. The Sirah Matisse TS Ti:Sapphire laser was frequency locked using the stabilized He-Ne and the wavelength meter, by sampling 1 % of the light as shown. The majority of this light was frequency doubled, and transported to the experimental area using a fiber optic cable. Here, after passing through a polarizing cube, 10 % of the light was sampled by a power meter in order to control the LPC, which modulated the power entering the frequency doubler. This allowed power fluctuations introduced by the transmission through the fiber to be eliminated, and ensure a stable 300 µW beam for CLS. 17

Figure 2.6: The recorded time spectra for the ^{36}Ca and ^{44}Ca bunched beams. ^{36}Ca had the fewest ions contained in each bunch, thus giving the narrowest time-width, while ^{44}Ca had the most ions per bunch, due to contamination from the more abundant ^{40}Ca (see Section 2.3.1.2), leading to a slightly wider peak in time. The ^{36}Ca time-spectrum is taken from the full 33 h running time with that isotope, while the ^{44}Ca time-spectrum is taken from a single reference measurement of < 1 h. Other isotopes measured in this experiment fall within these two extremes, with a time-width of approximately 1 µs. 21

Figure 2.7: Above is a schematic of the cooler/buncher used at BECOLA. A unique aspect of this design is the separate cooling and bunching sections, which are operated with different buffer gas pressures. The differential pumping scheme used to maintain the central high-pressure region can be seen in Figure 2.8. The ions are contained laterally by the pseudo-potential of a radio-frequency quadrupole (RFQ), while a drag potential is maintained in the longitudinal direction using segmented electrodes. The graph below the schematic shows the drag and trapping potential along the beam axis, the dashed line on the right indicates the potential used to release the ion bunch. Figure from ref. [44]. 23

Figure 2.8: Illustration of the differential pumping channel. The high and low pressure regions are connected via a narrow channel with relatively low conductance (marked "C"). The helium is introduced into the high pressure region, and pumped from the low pressure region using a turbomolecular pump (marked "S_{TMP}"). Figure from ref. [44]. . 24

Figure 2.9: The bunching efficiency as a function of cooling time. As shown by the black squares, with small quantities of ions there is minimal reduction in efficiency for holding times up to one second. These measurements were made using potassium ions. Figure from ref. [45]. 25

Figure 2.10: A plot showing the effect that the bunching period, T_b, has on the signal and noise collected when using unstable isotopes, assuming that the efficiency of the cooler is unaffected by the bunching period, and that the measurement time for each bunch is 1 µs regardless of the holding period. The vertical axis represents the noise and signal counts collected after a given time (see Equations 2.8 and 2.9), and their ratio (Equation 2.11). No units are provided on the vertical axis, as the absolute quantities also depend on other factors, such as the half-life, incoming beam rates, and the measurement time of the bunch. The signal counts are shown in blue, noise counts in red, and SNR (scaled arbitrarily) is shown in black. As the period is increased, the ions held in the trap, and thus the signal per bunch, will eventually plateau, however, the increased time between bunches leads to a continued reduction in signal collected. The noise collected from the laser is also reduced due to the decrease in total background caused by measuring the data in fewer bunches. Although both signal and noise are monotonically decreasing, the drastic reduction in noise causes the SNR to be maximized when $T_b \approx 1.8 \times T_{1/2}$. 26

Figure 2.11: This plot highlights the benefits of an in-flight measurement with regard to Doppler-broadening. For a given temperature of ions, there will be a small spread in kinetic energy, leading to a spread in velocity (black bands). When the ions are accelerated over a large potential, although the energy spread remains the same (and is small compared to the energy following acceleration), the corresponding velocity spread is reduced (red bands). Because the velocity determines the effective frequency of the laser light that the ions are interacting with, this velocity bunching results in narrower resonance peaks. . . 27

Figure 2.12: Experimental data from the gas cell group showing the mass-to-charge spectrum of ^{39}Ca extraction from the gas cell. The horizontal axis shows the selected mass/charge ratio (amu/e), while the vertical axis indicates the decay rate seen in the extracted beam. The peak at 39 is attributed to singly-charged ^{39}Ca ions, while the peak at 19.5 contains the doubly-charged ions of this species. At $m/q = 57$, a peak can also be seen due to singly-charged ^{39}Ca with a single water molecule (18 amu) attached. This spectrum was taken using 400 V for the dissociation potential. As shown, this results in a significant portion of singly-ionized ^{39}Ca which was then transported to BECOLA to perform spectroscopy. 30

Figure 2.13: Renderings of both the old and new systems. The PMT of the old system is placed at the focal point of the ellipsoidal reflector. The new system image has two complete photon detection regions, each with their own elliptical reflector, aperture, CPC and PMT. To enable a better view of the design, the detection region closest to the viewer has had two pieces removed from both the elliptical reflector and the CPC (green). The detection region further from the viewer has had the CPC and PMT removed to allow a view of the adjustable aperture (dark blue) which sits just outside the window. Four rods support the two regions, and are held inside the beam pipe using four adjustable insulating feet on each end (cyan), in order to allow the scanning potential to be applied to the PDS. 37

Figure 2.14: SNR results using various opening widths at the focal plane. The vertical axis is the SNR of the first detection region of the new system, normalized using the second detection region of the new system with the adjustable plates open as wide as possible. It was expected that the signal would be concentrated at the center of the focal plane, meaning that there would be a point where the SNR begins to decrease, as any wider opening only serves to allow more stray photons into the system. As shown, this was not the case. The wider the opening, the better the SNR becomes. 39

Figure 2.15: Results examining the SNR at various points along the Y-axis of the focal plane. The plates in one detection system were set to a 3 mm wide slit, and a calcium resonance was recorded with this slit at various positions along the Y-axis of the focal plane. The vertical axis is the SNR of the system being scanned, divided by the SNR of the control system. Red circles show the normalized SNR (compared to the other detection system which was used as a control), while the gray dotted line indicates the shape expected from the simulation. Rather than observing the signal concentrated into a single peak (see Figure A.3), the highest SNR was observed in two peaks on either side of the center. Further simulations to explore this behavior can be found in Section A.1.3. 40

Figure 2.16: SNR results using various masks to select the two peaks seen at the focal plane. The vertical axis is the SNR of the new system, divided by the SNR recorded with the old system. The mask used for each measurement is shown underneath the plot, gray areas are where the focal plane was blocked, while white areas show the region of the focal plane where light was allowed to pass through the window. While the adjustable plates were used to block the top and bottom, a 5 mm or 15 mm wide strip of anodized foil was used to block the central portion. The focal plane is labeled along the X and Y axes with units of mm. Selecting the two regions of peak intensity seen in Figure 2.15 does provide a better SNR, but in all cases, even with the focal plane fully open, the SNR was more than that obtained using the old system. 41

Figure 3.1: The spectrum measured for ^{36}Ca, along with the residuals from the fit using a pseudo-Voigt function as described in Section 3.2. 50

Figure 3.2: The hyperfine spectrum measured for ^{37}Ca, along with the residuals from the fit using six pseudo-Voigt functions as described in Section 3.2. 50

Figure 3.3: The spectrum measured for ^{38}Ca, along with the residuals from the fit using a pseudo-Voigt function as described in Section 3.2. 51

Figure 3.4: The hyperfine spectrum measured for ^{39}Ca, along with the residuals from the fit using six pseudo-Voigt functions as described in Section 3.2. 51

Figure 3.5: A typical spectrum measured for the reference ^{40}Ca, along with the residuals from the fit using a pseudo-Voigt function as described in Section 3.2. 52

Figure 3.6: A typical spectrum measured for the calibration ^{44}Ca, along with the residuals from the fit using a pseudo-Voigt function as described in Section 3.2. 52

Figure 3.7: Diagram from ref. [22] describing the mass shift and field shift principle. The left panel shows the mass shift. At the top, is a representation of the normal mass shift (NMS) which arises from the balance of momentum between the nucleus and each electron, while the middle and lower diagrams depict the specific mass shift (SMS) which varies depending on the momentum correlation between the electrons in the atomic system. The center panel describes the field shift. A pure Coulomb potential for a point-like nucleus is shown by the dotted line. Variations in the charge volume of the nucleus affect the energy levels of the electrons due to the probability of the electrons being within the nucleus. The horizontal dotted line represents the energy of an s-electron for a point-like nucleus, while the red and blue levels on the left and right show the energy levels shifted due to the volume of the nucleus A' and A respectively. The right section provides an idea of the relative contribution to the isotope shift of each effect, versus the atomic number. As the field shift is the component sensitive to the charge-radius, the charge radius becomes difficult to extract for lighter isotopes, where the mass shift dominates. 56

Figure 3.8: King plot from ref. [59] comparing the modified isotope shift of the D1 and D2 transitions in Ca. Previous data points are shown in red, while the blue circles are those measured in that work. Both the vertical and horizontal axes are plotting the "modified" isotope shift, which is the left hand side of Equation 3.12. Here μ represents the expression involving the masses. The high degree of precision and the excellent linearity of the points gives good cause to neglect higher order effects which may cause F to vary between isotopes. 57

Figure 4.1: The charge radii measured in this work (red squares) and previous experimental values (black squares) are compared to DFT predictions of SV-min (HFB), Fy(Δr,BCS), Fy(Δr,HFB), and Fy(Δr^*,HFB) models. The values of Fy(Δr^*,HFB) for $A > 37$ are very close to Fy(Δr,HFB) results; hence, they are not shown. The rms. charge radii were obtained using the known charge radius of ^{40}Ca (ref. [4]), and its error has been incorporated into the systematic uncertainty (the gray band). These values are shown in Table 3.3. 63

Figure 4.2: Graphs showing the energy levels, radii, and occupations of the single proton states in the Ca chain. The upper graph, a), highlights the weakly-bound nature of the valence protons. As shown by the red triangles, the single proton energy of the $0f_{7/2}$ orbital rises above the Coulomb barrier and becomes unbound in the case of $^{36-38}$Ca. Graphs b) and c) display the single-proton rms radii and occupations, respectively. In the case of the Fy(Δr,BCS) approach, the single-proton radius increases in a non-physical way as the states rise above the Fermi energy and continuum effects come into play (red diamonds). With a realistic pairing interaction, these unbound states do not grow so dramatically in size, as shown by the Fy(Δr,HFB) and Fy(Δr^*,HFB) points (green circles and blue triangles). 65

Figure 4.3: Nuclear charge radii of cadmium isotopes. Figure taken from reference [73]. Experimental values and several models are shown. The gray band represents the systematic uncertainty of the experimental values, arising from the uncertainty of the field-shift constant. The inset also shows the corresponding one-neutron separation energies. The agreement of the Fayans functional is quite good, although some overestimation of the odd-even staggering is present here as well. . 66

Figure 4.4: Nuclear charge radii of tin isotopes. Figure taken from reference [74]. Experimental values and several models are shown. The inset also shows the behavior of the Fy(Δr,HFB) model in the vicinity of ^{208}Pb. The ability of this Fayans functional to reproduce these kink-structures in heavy isotopes without additional tuning is quite remarkable. . . 67

Figure 4.5: Figure from reference [75]. This figure shows the relative locations of the nuclides used in the four empirical charge radii relationships. In all four cases, $\delta R_{in-jp} = R(1) + R(2) - R(3) - R(4) = 0$, allowing the prediction of a charge radius from the other three. This relationship is most robust for (a), where there is only a step of 1 proton or neutron between the four nuclides being compared, but holds reasonably well for the other three relationships as well. 69

Figure 4.6: Empirical predictions of charge radii shown here in purple diamonds are taken from reference [75]. These predictions use some combinations of the four relations shown in Figure 4.5. Experimental charge radii are shown using the red and black squares. Large deviations from the empirical predictions can suggest sudden variations in shape or density of the nucleus. It is interesting to note that while previous theories dramatically over predicted the size of the proton-rich nuclei in this chain, these empirical predictions are reasonably accurate, and in fact under predict nuclei below $A = 40$, which is to be expected considering the effect of the weakly-bound protons in these isotopes. This highlights the fact that there is no sudden change of behavior of the charge radii in this region, and strengthens the belief that a model which performs well in this chain may be applicable across the nuclear chart. 71

Figure A.1: Schematic showing the three simulation setups. Raytracing simulations were performed in FRED using perfectly reflective surfaces. The new system was simulated with a cylindrical volume emitting rays in random directions, while the background was simulated as rays emitted in random directions from within the area of a circle placed at the entrance to the elliptical region. The old system was simulated twice, once with the sources positioned identically to the new system, shown on the right, and again with the background source moved closer to be flush with the system, as shown on the left. These two simulations of the old system were used to evaluate the stability of the simulations and obtain a range of expected values. 78

Figure A.2: Simulation showing the geometric distribution of photons arriving at the focal plane using the existing PDS. The blue dashed circle indicates the geometric acceptance of the PMT, collecting the majority of the signal (red points), and excluding a portion of the background (yellow points). In this simulation, 44.8 % of the signal photons reach the focal plane, while 25–40 % of the background photons simulated arrive at the focal plane. In the area covered by the PMT, 13.4 % of the signal, and 1.5–2.6 % of the background were collected. The range of values for the background are due to a variation in the position of the simulated background source as described in Section A.1.1. . . 79

Figure A.3: Simulation showing the geometric distribution of photons arriving at the focal plane (left) and the PMT (right) with the new PDS. The blue dashed line indicates the geometric cutoff of the aperture at the focal plane, collecting the majority of the signal (red points), and excluding a portion of the background (yellow points). In this simulation, 42.9 % of the signal photons pass through the aperture of the focal plane, compared to only 15.3 % of the background photons. Following the CPC, the PMT accepts 8.3 % of the signal, and only 0.21 % of the background photons. 80

Figure A.4: Simulation results describing the angular distribution of photons arriving at the focal plane of the new PDS. Signal is shown in red, and background in yellow. The polar angle of 0° corresponds to the perimeter of the hemisphere, while an azimuthal angle of 0° or ±180° corresponds to the beam axis. The angular distribution is also shown projected onto a hemisphere above each graph, the center of the hemisphere faces the PMT. The blue dashed line indicates the angular cutoff chosen for the CPC. Photons arriving with a polar angle less than 70° are rejected excluding a large part of the background . . . 81

Figure A.5: Simulation results describing the angular distribution of photons arriving at the focal plane of the old PDS. Signal is shown in red, and background in yellow. The polar angle of 0° corresponds to the perimeter of the hemisphere, while an azimuthal angle of 0° or ±180° corresponds to the beam axis. The angular distribution is also shown projected onto a hemisphere above each graph, the center of the hemisphere faces the PMT. As shown, the primary intensity of both the signal and background lie at the same polar angle, preventing any improvement from adding a CPC to the existing system. 82

Figure A.6: This simulation highlights the difference in signal collection of the two systems. While the old system collects a large fraction of the signal at the center of the detection region (the focus of the ellipsoid), the new system collects signal more consistently across the entire region. The total acceptance of the new system (area under this curve) is still less than the old system, however, the increase in noise rejection allows it to outperform the old system for the Ca II measurement. . 83

Figure A.7: A schematic of the beampipe used to enclose the two new detection regions. The 8 in flanges on the top and bottom, which are offset from one another, are the location of the two new detection regions. A small flange opposite each allows a high voltage feedthrough in order to apply the scanning potential to the detection region, as shown in Figure A.12. 87

Figure A.8: Reflection data for the aluminum sheeting used for the reflective surfaces of the new PDS. The MIRO 4300UP was used, in order to allow for good reflectivity throughout the UV range (250–450 nm). 88

Figure A.9: Looking from the end of the beam cross, the internal supports of the PDS are shown. Four white insulating feet support it within the beam pipe, and the four main support rods are pointing away from the viewer, from the ends of the aluminum × in the center of the beam pipe. The small tube at the center of the × is where the laser and ion beams travel. Alignment of this main frame was accomplished by rotating the double-threaded brass connectors next to the insulators. 89

Figure A.10: Photographs showing the assembly of an elliptical reflector. On the top, the parts are shown prior to assembly. The left image shows the assembly minus one side plate, and the end plate. When the end plate is attached, it pushes the reflective sheet in flush with the end of the elliptical plates, causing it to bow further outward and lay flat against the elliptical plates. The right photo shows the final assembly, looking in through the window of the end plate. Not shown here is the metal mesh which covers this window in order to ensure that the entire detection region is enclosed by the desired potential when scanning. 90

Figure A.11: Photographs showing how the elliptical reflectors are attached to the support rods. On the left the interior of the beam pipe is shown. A small “J” shaped hook holds the elliptical reflector assembly up against the support rods. It is locked in place with a set screw on the side facing out the side flange, and so it can be accessed from outside with careful use of tweezers and a long hex wrench, as shown in the photo on the right. 91

Figure A.12: Photographs showing the installation of the high voltage feedthrough used for the scanning potential. A small spring allows contact with the back of one of the elliptical reflectors. The left photo shows the high voltage conductor in contact with the system, while the right shows the feedthrough removed from the system. 91

Figure A.13: A photograph of the CPC assembly. Two halves of one CPC are shown in the foreground, while in the back, a fully assembled CPC can be seen. The wide side attaches to the side window of the beam pipe, and the PMT is attached to the narrow end. 92

Figure A.14: A photograph showing the assembly of the exterior components of the PDS. An adjustable aperture of aluminum plates is attached to the window, with the CPC following. At the right end of the CPC, the mounting hardware for a PMT is shown. The face of the PMT presses up against a rubber O-ring on the CPC, while the back end is held tightly using a plate held by threaded rods protruding from the CPC. 92

Figure A.16: Photograph of the MFC and surrounding components. The open 9-pin connector seen on the "T" connector can be attached to a computer via an RS232 serial cable when the system is not on high voltage. The insulator is necessary to prevent current leakage when the PIG source is raised on the high voltage. Originally, the bent aluminum bracket was thought to be sufficient, however there was an excessive amount of leakage current when the MFC was connected there directly. When not operating the PIG source, the shutoff valve can be closed to allow a better vacuum in the PIG source. 97

Figure A.17: Schematic showing the wiring of the custom "T" connector being used for the MFC. The diagram is taken from the manual provided by Bronkhorst, and color labels are added to indicate the actual wires used within the connector. The left side of this figure connects to the MFC, and the connection on the lower right allows for power and analog controls to be attached. The upper right connector is used for serial communication with a PC, and is not usually connected. . . . 98

Figure A.18: Data taken using doubly-charged ^{40}Ca ions. The cooler/buncher was set to allow doubly-charged ^{40}Ca ions to pass through, and singly-charged ions were rejected (verified using spectroscopy). As the CEC temperature was increased, ion beam currents were measured after the CEC with and without the ion kicker. By measuring the total current from the doubly-charged ion beam prior to the CEC, assuming a total transmission through the CEC of 98 %, and measuring the neutral and charged beam current, the fraction of atoms in each charge state can be determined. While this method is not very precise, it does show that the cross section for the double and single charge exchange process increases with temperature. 101

Figure A.19: Photograph of the Raspberry Pi 3B+ and its connections used to interface with the waveform generator. This is in the rack inside the high voltage cage. Rather than connect the waveform generator directly to the Pi, a USB hub must be placed in between, otherwise the Pi does not recognize the device. 105

KEY TO ABBREVIATIONS

- BCS - Bardeen-Cooper-Schrieffer
- BECOLA - BEam COoler and LAser spectroscopy
- CLS - collinear laser spectroscopy
- DVM - digital volt-meter
- FC - Faraday cup
- FS - field shift
- FRIB - Facility for Rare Isotope Beams
- FWHM - full-width at the half-maximum
- hf - hyperfine
- HF - Hartree-Fock
- HFB - Hartree-Fock-Bogolyubov
- IS - isotope shift
- KE - kinetic energy
- LPC - laser power controller
- ms - mean-square
- MS - mass shift
- NSCL - National Superconducting Cyclotron Laboratory (East Lansing, MI, USA)
- PDS - photon detection system
- PIG - Penning ionization gauge
- PMT - photo-multiplier tube
- RFQ - radio frequency quadrupole
- rms - root mean-square
- SNR - signal-to-noise ratio
- UV - ultra-violet
- β-NMR - β-ray detecting nuclear magnetic resonance

Chapter 1

Introduction

Since the discovery of the nucleus over a century ago [1], experiments have been investigating the size and shape of all kinds of nuclei [2, 3, 4]. Measurements of global properties of nuclei, such as the charge radius, magnetic dipole moment, and electric quadrupole moment have brought new insights to the behavior of the nuclear force and the complex interactions of protons and neutrons within the nucleus [5, 6]. These experimental results are especially useful when they extend our knowledge to unstable nuclei, towards the proton or neutron dripline, because they can reveal evolutions in nuclear shell structure which may not exist in the region of stable nuclides.

One method of studying rare isotopes is Collinear Laser Spectroscopy (CLS). This technique enables a very precise measurement of the atomic hyperfine (hf) structure, which can be affected by variations in the nucleus' size and shape. A major advantage of this technique is the ease of application to exotic isotopes, due to in-flight measurement using a fast beam [7]. While collinear laser spectroscopy has been in use for over forty years [8], the technique has seen major advancements in the 21st century due to the pioneering of the bunched-beam technique (a time-resolved fluorescence measurement) [9]. This has dramatically enhanced the sensitivity, and in recent years, bunched-beam CLS has enabled measurements of charge radii and nuclear moments of an expanding group of rare isotopes as production capabilities have increased [10, 11].

From a precise measurement of an atomic hf transition, this technique allows the extraction of charge radii and nuclear moments of rare isotopes, and has been used with great success for nuclei across the entire nuclear chart, as shown in Figure 1.1 [12, 13, 14, 15, 16]. These observables can give indications of the nuclear structure, including highlighting the so called “magic numbers” where nuclei are observed to be particularly well bound, due to gaps in the nucleon single-particle energy levels, or shells, shown in Figure 1.2. Moving away from stability, variations in the nuclear single-particle energy levels can give rise to new magic numbers [17], and several unstable calcium isotopes have been predicted to show characteristics of these new shell closures [18].

1.1 Charge radii

One of the most important properties of the nucleus is its size. Indeed, the remarkably small charge radius of the nucleus compared to the atomic radius was the first experimental observation of the nucleus, before even understanding its constituents [1]. To this day, measurements of nuclear charge radii continue to be an important tool to inform and confirm nuclear theories [19].

From scattering experiments, it is found that, in general, the charge density of the nucleus is approximately constant. This leads to a simple relation between the radius, r, and the number of nucleons, A:

$$r = r_0 A^{1/3} \tag{1.1}$$

where r_0 has been found empirically to be approximately 1.2 fm [20]. While this can serve as a rough estimation for the charge radii of heavier nuclei, the deviations from this general trend provide insights into the underlying structure of the nucleus.

When looking at the variations in charge radii across a chain of isotopes, magic numbers

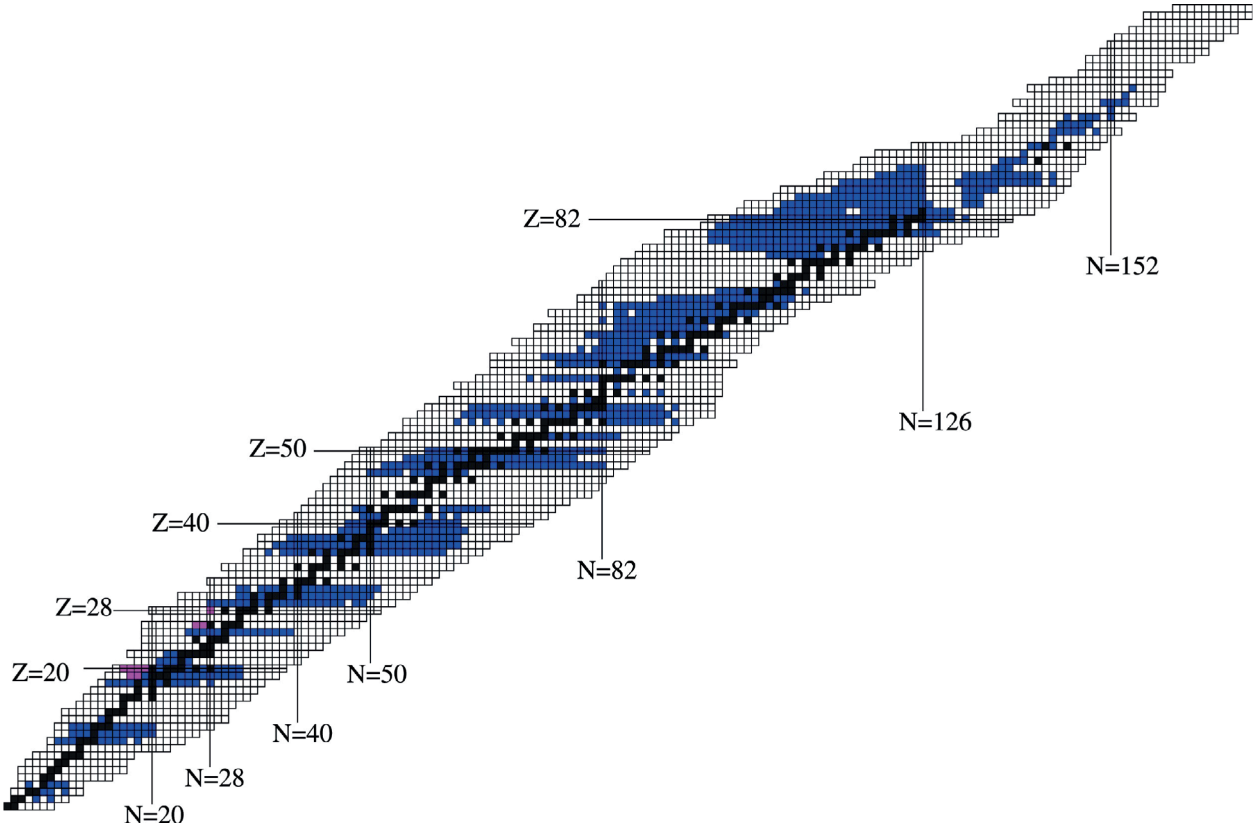

Figure 1.1: Figure modified from [16] highlighting nuclides which have been measured using optical spectroscopy. The nuclides are positioned with neutron number increasing toward the right, and proton number increasing vertically. Stable nuclei are highlighted in black, while blue squares indicate rare isotopes which have measurements from optical spectroscopy. Boxes in magenta indicate the rare isotopes which have been measured at BECOLA. The ability of spectroscopy to gain nuclear information from across all mass ranges and reach short lived isotopes far from stability is evident. For interpretation of the references to color in this and all other figures, the reader is referred to the electronic version of this thesis.

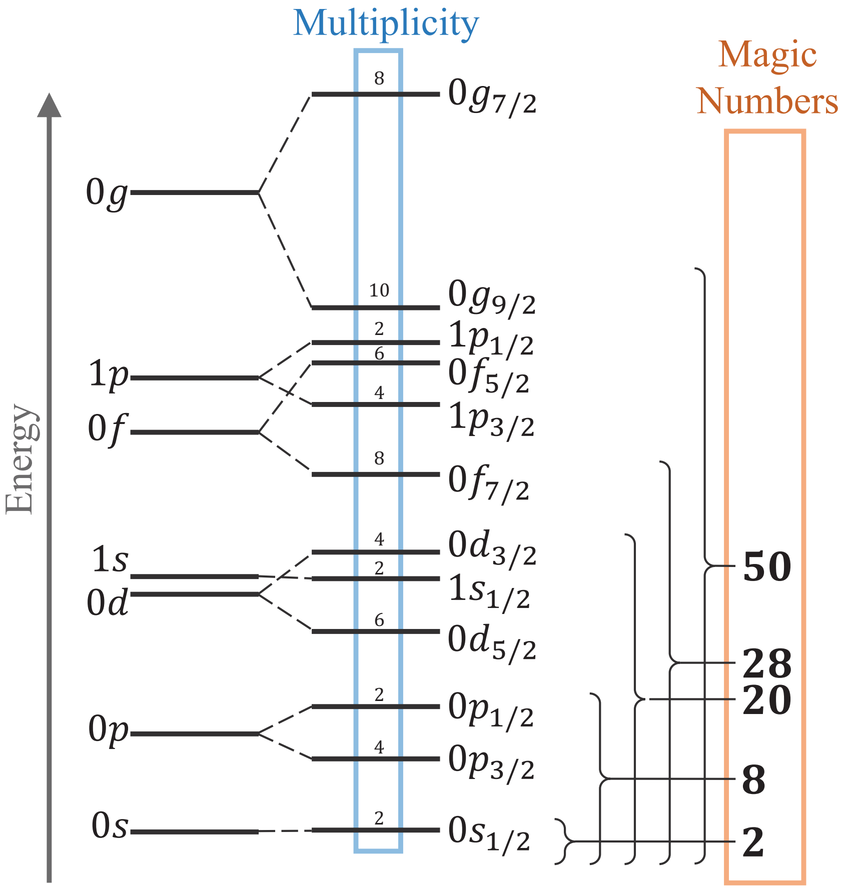
Multiplicity
Magic Numbers
Energy
$0g$
$1p$
$0f$
$1s$
$0d$
$0p$
$0s$
8
$0g_{7/2}$
10
$0g_{9/2}$
2
$1p_{1/2}$
6
$0f_{5/2}$
4
$1p_{3/2}$
8
$0f_{7/2}$
4
$0d_{3/2}$
2
$1s_{1/2}$
6
$0d_{5/2}$
2
$0p_{1/2}$
4
$0p_{3/2}$
2
$0s_{1/2}$
50
28
20
8
2

Figure 1.2: Single-particle levels of nucleons calculated from the nuclear shell model. On the left side are the energy states, and towards the right, the splitting from the spin-orbit interaction is included. The occupancy of these levels is noted above each. At shell closures where large gaps occur between one level and the next, magic numbers are observed. When moving away from stability, these levels shift, leading to the development of new magic numbers, and disappearance of others.

can be seen as a local minimum, where a sharp kink is present [4, 21]. This feature is caused by the nucleus taking on a spherical shape when a nucleon shell closure is reached, but becoming deformed and increasing the root mean-square (rms) charge radius when nucleons are added or removed from the system [22]. This signature is present in many chains of radii, but at neutron number $N = 20$ the expected kink structure nearly vanishes, as shown in Figure 1.3 [23].

Using CLS to examine a particular hf spectrum allows the transition energy to be precisely measured and compared to that of a reference isotope. This difference in energy is known as the Isotope Shift (IS) and from it, the differential charge radius can be extracted [12]. Measurements using CLS can therefore compare the charge radii of rare isotopes to those of known, stable isotopes, providing insights into the structure of nuclei far from stability.

1.2 Calcium

Due to the variety of stable isotopes in Ca (proton number $Z = 20$), spanning between two doubly-magic nuclei, ^{40,48}Ca ($N = 20, 28$), Ca has proven to be a unique element. Despite the addition of 8 neutrons, the mean-square charge radius of ^{48}Ca is nearly the same size as ^{40}Ca, while the isotopes in between rise and fall in a parabolic manner and possess a pronounced odd-even staggering, as shown in Figure 1.4. Nuclear theories have struggled to reproduce this the local maximum at ^{44}Ca [23], the odd-even staggering [24, 25], and the dramatic minimum at ^{48}Ca [21, 26, 27]. Because of this, the chain of Ca isotopes has become a proving ground for charge radii models.

Beyond the complex pattern seen in the charge radii, experimental evidence of doubly-magic features has been seen in neutron-rich Ca at $N = 32$ and $N = 34$ through precision

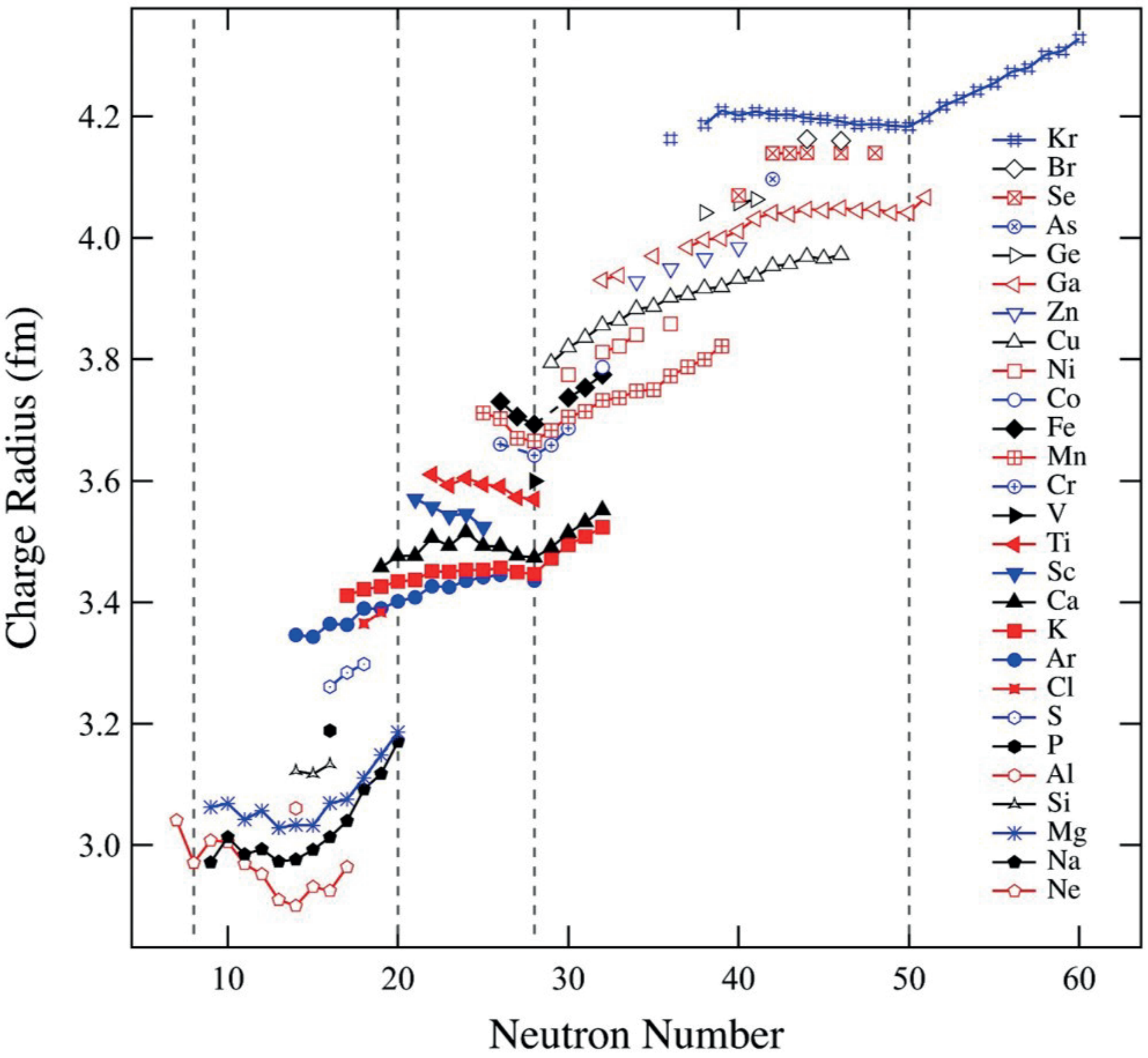

Figure 1.3: Examples of charge radii from Ne to Kr isotopes. Experimental data is from [4]. Neutron magic numbers are indicated by vertical dashed lines. A local minimum can be observed in many chains for $N = 28$ and $N = 50$, however this signature is not observed across $N = 20$.

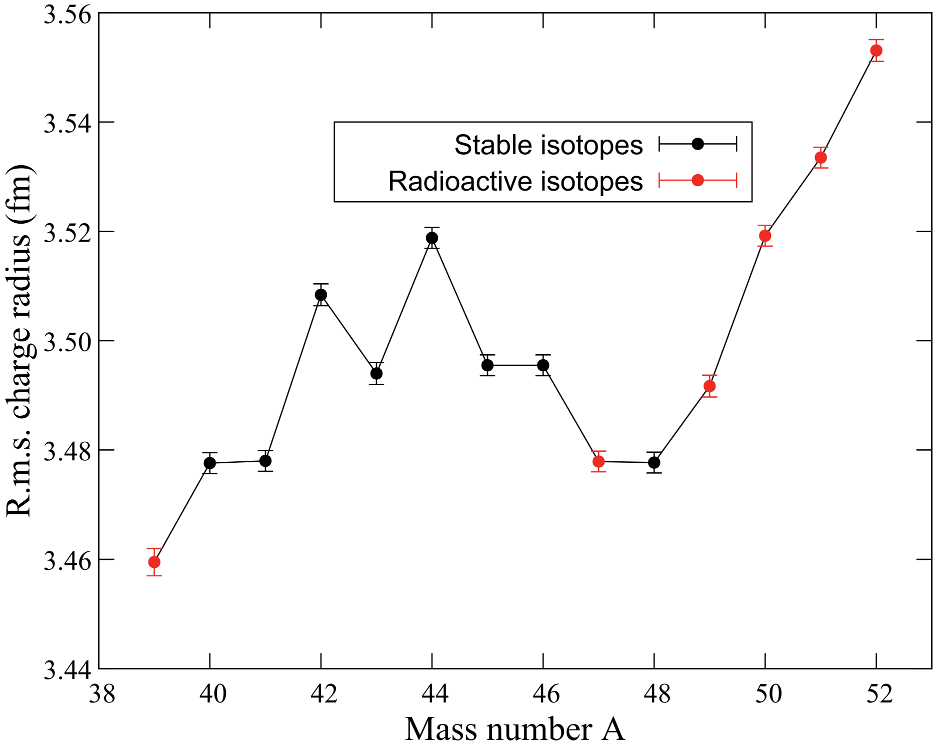

Figure 1.4: Experimental calcium charge radii prior to this work. Stable and long-lived isotopes are plotted in black, while unstable isotopes are plotted in red. Data taken from [4, 26]. The parabolic shape between $A = 40$ and $A = 48$, odd even staggering, and the dramatic rise beyond $A = 48$ have been difficult for theories to reproduce [23, 24, 25, 21, 26, 27].

mass measurements and 2^+ excitation energies respectively [28, 29], and evidence of doubly-magic nuclei is expected to be seen in the neutron-deficient region as well [18]. Recently, an investigation of neutron-rich Ca isotopes was carried out at CERN, and the charge radii of ^{49,51,52}Ca were determined for the first time [26]. The charge radii of these isotopes were surprisingly large compared with theoretical predictions, contrasting with the expectation of a spherical, doubly-magic nucleus at $N = 32$.

This interest in the chain of Ca isotopes has continued, and the unique production technique used at the NSCL has enabled the study of isotopes on the neutron-deficient side of the chain, reaching all the way to the short-lived ($T_{1/2} = 102\,\mathrm{ms}$ [30]) ^{36}Ca, and allowing measurements of the charge radii and nuclear moments.

1.3 Collinear Laser Spectroscopy at BECOLA

At the BEam COoling and LAser spectroscopy (BECOLA) facility at the National Superconducting Cyclotron Laboratory (NSCL), a CLS beamline was installed and commissioned in 2014 [31, 32]. Due to the in-flight production method (projectile-fragment reaction) mostly employed at the NSCL, BECOLA has a unique opportunity to study rare isotopes which are difficult to produce in sufficient quantities at other CLS facilities, where the Isotope Separation On Line (ISOL) technique is typically used. The projectile fragmentation reaction results in reaction products being emitted in a narrow forward angle at nearly the primary-beam velocity. Because of this, fragments can be selected efficiently and quickly using a magnetic spectrometer [33], and then thermalized in a gas cell [34].

At other CLS facilities, such as the COLLAPS collaboration at ISOLDE/CERN, the ISOL technique is used to produce rare isotopes. In this method, light ions bombard a thick target and stationary reaction products are produced within the target. These reaction products then need to be extracted, and long release times from the target can lead to large decay losses. This limitation has been partially overcome using the Ion Guide Isotope Separator On-Line (IGISOL) approach, which can allow a very fast extraction for some reaction products, however it is still difficult to achieve high rates for neutron-deficient isotopes [35].

As shown in Figure 1.1, laser spectroscopy has been utilized to study a number of isotopes to the left of the valley of stability in the heavier mass region, however for lighter isotopes, the short lifetimes, and thus difficulty of production and transport, make this region difficult to study. At BECOLA, several successful first-time measurements of these neutron deficient isotopes have been performed, including the charge radii of ^{36,37}K [23] and ^{52,53}Fe [21].

1.4 Dissertation overview

This dissertation will describe the recent charge radii measurement of neutron-deficient ^{36,37,38,39}Ca at BECOLA [36]. From the hf spectra, the differential mean-square (ms) charge radius of each isotope was extracted, as well as the ground-state nuclear moments of ^{37,39}Ca. While the charge radius of ^{39}Ca is known, all others are first-time measurements. The nuclear moments of ^{37}Ca were also determined for the first time [37], but will not be discussed in detail in this thesis. These results give valuable insight into nuclear structure and its evolution moving away from the valley of stability, hinting at the sub-shell closure in ^{36}Ca, and specifically elucidating the importance of the pairing interaction when weakly-bound states come into play.

Chapter 2 presents the experimental setup. It provides an introduction to CLS and describes the isotope production techniques used in this experiment. Several upgrades performed at BECOLA are also described, including the new photon detection system which was built and installed for use in this experiment. Chapter 3 contains the analysis procedure used to calibrate, fit, and extract the nuclear observables from the data. The calibration using two reference isotopes, which was used in this experiment for the first time at BECOLA, is described, and the hyperfine spectra of ^{36,37,38,39}Ca are presented. The extraction of the nuclear moments is mentioned briefly, and a more detailed description of the charge radii extraction is presented. Chapter 4 discusses the resulting ms charge radii in detail. The effect of weakly-bound proton levels is discussed, and the reproduction of these results using a state-of-the-art model of charge radii is presented. The experimental results are also compared to empirical predictions of charge radii. Chapter 5 summarizes the experimental and theoretical results, and gives an overview of future work. Appendix A provides a more detailed look at some experimental tools in the BECOLA beamline, including the photon detection system and the offline ion source. Appendix B gives information about software tools used for this experiment, providing details about the ROOT data structures and scripts used for the analysis. Appendix C outlines my personal contributions to the work at BECOLA, including mention of talks and presentations given

Chapter 2

Experiment

Schematics showing the experimental setup, including the rare isotope production system at the NSCL, the gas stopping system, and the CLS setup is shown in Figures 2.1, 2.2, and 2.3, respectively.

2.1 Basic principles

Collinear Laser Spectroscopy has been used with great success in past decades to examine the size and shape of nuclei [12, 13]. Early studies were limited in their usefulness by resolution and sensitivity, but recent technological advancements have dramatically increased the sensitivity, allowing high precision measurements of exotic isotopes [14, 16, 38, 39]. Laser spectroscopy has served as a valuable tool for exploring charge radii beyond stability, and has been used to study nuclei from light to heavy elements across the whole nuclear chart. The fundamental strategy is to precisely compare the shift of the hyperfine spectra between two isotopes. From this difference in energy, the difference in their mean-square charge radii can be extracted. For an isotope with a non-zero ground-state nuclear spin, the hyperfine splitting of the transition can also reveal the ground-state nuclear moments of that isotope. To achieve the required precision to extract these nuclear properties from radioactive beams with low rates, the signal-to-noise ratio (SNR) must be carefully optimized and measurements of stable reference isotopes must also be made with high precision.

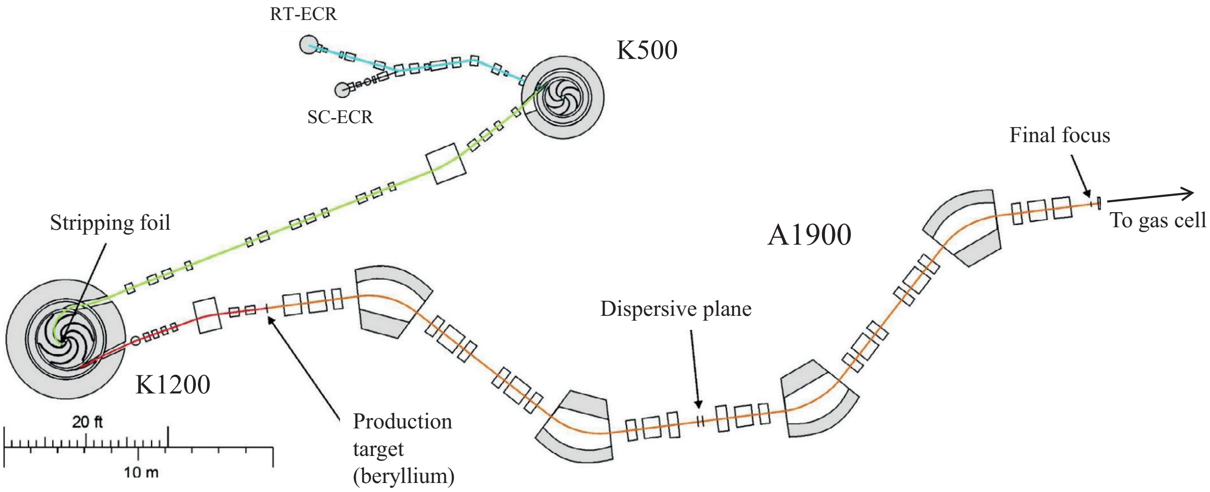
RT-ECR
K500
SC-ECR
Final focus
To gas cell
Stripping foil
A1900
Dispersive plane
K1200
20 ft
10 m
Production
target
(beryllium)

Figure 2.1: The rare isotope production at the NSCL. For this experiment, stable ^{40}Ca were generated and then accelerated to 140 MeV/nucleon using the coupled cyclotrons, K500 and K1200. Following this acceleration, the beam was impinged on a beryllium target. A wide range of isotopes was produced, and these isotopes were then passed through the A1900 fragment separator, in order to select those of interest. Following this schematic, the fast beams (0.5 c) were passed to the gas cell, where the beam is thermalized.

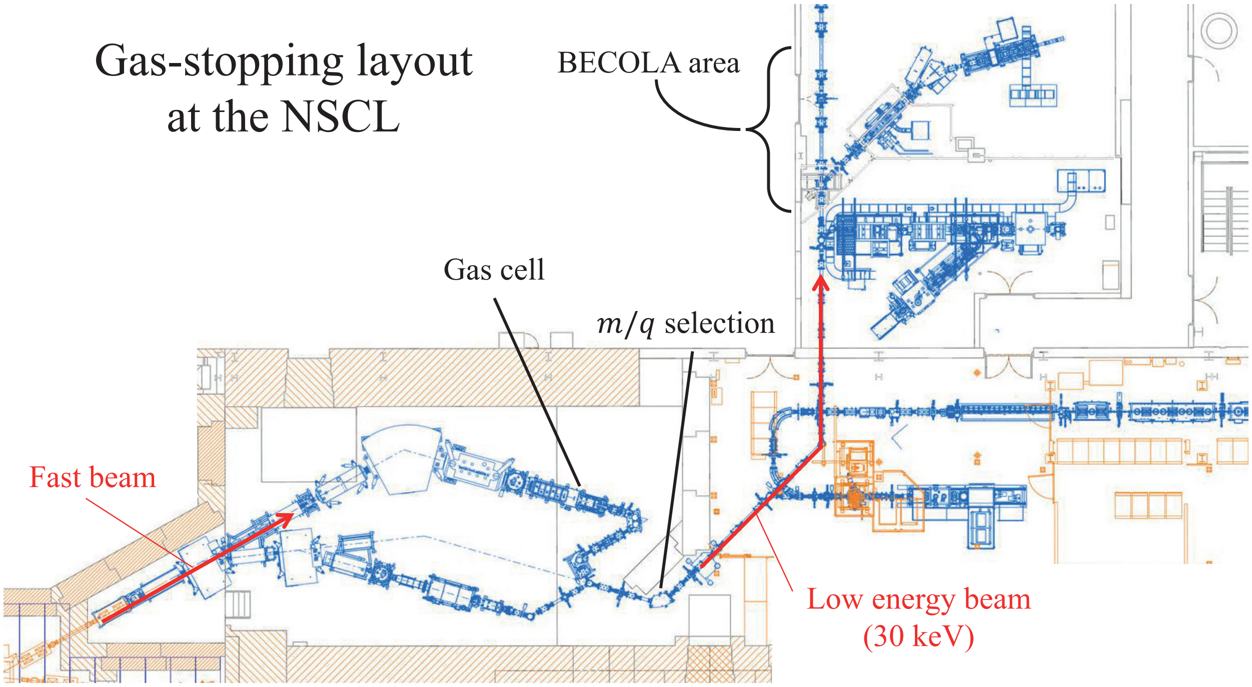
Gas-stopping layout
at the NSCL
BECOLA area
Gas cell
m/q selection
Fast beam
Low energy beam
(30 keV)

Figure 2.2: The gas stopping layout at the NSCL. Fast beams of rare isotopes are brought in from the left and are introduced to the gas cell, following a solid degrader. The ions are then thermalized in the helium buffer gas. On extraction from the gas cell, the desired charge/mass ratio can be selected using a dipole magnet. The low energy beam is then transported to the BECOLA facility, where collinear laser spectroscopy is performed.

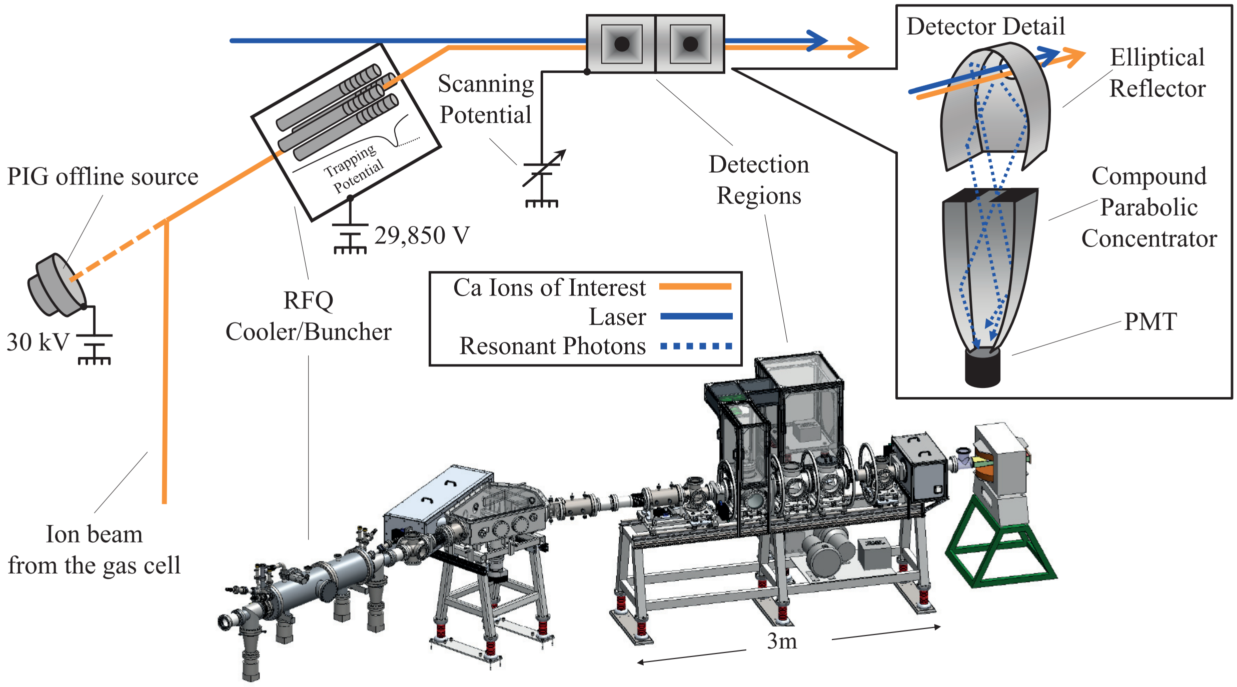
Detector Detail
Elliptical Reflector
Compound Parabolic Concentrator
PMT
Scanning Potential
Detection Regions
PIG offline source
Trapping Potential
29,850 V
30 kV
RFQ Cooler/Buncher
Ca Ions of Interest
Laser
Resonant Photons
Ion beam from the gas cell
3m

Figure 2.3: The collinear laser spectroscopy setup at BECOLA. Above is a cartoon showing the beam path of the laser and the ion beams. The radio-frequency quadrupole (RFQ) cooler/buncher is able to accept the beam from either the PIG offline source, or the radioactive "online" beam coming from the gas cell. As shown, the voltage at the detection region is scanned in order to scan the transition energy being probed, and the two photon detection systems collect the resonant photons. Below, a more true to life diagram is pictured, in order to give an accurate sense of scale.

2.1.1 Atomic transition

A favorable atomic transition is necessary for Collinear Laser Spectroscopy, specifically one that is accessible to the laser system and produces a strong signal. Detection of the spectral resonance requires absorption of the laser light to the excited state, and subsequent spontaneous emission in which the photons can be directed transverse to the beam. Because of this, the signal rate depends on the absorption and spontaneous emission rates of the transition. These rates are dependent on the population of the atomic states and the Einstein coefficients, A_{21} and B_{12} respectively. The larger the Einstein coefficients of the transition are, the more quickly the ions will absorb and emit photons through spontaneous emission. It is also important that the transition has a large branching-ratio from the upper state back to the lower state, so that the majority of decays arrive back at the ground state, rather than decaying to a state which is not being probed, as the transition may be excited several times as the ions travel through the detection regions.

In preparation for the experiment, spectroscopy of transitions in Ca I and Ca II were performed. Using the spectroscopic notation for charge states, Ca I refers to neutral calcium atoms, while Ca II, Ca III, etc. refer to the singly-, doubly-, and higher ionized states respectively. Both singly- and doubly-charged ions of stable ^{40}Ca were produced offline, as the ratio of Ca II and Ca III to be delivered from the gas cell was an unknown factor leading up to the online experiment. In the event of an online beam consisting primarily of Ca III, a charge-exchange process must be utilized, as all ground-state atomic transitions in Ca III are too high in energy to be accessed by the continuous wave laser systems at BECOLA. Several tests were performed to verify that charge-exchange and spectroscopy could be performed at BECOLA using Ca III (see Section A.2.2). Following the charge exchange process however, the Ca III ion beam is fractionalized into Ca I and Ca II, and various atomic states within each [40]. Due to this, the ideal situation would be to obtain a beam consisting entirely of Ca II, avoiding the fractionalization subsequent to charge exchange and the additional background photons produced as excited electronic states decay following the charge exchange process. Ultimately, the online beam coming from the gas cell was approximately evenly split between singly- and doubly-charged ions (see Section 2.2.1), and so spectroscopy was performed on the $4s\ ^2S_{1/2} \leftrightarrow 4p\ ^2P_{3/2}$ (393.3663 nm, $A_{21} = 1.47 \times 10^8\,\mathrm{s}^{-1}$ [41]) transition in singly-charged calcium ions. The atomic levels for Ca II are shown in Figure 2.4.

2.1.2 Laser system

To excite this transition in Ca II, a Sirah Matisse TS Ti:Sapphire ring laser was used. This laser frequency was locked to 787 nm light using a HighFinesse WSU-30 wavelength meter, which was calibrated by a frequency-stabilized He-Ne laser. The 787 nm light was then frequency-doubled using a SpectraPhysics WaveTrain, in order to reach the near UV light (393 nm) required. After being transported through a fiber-optic cable, 300 µW of this light was then collimated down the beam line. The laser power was stabilized just prior to entering the beamline using a laser-power controller (LPC) [43]. The controlling optic of the LPC was placed immediately following the Ti:Sapphire laser, prior to the frequency doubler. The transmittance of this device was controlled using voltage input from a power meter monitoring a 10 % sample of the blue laser beam after exiting the fiber-optic cable and passing through a polarizing cube to redefine the vertical polarization of the light. This was the first time that this setup was used in an online experiment at BECOLA, and ensures that any long term drifts in transmittance of the fiber or rotation of the polarization exiting the fiber can be counteracted by the LPC, allowing a stable 300 µW beam to enter the BECOLA

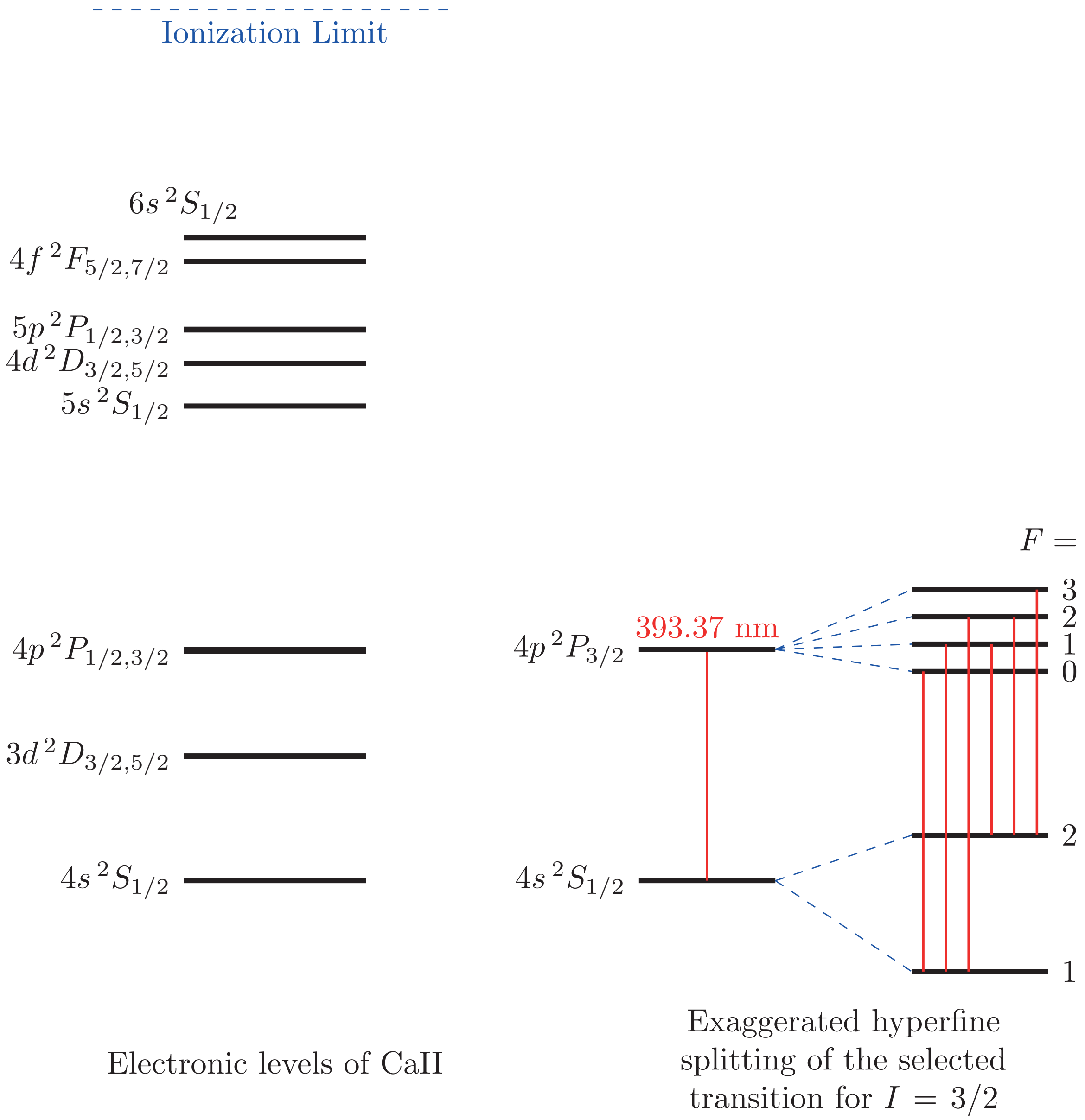
Ionization Limit
$6s\,^2S_{1/2}$
$4f\,^2F_{5/2,7/2}$
$5p\,^2P_{1/2,3/2}$
$4d\,^2D_{3/2,5/2}$
$5s\,^2S_{1/2}$
$4p\,^2P_{1/2,3/2}$
$3d\,^2D_{3/2,5/2}$
$4s\,^2S_{1/2}$
Electronic levels of CaII
$F =$
393.37 nm
$4p\,^2P_{3/2}$
3
2
1
0
$4s\,^2S_{1/2}$
2
1
Exaggerated hyperfine splitting of the selected transition for $I = 3/2$

Figure 2.4: Atomic states, and hyperfine splitting. On the left, the electronic levels for Ca II are drawn [41]. On the right, the selected transition is drawn, along with the hf splitting for $I = 3/2$, as in ^{37,39}Ca [42]. The allowed hf transitions are marked in red.

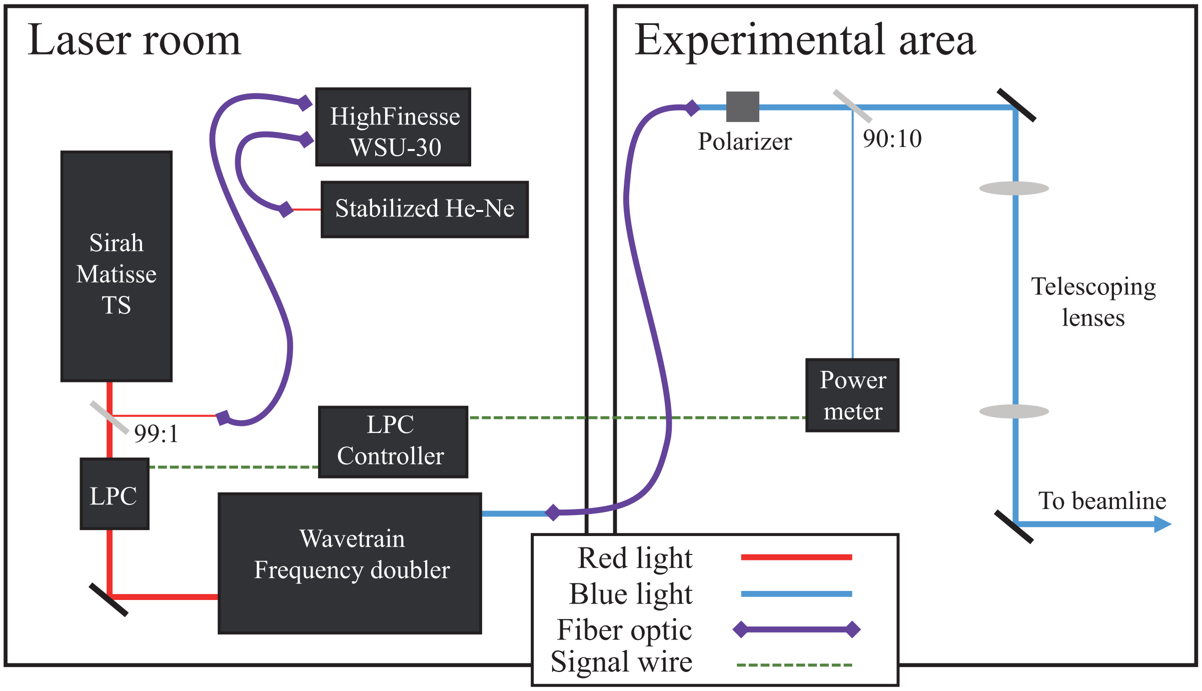
Laser room
Experimental area
HighFinesse WSU-30
Stabilized He-Ne
Sirah Matisse TS
99:1
LPC Controller
LPC
Wavetrain Frequency doubler
Polarizer
90:10
Telescoping lenses
Power meter
To beamline
Red light
Blue light
Fiber optic
Signal wire

Figure 2.5: The laser setup used in this experiment. The Sirah Matisse TS Ti:Sapphire laser was frequency locked using the stabilized He-Ne and the wavelength meter, by sampling 1 % of the light as shown. The majority of this light was frequency doubled, and transported to the experimental area using a fiber optic cable. Here, after passing through a polarizing cube, 10 % of the light was sampled by a power meter in order to control the LPC, which modulated the power entering the frequency doubler. This allowed power fluctuations introduced by the transmission through the fiber to be eliminated, and ensure a stable 300 µW beam for CLS.

beamline for the spectroscopy. A schematic of this setup can be seen in Figure 2.5.

2.1.3 Hyperfine interaction

^{36,38,40,44}Ca are even-even nuclei, possessing a ground-state nuclear spin of 0. For ^{37,39}Ca however, the ground-state nuclear spin is 3/2, due to an unpaired neutron in the $0d_{3/2}$ shell. With a non-zero nuclear spin, the alignment between the spin of the nucleus, $\mathbf{I}$, and the atomic spin $\mathbf{J}$ creates a hyperfine splitting of the levels in the atomic transition, leading to six allowed transition energies for the ^{37,39}Ca spectra.

The shift of an electronic level relative to the fine energy is given by the equation:

$$\Delta E = \frac{K}{2}A^{\mathrm{hf}} + \frac{3K(K+1) - 4I(I+1)J(J+1)}{8I(2I-1)J(2J-1)}B^{\mathrm{hf}} \tag{2.1}$$

where $K = F(F+1) - I(I+1) - J(J+1)$, F is the quantum number defined by the vector $\mathbf{F} = \mathbf{I} + \mathbf{J}$, and A^{hf} and B^{hf} are the hyperfine coupling constants of the atomic level.

The Ca II transition used in this work connects the upper state $^2P_{3/2}$ $(J = 3/2)$ and the lower state $^2S_{1/2}$ $(J = 1/2)$, using the notation $^{2S+1}L_J$. From the nuclear spin, $I = 3/2$ present in ^{37,39}Ca [42], possible values of F in the upper state are integer steps between $(3/2 + 3/2)$ and $(3/2 - 3/2)$, leading to the values

$$F_{\mathrm{upper}} = 3, 2, 1, 0. \tag{2.2}$$

Possible values of F in the lower state are then integer steps between $(3/2 + 1/2)$ and $(3/2 - 1/2)$, giving

$$F_{\mathrm{lower}} = 2, 1. \tag{2.3}$$

Thus, the upper level is split into four energy levels, while the lower is split into two. Due to the selection rules of the transition, $\Delta F = +1, 0, -1$, six transitions are allowed:

$$(F_{\mathrm{upper}}, F_{\mathrm{lower}}) = (3,2), (2,2), (1,2), (2,1), (1,1), (0,1). \tag{2.4}$$

To obtain the difference in energy from the centroid, Equation 2.1 can be used to find

ΔE_{upper} and ΔE_{lower}, giving a transition energy of

$$E = E_0 + \Delta E_{\text{upper}} - \Delta E_{\text{lower}} \tag{2.5}$$

where E_0 is the centroid energy of the transition. A schematic diagram of this hf splitting, highlighting the allowed transitions is shown in Figure 2.4.

The hyperfine coupling constants A^{hf} and B^{hf} are defined as,

$$A^{\text{hf}} = \mu B_0/(IJ), \tag{2.6}$$

$$B^{\text{hf}} = eQV_{zz}. \tag{2.7}$$

Here μ and Q are the magnetic-dipole and spectroscopic electric-quadrupole moment of the nucleus, e is the elementary charge, and B_0 and V_{zz} are the magnetic field and electric-field gradient respectively, which are produced at the nucleus by the orbital electrons. In the case of the lower level ($^2S_{1/2}$) the electric field is spherically symmetric, leading to a gradient of 0 at the nucleus, and thus a B^{hf} of 0. This means there are three hyperfine coupling constants for each isotope.

When a hf spectrum is measured, the positions of the peaks can be fitted using the energies described from Equation 2.5 by allowing these hyperfine coupling constants to vary. From this fit, the hyperfine coupling constants can be determined, and thus the nuclear moments can be extracted using some knowledge of B_0 and V_{zz}, which will be the same for each isotope assuming a point-like nucleus [37] (see Sections 3.2.2.1 and 3.3).

2.1.4 Bunched beam background suppression

In recent years, background suppression by using a bunched ion beam has led to major advancements in CLS [38, 39]. Stray photons reaching the PMT from the laser are a significant source of background. These cannot easily be filtered out due to the fact that the fluorescence photons are the same wavelength as the laser light. By bunching the ion beam and counting photons only in the window of time where the ion bunch comes past the detector, a large portion of the constant background caused by stray light from the laser can be ignored. If, for example, the ion beam bunch is released once per second, and the bunch has a time spread of 1 µs, this will reduce the measured laser background by a factor of 10^6, without reducing the amount of signal observed (assuming perfect bunching efficiency).

This technique is employed at BECOLA using a two-section cooler/buncher [44, 45]. The first section is operated with a helium-buffer-gas pressure of approximately 0.1 mbar [45], to efficiently cool the incoming ions. Ions are contained laterally in the trap using a radio-frequency quadrupole (RFQ), which is sensitive to the charge/mass ratio of the ions. As the ions move through a longitudinal drag field, they move into the bunching section, where the pressure is approximately 100 times lower [45], and a weaker lateral containment field is present. This lower pressure section allows for better emittance in the ion bunch, and allows a low energy spread, resulting in a time width of 1 µs for each bunch (FWHM). A schematic of the cooler/buncher is shown in Figure 2.7, and the differential pumping design can be seen in Figure 2.8.

The bunches typically have a time-spread of 1 µs FWHM, however depending on how full the trap is, the time spectrum at the detection region can be affected. In Figure 2.6, the two most extreme time spectra from this experiment can be seen; ^{36}Ca and ^{44}Ca, which were

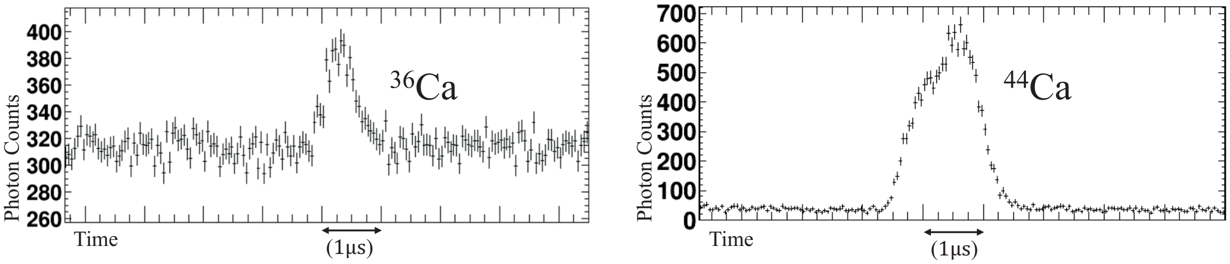

Figure 2.6: The recorded time spectra for the ^{36}Ca and ^{44}Ca bunched beams. ^{36}Ca had the fewest ions contained in each bunch, thus giving the narrowest time-width, while ^{44}Ca had the most ions per bunch, due to contamination from the more abundant ^{40}Ca (see Section 2.3.1.2), leading to a slightly wider peak in time. The ^{36}Ca time-spectrum is taken from the full 33 h running time with that isotope, while the ^{44}Ca time-spectrum is taken from a single reference measurement of < 1 h. Other isotopes measured in this experiment fall within these two extremes, with a time-width of approximately 1 μs.

operated with the fewest and greatest number of ions in the trap, respectively.

This bunched beam technique is crucial to reduce the laser related background, which is the same wavelength as the signal, and is the predominant source of background for the Ca isotope measurements. Several factors can limit the effectiveness of the bunched beam technique however. To avoid losing signal, loss of ions due to the holding time must be taken into account. At low incoming rates of ions, the BECOLA cooler/buncher is consistently able to hold ion bunches for up to 1 s before seeing a decrease in the trapping efficiency, as shown in Figure 2.9. When dealing with unstable ions however, the half-life of the isotope can become a limiting factor, and the reduction in background must be balanced against the loss of signal caused by the increase of decays taking place in the trap. When filling the trap for an extended time, the rate of incoming ions will become offset by the decay of ions currently in the trap, and the signal per bunch will plateau. Regardless of the time between bunches, the time spread of each bunch will alway span across 1 μs, resulting in a consistent amount of laser related background recorded per bunch. Because of this, bunching times significantly longer than the half-life of the isotope in question will lead to a consistent SNR per bunch, however, because there is no gain in the signal strength from the increased time, the longer time between bunches serves only to reduce the frequency at which signal and noise are being gathered.

To determine the optimal bunching time for the short-lived Ca isotopes, this reduction in sensitivity was taken into account. Examining SNR as a function of the bunching period, T_b, a peak can be found at $\sim 1.8 \times T_{1/2}$. Because a consistent amount of background is recorded during the time window of each bunch, the background rate (per time, not per bunch) varies as

$$B(T_b) \propto 1/T_b. \tag{2.8}$$

The signal recorded per time depends on the amount of ions present at the time the bunch is released, and the rate at which bunches are released. Because of the decays within the trap, the ions held in the trap at the time of release is proportional to $(1/\lambda)(1 - e^{-\lambda T_b})$, where λ is the decay constant of the isotope. The signal rate is then

$$S(T_b) \propto (1/\lambda)(1 - e^{-\lambda T_b})/T_b \tag{2.9}$$

when taking into account how frequently these bunches of signal arrive. The SNR can then be written

$$\mathrm{SNR} = \frac{S(T_b)}{\sqrt{B(T_b)}} \propto \frac{(1/\lambda)(1 - e^{-\lambda T_b})}{\sqrt{T_b}} \tag{2.10}$$

Expressing this in terms of the half-life, $T_{1/2} = \ln(2)/\lambda$, we arrive at a more useful expression,

$$\mathrm{SNR} \propto \sqrt{T_{1/2}} \frac{(1 - e^{-T_b/T_{1/2}})}{\sqrt{T_b/T_{1/2}}} \tag{2.11}$$

In this form, the SNR can plotted versus $T_b/T_{1/2}$ as shown in Figure 2.10. From this it was

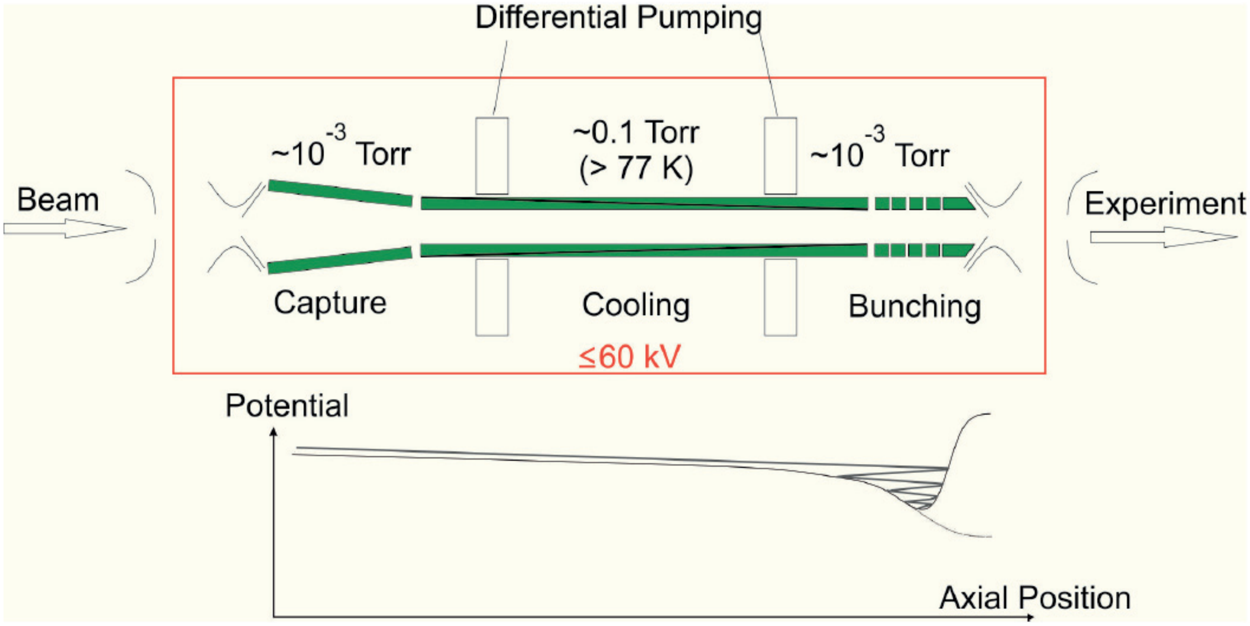

Figure 2.7: Above is a schematic of the cooler/buncher used at BECOLA. A unique aspect of this design is the separate cooling and bunching sections, which are operated with different buffer gas pressures. The differential pumping scheme used to maintain the central high-pressure region can be seen in Figure 2.8. The ions are contained laterally by the pseudo-potential of a radio-frequency quadrupole (RFQ), while a drag potential is maintained in the longitudinal direction using segmented electrodes. The graph below the schematic shows the drag and trapping potential along the beam axis, the dashed line on the right indicates the potential used to release the ion bunch. Figure from ref. [44].

determined that the maximum SNR is obtained using a bunching time $T_b \approx 1.8 \times T_{1/2}$. This was used to set the bunching period used during the experiment for ^{36,37}Ca. Due to the longer half-lives and higher rates, the bunching periods selected for ^{38,39}Ca were shorter than these ideal calculations, because of the space-charge limitations of the trap. These bunching periods and rates are shown in Table 2.2.

2.1.5 Doppler-shift

The precision which can be achieved through collinear laser spectroscopy is due to use of the Doppler-shift. While the laser is stabilized and held at a specific frequency, the velocity of the ion beam can be modified by scanning the small voltage applied at the detection

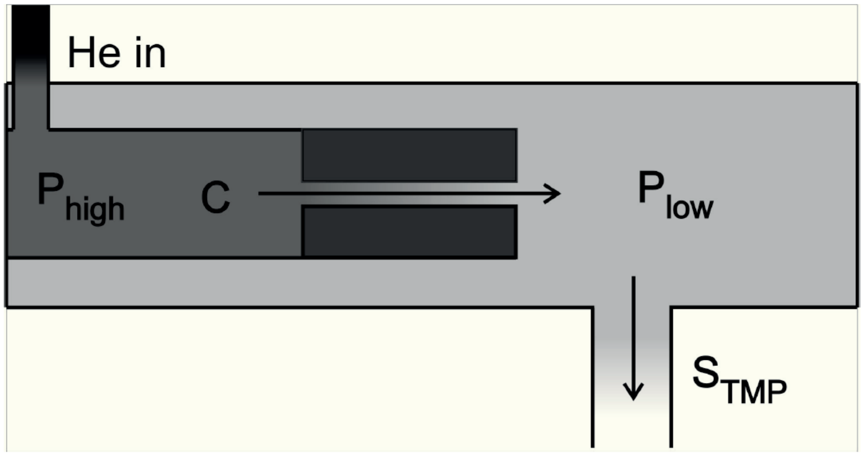

Figure 2.8: Illustration of the differential pumping channel. The high and low pressure regions are connected via a narrow channel with relatively low conductance (marked "C"). The helium is introduced into the high pressure region, and pumped from the low pressure region using a turbomolecular pump (marked "S_{TMP}"). Figure from ref. [44].

region. Scanning across the transition is accomplished by utilizing the fact that the ions are moving along to the light path, allowing a precise variation in the effective laser frequency. In addition, by performing an in-flight measurement at 30 keV, the velocity of the ion beam reduces Doppler-broadening due to thermal motion of ions within the bunch, as shown in Figure 2.11, resulting in a narrow line width [46, 47]. Because the area of the peak is not changed, the peak height is increased by the same factor as the linewidth is reduced, thus this kinematical compression increases both sensitivity and resolution [12].

When accelerated across the potential difference U, kinetic energy (KE) of qU is given to each ion. Using the relativistic expression for KE,

$$\mathrm{KE} = qU = \frac{1}{\sqrt{1-\beta^2}}mc^2 - mc^2 \tag{2.12}$$

where m is the rest mass of the ion, and β is the velocity in units of c. This expression can

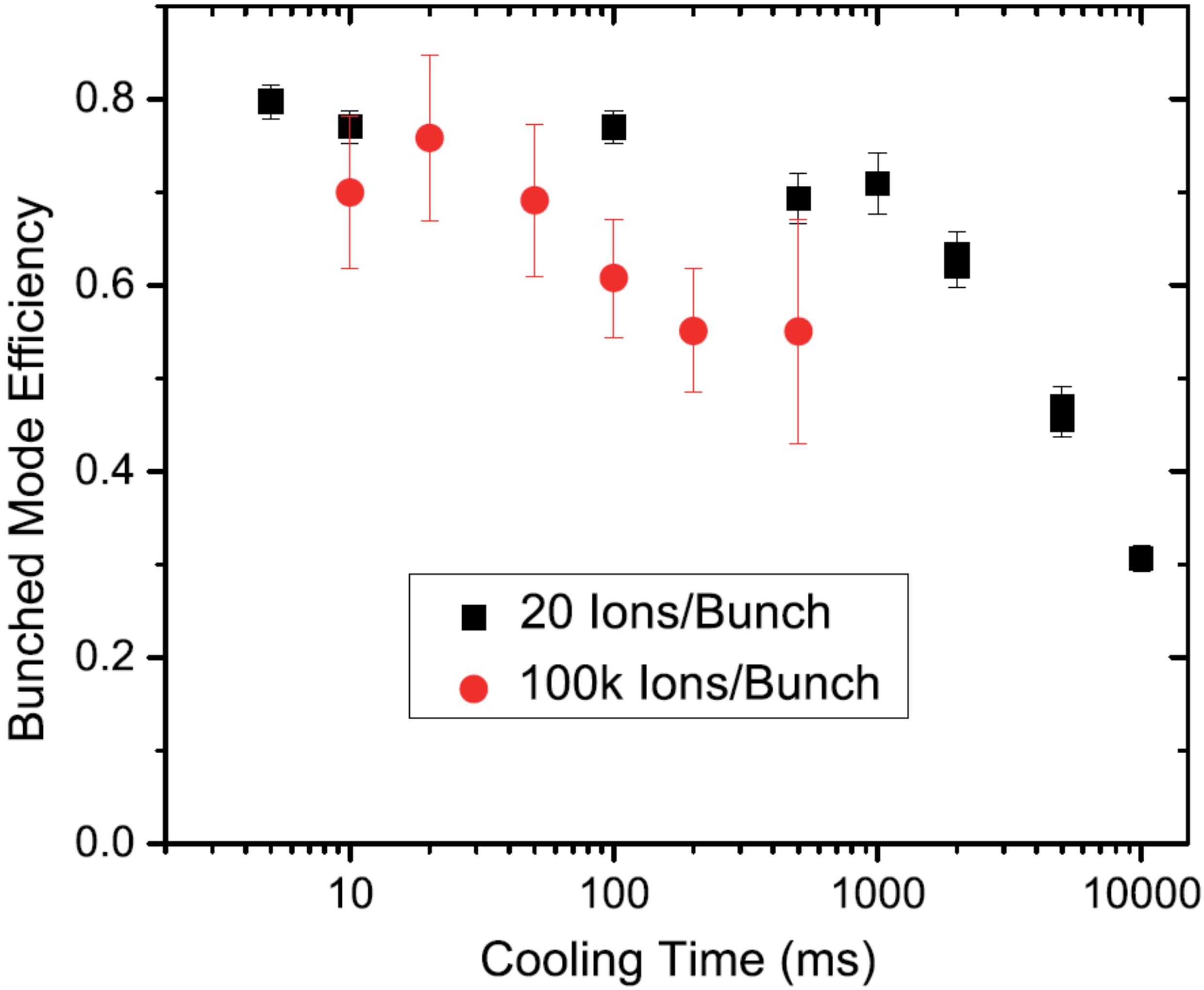

Figure 2.9: The bunching efficiency as a function of cooling time. As shown by the black squares, with small quantities of ions there is minimal reduction in efficiency for holding times up to one second. These measurements were made using potassium ions. Figure from ref. [45].

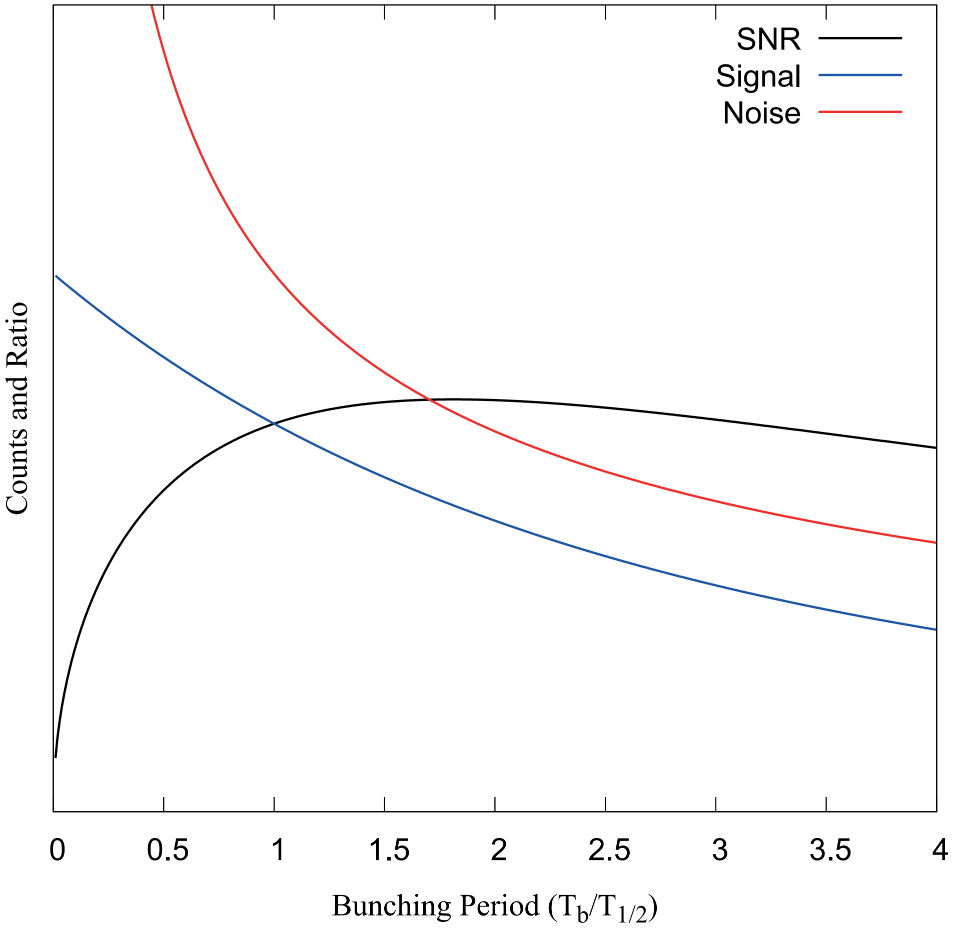

Figure 2.10: A plot showing the effect that the bunching period, T_b, has on the signal and noise collected when using unstable isotopes, assuming that the efficiency of the cooler is unaffected by the bunching period, and that the measurement time for each bunch is 1 µs regardless of the holding period. The vertical axis represents the noise and signal counts collected after a given time (see Equations 2.8 and 2.9), and their ratio (Equation 2.11). No units are provided on the vertical axis, as the absolute quantities also depend on other factors, such as the half-life, incoming beam rates, and the measurement time of the bunch. The signal counts are shown in blue, noise counts in red, and SNR (scaled arbitrarily) is shown in black. As the period is increased, the ions held in the trap, and thus the signal per bunch, will eventually plateau, however, the increased time between bunches leads to a continued reduction in signal collected. The noise collected from the laser is also reduced due to the decrease in total background caused by measuring the data in fewer bunches. Although both signal and noise are monotonically decreasing, the drastic reduction in noise causes the SNR to be maximized when $T_b \approx 1.8 \times T_{1/2}$.

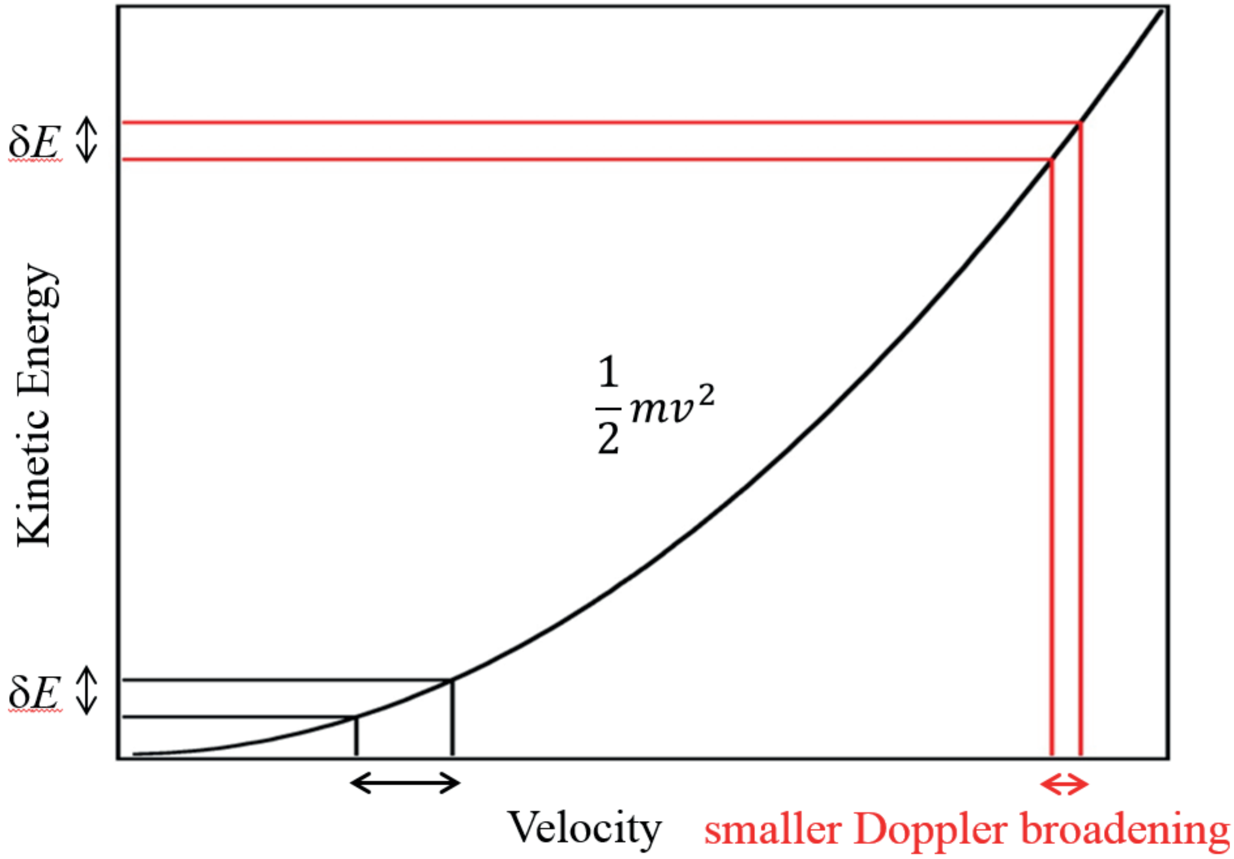

Figure 2.11: This plot highlights the benefits of an in-flight measurement with regard to Doppler-broadening. For a given temperature of ions, there will be a small spread in kinetic energy, leading to a spread in velocity (black bands). When the ions are accelerated over a large potential, although the energy spread remains the same (and is small compared to the energy following acceleration), the corresponding velocity spread is reduced (red bands). Because the velocity determines the effective frequency of the laser light that the ions are interacting with, this velocity bunching results in narrower resonance peaks.

be solved for β to give,

$$\beta = \sqrt{1 - \frac{1}{1 + q^2(U/m)^2 + 2qU/m}} \tag{2.13}$$

where β is the velocity in units of c, q is the charge of the ions in units of e, U is the potential difference in Volts, and m is the mass of the ions in units of eV/c^2. From this velocity, the Doppler-shifted frequency is expressed,

$$f_{\text{obs}} = f\sqrt{\frac{1-\beta}{1+\beta}} \tag{2.14}$$

where f_{obs} is the Doppler shifted frequency observed by the collinear particles as they move away from the source, and f is the stable frequency of the laser. In this way, each voltage step at the interaction region can be precisely converted to a frequency.

For this experiment, the singly-ionized Ca ions were released from the cooler/buncher with an energy of approximately 29 850 V [36]. This results in a shift of the observed laser frequency equivalent to approximately 16 MHz for each volt applied to the detection region. The set laser frequency, as well as the ranges of the scanning voltage applied to the detection region for each isotope are shown in Table 2.1.

2.2 Isotope production

2.2.1 Rare isotopes

One unique aspect of the BECOLA facility is the access to neutron-deficient isotopes that the NSCL can provide. By using fast in-flight production and separation, rare isotopes with

Table 2.1: The set laser frequency and scanning voltage used for each measurement. The set laser frequency is the wavenumber of the Ti:Sapphire laser prior to the frequency doubler, while the scanning region indicates the range of the scanning potential applied to the detection region as the spectra were recorded.

A	Set Laser Freq (1/cm)	Scanning Region(s) (V)
36	12724.14966	5–45
37	12723.92541	−80–30 , 45–105
38	12723.7097	−15–65
39	12723.51262	−105–−45 ,70–120
40	12723.30257	−15–65
44	12722.5675	−15–65

short half-lives can be produced in sufficient quantities to perform CLS. A fast primary beam of ^{40}Ca (140 MeV/nucleon) is obtained using the coupled superconducting cyclotrons, and impinged on a Be target, with a thickness of 658 mg/cm^2. From the projectile-fragmentation reactions, reaction products are produced in flight, and specific isotopes can be selected using the A1900 fragment separator [33]. This technique is complementary to the ISOL technique employed at other CLS facilities [35], in that it allows beams of rare isotopes to be produced without regards to their chemical properties.

The fast beam is then injected into a helium-filled gas cell stopper [34] where the ions are thermalized. After the stopping range selection in the cell Ca-ions are extracted at an energy of 30 keV and transported to the BECOLA facility. On extraction from the gas cell, a potential of 400 V was used for collision-induced dissociation to dissociate water molecules attached to the calcium ions. This voltage was selected to give a large portion of singly-charged ions with no attached molecules, without greatly reducing the overall efficiency and degrading the emittance of the beam. The distribution of these different states when this dissociation voltage was used are shown in Figure 2.12.

At BECOLA, the rare isotopes are injected into the cooler/buncher, and extracted in

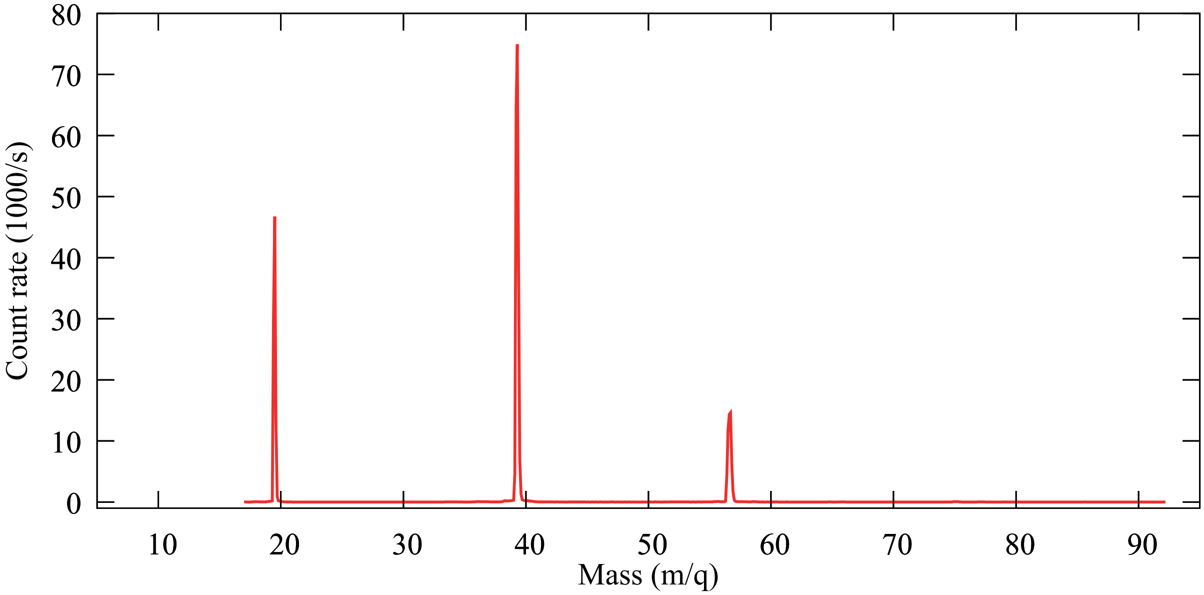

Figure 2.12: Experimental data from the gas cell group showing the mass-to-charge spectrum of ^{39}Ca extraction from the gas cell. The horizontal axis shows the selected mass/charge ratio (amu/e), while the vertical axis indicates the decay rate seen in the extracted beam. The peak at 39 is attributed to singly-charged ^{39}Ca ions, while the peak at 19.5 contains the doubly-charged ions of this species. At $m/q = 57$, a peak can also be seen due to singly-charged ^{39}Ca with a single water molecule (18 amu) attached. This spectrum was taken using 400 V for the dissociation potential. As shown, this results in a significant portion of singly-ionized ^{39}Ca which was then transported to BECOLA to perform spectroscopy.

bunches periodically. As discussed in Section 2.1.4, the repetition rate of the bunches was selected for each isotope to optimize the signal-to-noise ratio of the system. For ^{36,37}Ca, the bunching rates were determined based on the half-life, however in the case of ^{38,39}Ca and the reference isotopes ^{40,44}Ca, the repetition rate was limited by the number of ions able to be contained in the trap without disturbing the beam emittance. The approximate ion beam intensity at BECOLA and the repetition rates used for the spectroscopy are presented in Table 2.2.

Table 2.2: The half-life ($T_{1/2}$), bunching period (T_b), rates at the cooler/buncher for the rare isotopes, and the total measurement time used for each isotope. The bunching repetition rates for ^{36,37}Ca were chosen based on the short half-lives, while the bunching periods of ^{38,39}Ca were affected by the high ion rates and the space-charge limitations of the trap. Because the reference isotopes ^{40,44}Ca can be produced with high ion currents, they have different limitations, which are discussed in Section 2.3.1.2.

A	$T_{1/2}$ (ms)	T_b (ms)	Rate (1/s)	Msmt Time (h)
36	102	180	50	33.3
37	181	330	960	42.3
38	440	220	13500	9.8
39	859.6	30	60000	8.5
40	—	30	See 2.3.1.2	< 1
44	—	30	See 2.3.1.2	< 1

2.3 System upgrades

In order to achieve the sensitivity required to measure all four isotopes during this online run, several upgrades and optimizations were carried out at the BECOLA beamline. The most dramatic change for this experiment was the installation of a newly-designed photon detection system (PDS), but other experimental strategies were also employed for the first time in this online experiment, such as the use of two reference isotopes for calibration.

2.3.1 Reference isotopes

To obtain a precise measurement of the isotope shift, the spectrum of two reference isotopes were taken. By measuring an isotope with a known transition frequency periodically throughout the experiment, not only does it serve as a reference for the isotope shift, but it also allows an understanding of the small fluctuations that may take place during the hours or days taken to measure the unknown isotope. The known isotope shift between the two reference isotopes can also be used to understand the release voltage of the cooler/buncher (see Section 3.1). These measurements require an offline ion source with a sufficient rate and a stable beam current. Using an ion-source with a high rate allows for these calibration measurements to be taken quickly, in order to minimize the interruption of the rare isotope beam. Because of the relatively short time frame for each of these measurements ($< 1\,\mathrm{h}$), the stability of the source is crucial, to prevent fluctuations in the baseline of the spectrum during the measurement. If a source requires a long period of time to stabilize, this again takes time away from the measurement of the unknown isotope.

At BECOLA, a Penning Ionization Gauge (PIG) source was used to serve this purpose with great success. This source requires relatively little warm up, and provides a consistent ion current. It can also be used to produce a wide range of elements by using an electrode or buffer gas which contains the desired element(s). Ions from the source are produced from both the cathode material and the buffer gas. By utilizing a buffer gas which has a significantly different mass than the isotope of interest, the RFQ in the cooler/buncher can be used as a mass filter to select only the isotope of interest. Although this source was designed and installed in 2015, several upgrades were performed prior to this experiment in order to improve the stability and warm-up time.

2.3.1.1 PIG source upgrades

The design of the PIG source used at BECOLA provides a convenient way to produce large currents of a variety of stable ions (typically on the order of 10 nA of beam current following the cooler/buncher). The flow of the buffer gas into the PIG source is the most difficult aspect of the source to stabilize and control. When operating the PIG source, fluctuations in the gas pressure have been observed to directly affect the ion current exiting the source, including the current after the cooler/buncher. In previous experiments, this pressure was controlled by adjusting a hand valve, which required lowering the high voltage in order to physically adjust the knob, as well as a period of time to stabilize after making adjustments.

To improve the performance and reduce the time required to start the source, a mass-flow controller (MFC) was obtained from Bronkhorst, Inc. with a flow range of 0.014–0.7 $\mathrm{ml_n}$/min. While this upgrade greatly simplified the start-up procedure for the source, it also has the benefit of enabling easy control of the gas pressure, allowing a more thorough and repeatable exploration of the source parameters. The MFC allows very stable pressures to be achieved quickly, and can be controlled remotely without lowering the high voltage. Because of this ease of control, the PIG source was able to be operated successfully using a He buffer gas, which was not possible when using the hand valve due to the narrow range of gas pressures which enable the plasma generation. For more details regarding the setup and operation of the MFC, see Appendix A.

In order to use this source to produce the two reference Ca isotopes, cathodes were ordered from ACI Alloys, Inc. consisting of a custom alloy with an atomic ratio of 2 parts Sn to 1 part Ca, with greater than 99 % purity. The mass difference between Sn and Ca is sufficient to filter out the Sn in the cooler/buncher. Due to being mixed with Sn, the cathodes are expected to be less reactive than pure Ca, however, care was taken during shipping and installation to minimize contact with air to avoid oxidization of the surface. The primary exposure to air occurred during the installation of the cathodes into the PIG source, a process taking approximately 30 min, and no effects from oxidization were observed in the operation of the PIG source.

2.3.1.2 Isotopic limitations

The PIG source produces much larger quantities of ions than are needed, however the primary limitation is due to the fact that the naturally-occurring isotopes are produced in ratio with their abundance within the cathode material. Because they are so close in mass, the cooler/buncher is unable to filter between the reference isotopes, and the space-charge limitations of the trap then dictate a maximum amount of signal per bunch for a given isotope.

The primary reference, ^{40}Ca, has a natural abundance of 96.94 % and serves as the reference for the isotope shift of the rare isotopes, in order to extract the charge radii. A second isotope, ^{44}Ca, was also measured throughout the experiment, in order to calibrate the spectra as described in Section 3.1. ^{44}Ca is the second most abundant isotope at only 2.09 %, making it more difficult to measure efficiently.

When measuring the transition in ^{44}Ca, the ion trap was slightly overfilled in order to achieve an acceptable reference measurement in under 1 h. This results in a slightly wider time spread of the ion bunch at the detection region (2 µs FWHM), however several measurements of ^{44}Ca were taken using the narrower time width as well in order to verify that this small change did not affect the peak position in the energy spectrum. The time spectra of ^{36}Ca and ^{44}Ca are shown in Figure 2.6.

2.3.2 Photon detection system

While the bunched beam technique allows for dramatic improvements to the laser background, the sensitivity of the system is still dependent on the ability of the photon detection system (PDS) to collect resonant photons from the laser-excited ion beam, and exclude stray light from the laser. Signal collection is performed using a photo-multiplier tube (PMT) which is aligned radially to the beam axis. The goal is to allow photons from the laser to simply pass by the detector, while those which are absorbed and spontaneously emitted from the ion bunch may be emitted transverse to the shared beam path, and can then be collected using a reflective geometry to direct as many photons as possible from the interaction region towards the PMT.

The PDS originally installed at BECOLA in 2013 does well at collecting a large amount of the signal produced, and will from here be referred to as the "old system". An upgraded system was designed by collaborators at TU Darmstadt, with a strong emphasis on the rejection of the noise from stray laser light, which will hereafter be referred to as the "new system". In preparation for this experiment, simulations of the new system were performed to compare it to the old system. The simulations indicated that this new system would provide an increased sensitivity for the CaII measurement (see Table A.1 for detailed results of the simulations). The components were manufactured at TU Darmstadt and installed at BECOLA in the summer of 2017, and an identical system was also installed at TU Darmstadt. After installation of the new system, performance studies were carried out to evaluate the real-life performance of the two systems, and the new system was utilized for the online experiment.

2.3.2.1 Motivation

The old system at BECOLA involves an ellipsoidal reflector, as shown in Figure 2.13. The laser and ion beams pass in and out of the ellipsoid and cross a focal point of the ellipsoid. Light which is emitted at the focal point is focused to the second focal point of the ellipsoid, where the PMT is positioned. This system does an excellent job at collecting the resonant photons produced at the focal point, but the sensitivity could be improved through better noise rejection. The strategy of the old system is to increase the SNR by maximizing the signal. An alternative method of achieving a high SNR is to minimize the noise reaching the detector.

The new system utilizes an elliptical section, which spatially separates the signal from the noise. Unlike the old system which primarily collected photons emitted from the focal point of the ellipsoidal reflector, the elliptical reflector of the new system allows collection of photons from the entire section of beam passing through the detector, as the focal region of the elliptical reflector is a line instead of a point (see Figure A.6). The second focal region of this elliptical reflector is located just outside of the vacuum-enclosed beamline, just through a 5 in window. A pair of movable plates outside this window create a horizontal aperture which allows the focused signal to pass through, while blocking a majority of the background. Following this geometric cut, a compound parabolic concentrator (CPC) is used to reject photons which are entering with an angle of more than 20° from the normal. This angular cut further reduces the noise reaching the PMT, although it does come at the cost of some signal. A rendering showing the components of the new system is shown in Figure 2.13. Details about the optical simulations used to decide specific characteristics of the new system, including expected performance compared to the old system, can be found

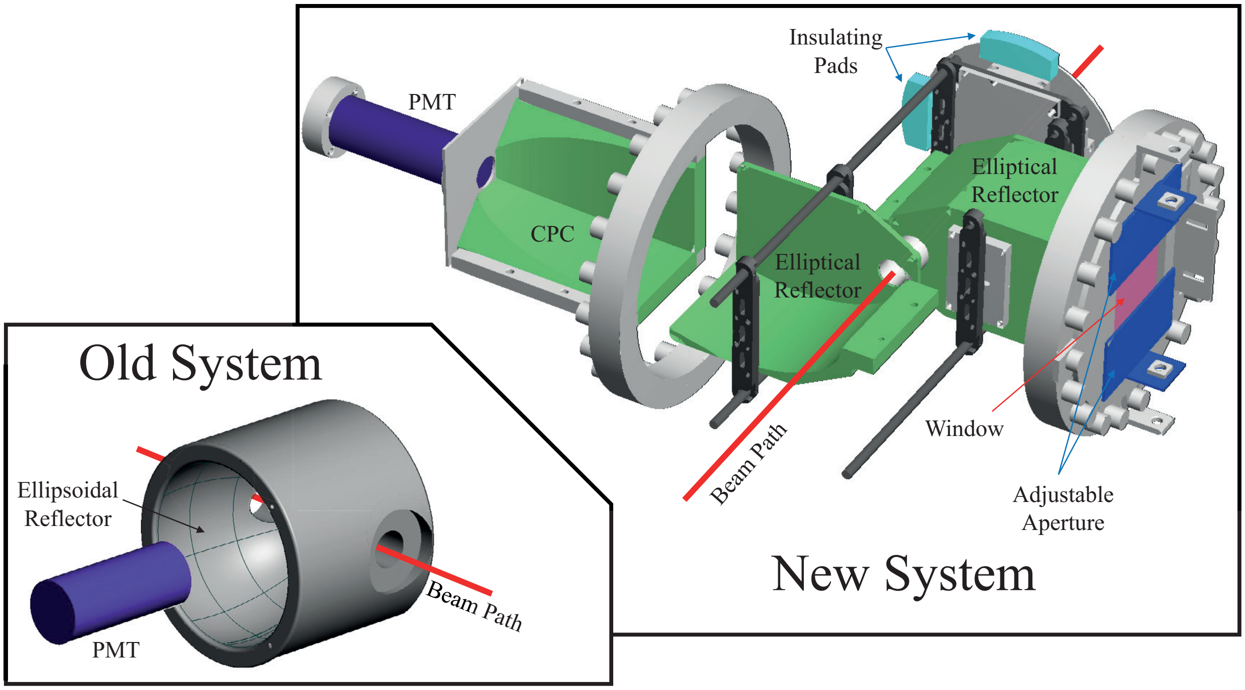
Insulating
Pads
PMT
Elliptical
Reflector
CPC
Elliptical
Reflector
Beam Path
Window
Adjustable
Aperture
New System
Old System
Ellipsoidal
Reflector
Beam Path
PMT

Figure 2.13: Renderings of both the old and new systems. The PMT of the old system is placed at the focal point of the ellipsoidal reflector. The new system image has two complete photon detection regions, each with their own elliptical reflector, aperture, CPC and PMT. To enable a better view of the design, the detection region closest to the viewer has had two pieces removed from both the elliptical reflector and the CPC (green). The detection region further from the viewer has had the CPC and PMT removed to allow a view of the adjustable aperture (dark blue) which sits just outside the window. Four rods support the two regions, and are held inside the beam pipe using four adjustable insulating feet on each end (cyan), in order to allow the scanning potential to be applied to the PDS.

in Section A.1.1.

2.3.2.2 Performance Studies

The fabrication, installation, and alignment procedure of the new system is covered in Section A.1.2. With both the previous and upgraded systems in place in the beamline, systematic tests were performed using stable beams at BECOLA. Optimization of the laser background in all three detection regions was performed by carefully aligning the laser. Unfortunately, the laser background in the three regions were each minimized at different alignments, making comparison difficult. This is likely due to a rotational misalignment of the old system, which cannot currently be adjusted. For comparison between the systems, an alignment was used which allowed all detection regions to be near to their minimum. In the actual experiment, the previous detection system was removed, allowing further alignment to lower the background rates in the two new detection regions.

The primary variable allowing us to gauge performance of the new system was the geometric cut (mask) following the elliptical reflector. An adjustable plate on each side allows a slit of variable width to be formed. It was expected that the elliptical chamber would focus the light to a single strip, so that the adjustable aperture (shown in Figure 2.13) could be configured to maximize the SNR (see Figure A.3 for the simulated configuration).

While one of the new detection regions had the slit at the focal plane opened as wide as possible, the width of the other was varied, and at each point the SNR between the two detection systems was compared. Surprisingly, the SNR simply increased as the slits were opened wider, as shown in Figure 2.14.

Due to this unexpected result, the intensity of signal across the focal plane was examined. To evaluate the intensity profile at the focal plane, the plates were adjusted to a 3 mm slit which was then moved along the Y-axis of the focal plane. This slit was scanned across the focal plane and at each position, the resonance of ^{40}Ca was measured. Because each measurement position requires a sufficiently high-quality scan of the calcium resonance line, a single scan of the slit across the focal plane takes a significant amount of time. To minimize the effect of any drift in the ion source intensity during this time, the slit position was adjusted on one of the new detection systems, while the other was held constant with the slit wide open. The SNR was then normalized by comparing to the wide open detection system. The results are shown in Figure 2.15 and an approximate profile expected from simulations is

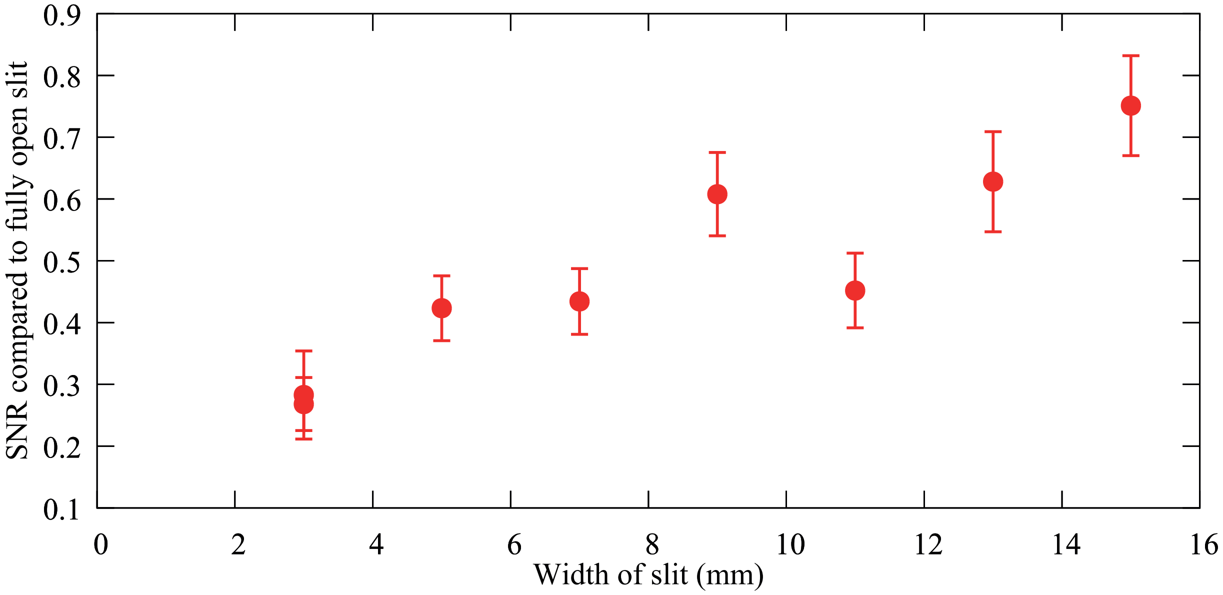

Figure 2.14: SNR results using various opening widths at the focal plane. The vertical axis is the SNR of the first detection region of the new system, normalized using the second detection region of the new system with the adjustable plates open as wide as possible. It was expected that the signal would be concentrated at the center of the focal plane, meaning that there would be a point where the SNR begins to decrease, as any wider opening only serves to allow more stray photons into the system. As shown, this was not the case. The wider the opening, the better the SNR becomes.

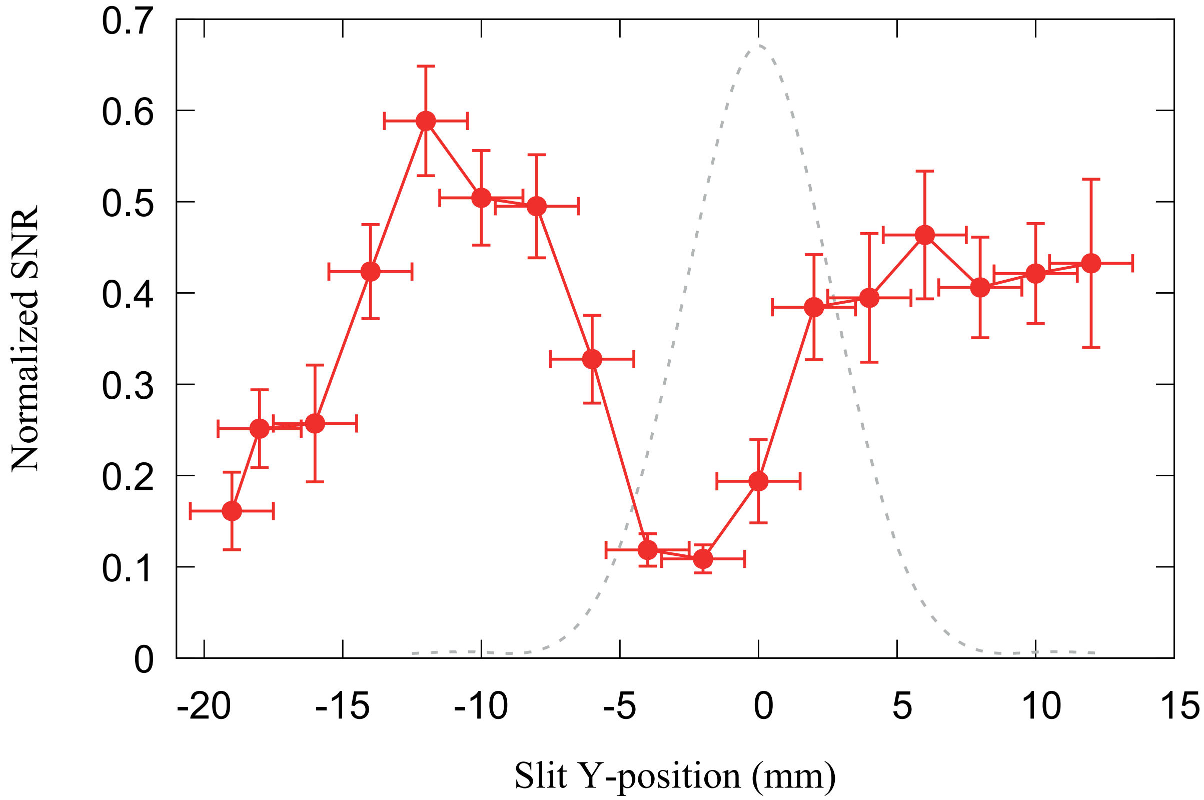

Figure 2.15: Results examining the SNR at various points along the Y-axis of the focal plane. The plates in one detection system were set to a 3 mm wide slit, and a calcium resonance was recorded with this slit at various positions along the Y-axis of the focal plane. The vertical axis is the SNR of the system being scanned, divided by the SNR of the control system. Red circles show the normalized SNR (compared to the other detection system which was used as a control), while the gray dotted line indicates the shape expected from the simulation. Rather than observing the signal concentrated into a single peak (see Figure A.3), the highest SNR was observed in two peaks on either side of the center. Further simulations to explore this behavior can be found in Section A.1.3.

shown as well. A double peak was observed, indicating an unexpected structure in the signal arriving at the focal plane. In addition, the peaks were also a bit wider than what was expected of the single peak.

To further optimize the SNR of the new system, several other masks were used to try and take advantage of the structure seen in Figure 2.15. In addition to varying the slit width, a strip of foil was placed at the center, effectively creating two slits, allowing for more noise

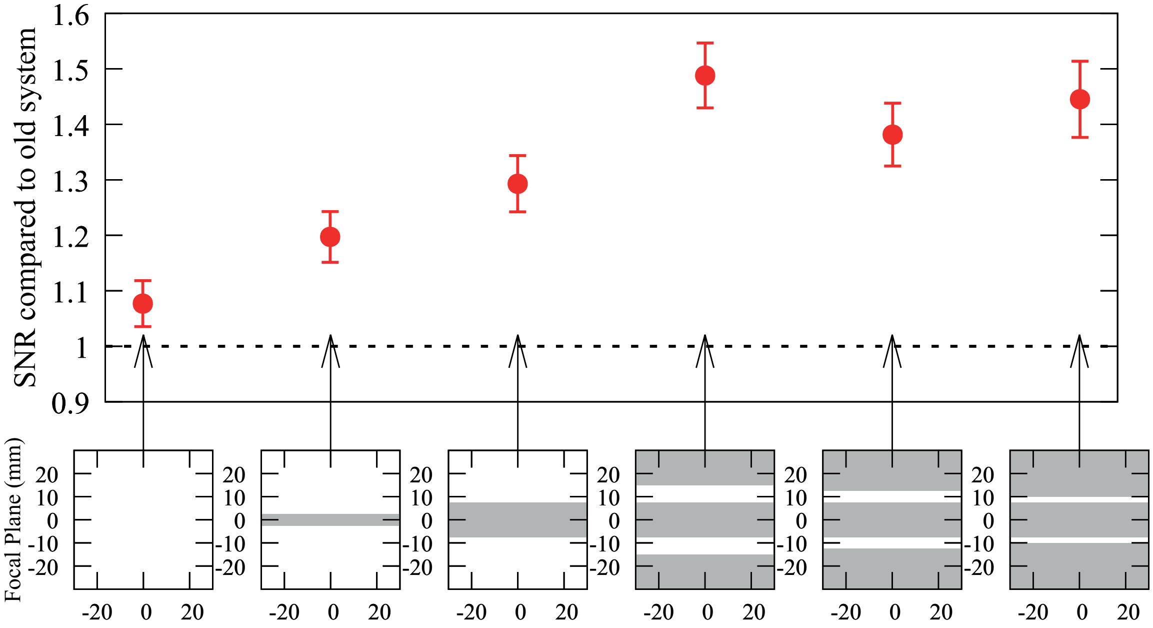

Figure 2.16: SNR results using various masks to select the two peaks seen at the focal plane. The vertical axis is the SNR of the new system, divided by the SNR recorded with the old system. The mask used for each measurement is shown underneath the plot, gray areas are where the focal plane was blocked, while white areas show the region of the focal plane where light was allowed to pass through the window. While the adjustable plates were used to block the top and bottom, a 5 mm or 15 mm wide strip of anodized foil was used to block the central portion. The focal plane is labeled along the X and Y axes with units of mm. Selecting the two regions of peak intensity seen in Figure 2.15 does provide a better SNR, but in all cases, even with the focal plane fully open, the SNR was more than that obtained using the old system.

rejection at the focal plane. This test was done with varying widths blocking the center, and various positions of the two adjustable plates. The results using these masks are shown in Figure 2.16. Although the SNR does increase, it was uncertain whether the double-peak structure seen at the focal plane would be stable to slight changes in alignment of the laser or ion beam. Because this thorough measurement of the intensity across the focal plane is not feasible during the online experiment due to the time constraints, it was decided to run the experiment without the foil blocking the center, and with the slits open as wide as possible, the left most condition in Figure 2.16. By simply using the aperture at the focal plane fully opened however, there is less possibility for a slight change of alignment during the online experiment to drastically reduce the SNR. This does still marginally improve the SNR over the previous system, but not quite to the extent expected from the simulations. This configuration still allows for a usable measurement of ^{36}Ca, especially considering the fact that there are two identical detection systems in the new installation. Further investigation of these behaviors was performed using simulations, and can be found in Section A.1.3.

Regardless of these unexpected behaviors at the focal plane, the new PDS was able to perform better than the old system for spectroscopy on Ca II in the offline tests (see Figure 2.16). With a proper behavior at the focal plane, it should be possible to increase the performance even further, however this may require a replacement of the reflecting foil used for the elliptical reflector, or a better alignment of the system to the ion and laser beam. In cases where the charge exchange cell is required for the measurement, it is expected that the new system will perform worse than the old system (see Table A.1), so having both systems available is still a necessity.

Chapter 3

Analysis

Rare isotope beams were sent to BECOLA from October 7th, through October 15th, 2017. The data obtained were calibrated, and the hyperfine spectra were used to extract the nuclear moments and charge radii.

3.1 Calibration

For past experiments at BECOLA, calibration has been performed using a single, stable isotope. As the frequency is scanned using a Doppler shift, it is crucial to determine both the laser frequency, as well as the energy of the ion beam with high precision. When released from the cooler/buncher, the ions are extracted with a potential that is $10\,\mathrm{V}$ lower than the minimum potential of the trap. As the ions leave the helium-filled trap, some residual cooling can occur, allowing the absolute energy of the beam to be offset from the nominal difference between the potential at the interaction region and the potential of the trap. In the past, this behavior was examined by recording the potential of the trap, and using the known absolute transition frequency of a stable isotope to determine the offset in voltage which occurs during the release of the beam.

Due to the variety of stable Ca isotopes available, the decision was made to instead use the measured centroids of two stable isotopes, ^{40,44}Ca for calibration during the experiment. By using the known isotope shift between ^{40,44}Ca, the release potential can be extracted without relying on the measurement using a high voltage divider. This technique has the added advantage that, as these measurements are made throughout the experiment, the actual variation in the isotope shift measurement is obtained, as opposed to simply recording the fluctuations of an absolute measurement. This allows for a better understanding of the systematic fluctuations taking place over the duration of the experiment.

Every two or three hours during the experiment, a measurement of ^{40}Ca and ^{44}Ca was taken using the PIG ion source. As an ion bunch leaves the trap, some residual cooling may occur as the ions are accelerated out of the trap, resulting in an uncertainty of approximately 10 V. By utilizing two reference isotopes however, this primary source of uncertainty was reduced by a factor of two, and was limited instead by fluctuations of the high voltage power supply throughout the course of the experiment.

The calibration of the data was performed as follows:

The scanning voltage was recorded with a high precision digital volt meter (DVM), Keysight Technologies 34465A, at each scanning position during the run. Because of this, measurements taken at the same voltage step may each have a slightly different voltage recorded in the data. Measurements from each run were sorted into voltage bins with a width of 0.998 964 19 V, and the bin centers were selected for each run to ensure that the sum of all deviations (between the DVM voltage and the center of the bin where that measurement was placed) was zero. The deviation of the bin width from 1 V was due to the fact that when requesting a scanning voltage of ±1000 V from the system, $\sim \pm 999$ V are measured.

For each reference measurement taken, the beam energy was converted into frequency, and the the known shift between these isotopes ($\delta\nu^{40,44} = 850.231(65)$ MHz [48]), was used to determine the precise energy of the ion beam. This calibration was performed using the spectra recorded by the upstream detector (channel 1), as there was more laser background present in the downstream detector (channel 2). For the rare isotope measurements, the weighted average of the neighboring reference measurements were used to shift the beam energy (voltage) of each run. The edges of each bin were converted into frequency using the Doppler shift and set laser frequency. This same voltage shift was then applied to the neighboring reference measurements of ^{40}Ca, and the weighted average of the centroid frequencies was used to offset the frequency of each bin in the rare isotope data.

Finally, now that the rare isotope data has been calibrated and converted to a relative frequency (using the preceding and following calibration measurements) these histograms were combined into a single histogram for each rare isotope and detector. An uncertainty for each voltage calibration was obtained based on the statistical precision of the reference measurements used to deduce the shift, as well as the fluctuation in voltage shifts between each reference measurement. This systematic uncertainty accounts for fluctuations in the cooler/buncher potential, as well as fluctuations in the laser frequency, as it depends directly on the variations in the reference measurements throughout the experiment.

The data from the two detection regions were not combined, rather, they were fit separately and the fit parameters were then averaged, with weighting based on the uncertainty.

3.2 Hyperfine Spectra

3.2.1 Fitting Function

After converting the resonance spectra from voltage to frequency, the peaks were fitted using an asymmetric pseudo-Voigt function. A true Voigt function is a convolution of a Gaussian and Lorentzian lineshape, due to the combination of Doppler and collision broadening, and the natural lineshape, respectively [49]. The pseudo-Voigt function employs a linear combination of a Gaussian and Lorentzian, in order to serve as a closed-form approximation to the Voigt function. For this experiment, the pseudo-Voigt used was of the form

$$I(\nu) = \eta L(\nu) + (1 - \eta) G(\nu) \tag{3.1}$$

where I is the intensity of the resonance as a function of frequency ν, η $(0 < \eta < 1)$ describes the combination of the Lorentzian and Gaussian components, L and G, whose lineshapes depend on the total area under the peak A_0, the centroid frequency ν_0, and the total FWHM γ_0. the Lorentzian and Gaussian functions are

$$G(\nu) = \frac{2A_0}{\gamma_0}\sqrt{\frac{\ln{(2)}}{\pi}}e^{-4\ln{(2)}\left(\frac{\nu-\nu_0}{\gamma_0}\right)^2} \tag{3.2}$$

$$L(\nu) = \frac{2A_0}{\pi\gamma_0}\frac{1}{1+4\left(\frac{\nu-\nu_0}{\gamma_0}\right)^2} \tag{3.3}$$

To approximate a true Voigt function, η and γ_0 have a complicated relationship to the FWHM of the Lorentzian and Gaussian functions which are convoluted [50]. Because we are focused on extracting the centroids of each peak, the true widths of the deconvoluted Gaussian and Lorentzian are not of interest so this analysis simply uses the values of η and γ_0 in the fitting process.

Because of collisions when exiting the cooler/buncher, there is a possibility of some asymmetry present in the spectrum. Energy can be lost during the exit, and thus a low energy tail may be present. To account for asymmetry using the above definition of the pseudo-Voigt, a function of the frequency is used in place of γ_0, resulting in one side having a wider lineshape than the other [51].

$$\gamma(\nu) = \frac{2\gamma_0}{1 + e^{a(\nu-\nu_0)}} \tag{3.4}$$

This adds an additional parameter a, which asymmetrically affects the shape of the spectrum.

3.2.2 Fitting Procedure

The lineshape of this asymmetric pseudo-Voigt function is determined by the a and η, and in the case of ^{36,38}Ca, these parameters were constrained to match those obtained from the ^{40}Ca calibration runs ($\eta = .66$, $a = 0.0007$). Due to the longer running times, fluctuations in the high voltage of the cooler/buncher can lead to a wider resonance than the reference measurements, which are taken in less than 1 h, and so the widths (γ_0) of ^{36,38}Ca were each free parameters. While the reference measurements had a typical linewidth of 75 MHz, the linewidth of ^{36}Ca was 80 MHz.

3.2.2.1 Hyperfine coupling constants

In the case of ^{37,39}Ca, the unpaired neutron results in a non-zero ground-state nuclear spin. As described in 2.1.3, the interaction between the electron and nuclear spin leads to a hyperfine splitting of the $4s\ ^2S_{1/2} \leftrightarrow 4p\ ^2P_{3/2}$ transition. These can be seen in Figures 3.2 and 3.4. All six peaks of these hyperfine spectra were fit using a common lineshape and width, with their centroid positions given from the three hyperfine coupling constants as described in Section 2.1.3. For these transitions between hyperfine levels, the transition probability (and thus the relative intensity of each spectral line) can be determined from the Clebsch-Gordan coefficients linking the lower and upper states. This calculation does require a consideration of the helicity of the laser light used to excite the transition, but because ^{37,39}Ca were measured under the same laser conditions (power and polarization) the lineshape and relative intensities of ^{39}Ca should match those of ^{37}Ca. Another constraint, which can be used when comparing isotopes, is the ratio of the A^{hf} coupling constants of the upper and lower state. In this ratio, the nuclear factors from the magnetic moment and spin cancel out, and the only remaining contribution to this ratio comes from B_0 of each state, which will not vary between isotopes. The ratio of the A^{hf} constants and the relative intensity of each peak were used as constraints in the fitting of ^{37}Ca, because of the excellent statistics of the ^{39}Ca measurement,.

No constraints were placed on the hyperfine coupling constants of ^{39}Ca when fitting the spectrum. The obtained values are shown in Table 3.1. Interestingly, the $A^{\text{hf}}(^2S_{1/2})$ and $A^{\text{hf}}(^2P_{3/2})$ had a ratio of 26.24(4), which deviates from previous experimental results of 25.92(3) [52]. The reason for this discrepancy is not known. An examination of our data for sources of possible systematic differences that could explain the difference in this ratio were unsuccessful. A greater uncertainty in the absolute voltage of the system, the laser frequency, or even an angle between the ion and laser beams cannot account for this discrepancy because of the fact that it is a ratio. Although these variables do have an effect on the values of $A^{\text{hf}}(^2S_{1/2})$ and $A^{\text{hf}}(^2P_{3/2})$, their ratio is highly insensitive to these sources of systematic uncertainty in our experimental setup. Because of this unexplained discrepancy, an inflated systematic uncertainty is included with the reported hyperfine coupling constants for ^{39}Ca.

3.2.3 Results

The resulting fits of ^{36,37,38,39}Ca, using the data collected from the upstream detector, are shown in Figures 3.1– 3.4, along with the residuals. A typical example of the twenty reference

Table 3.1: The obtained hyperfine coupling constants of ^{37,39}Ca for the $4s\ ^2S_{1/2}$ and $4s\ ^2P_{3/2}$ states. The statistical and systematic uncertainties are reported in the first and second parentheses, respectively. The systematic uncertainty comes from the high voltage calibration, and also the deviation of the A^{hf}-factor ratio measured for ^{39}Ca from the literature value from ^{43}Ca. This unexplained discrepancy is the dominant source of systematic error.

		A (MHz)		B (MHz)
A	I^π	$^2S_{1/2}$	$^2P_{3/2}$	$^2P_{3/2}$
37	$3/2^+$	+1064.5(103)(08)	+40.57(39)(27)	−22.9(163)(05)
39	$3/2^+$	+1457.20(14)(34)	+55.53(9)(32)	+5.79(26)(32)

measurements for ^{40,44}Ca is shown in Figures 3.5 and 3.6. The same fits were performed using data from the downstream detector, and the results were combined using a weighted average.

3.3 Nuclear Moments

While the nuclear moments are not the focus of this thesis, their results are briefly presented here.

Assuming B_0 and V_{zz} to be constant between isotopes and neglecting the hyperfine anomaly [37], a simple ratio between isotopes using Equations 2.6 and 2.7 provides the following determination of the nuclear moments:

$$\mu = \mu_{\mathrm{R}} \frac{A^{\mathrm{hf}}}{A^{\mathrm{hf}}_{\mathrm{R}}} \frac{I}{I_{\mathrm{R}}} \tag{3.5}$$

$$Q = Q_{\mathrm{R}} \frac{B^{\mathrm{hf}}}{B^{\mathrm{hf}}_{\mathrm{R}}}. \tag{3.6}$$

Where the subscript R refers to the reference nucleus, whose hyperfine coupling constant of the same atomic state, nuclear moment, and nuclear spin are known. The known values of

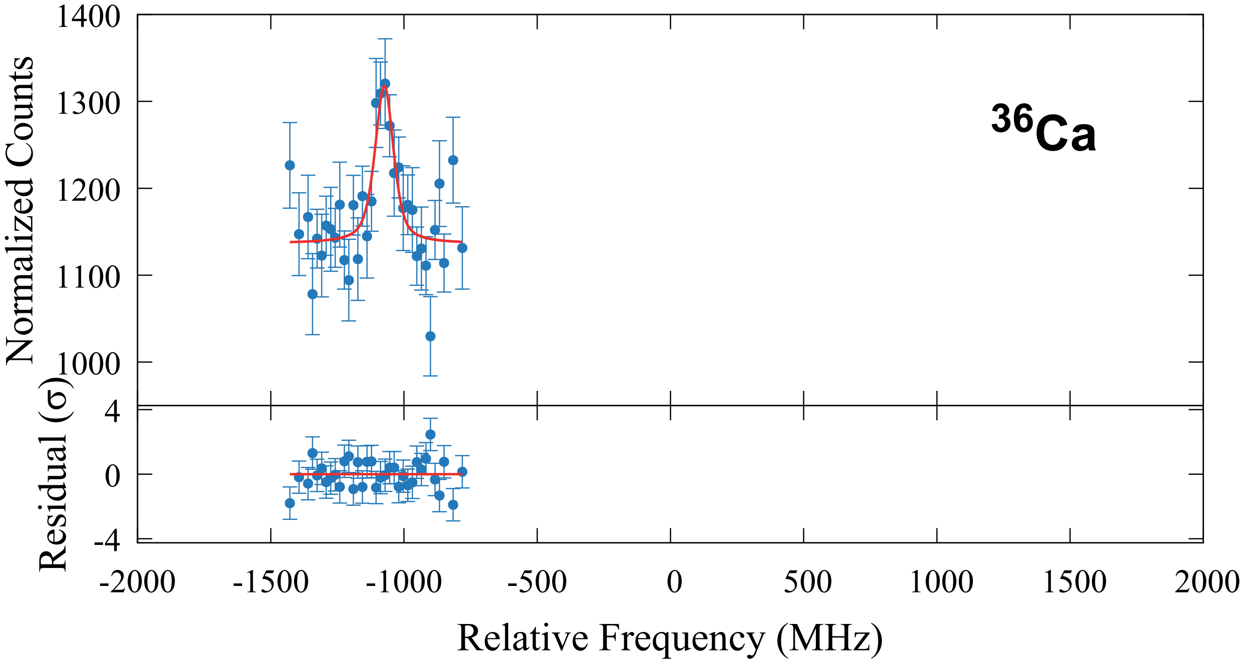

Figure 3.1: The spectrum measured for ^{36}Ca, along with the residuals from the fit using a pseudo-Voigt function as described in Section 3.2.

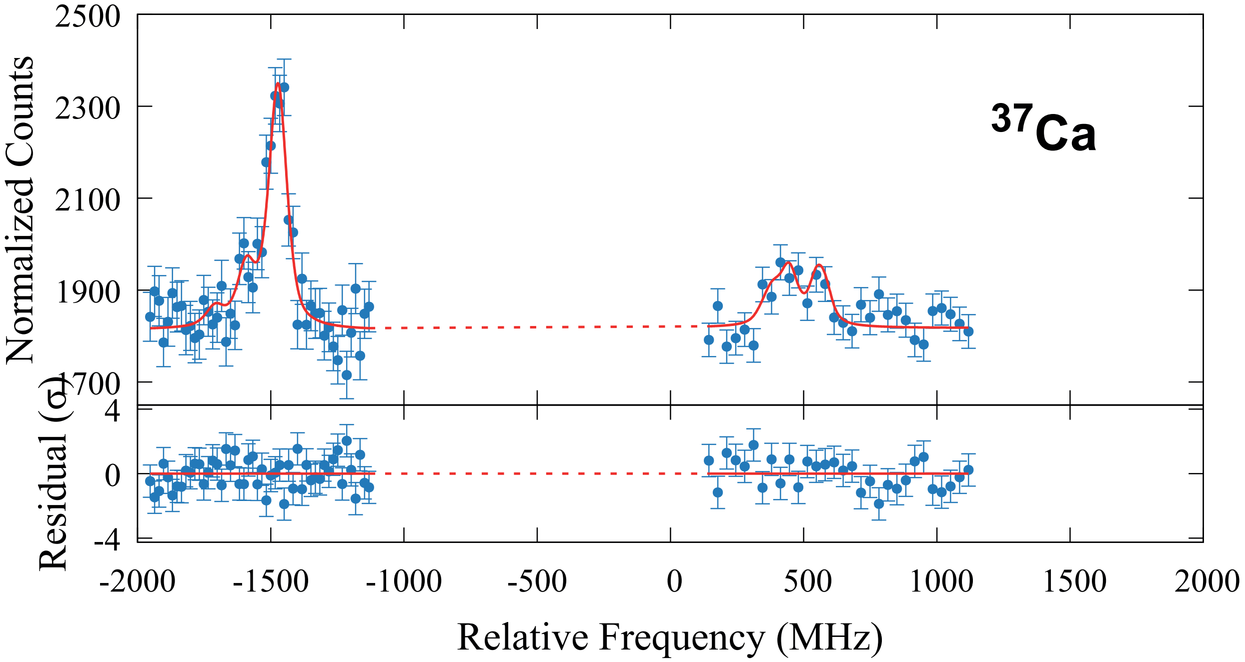

Figure 3.2: The hyperfine spectrum measured for ^{37}Ca, along with the residuals from the fit using six pseudo-Voigt functions as described in Section 3.2.

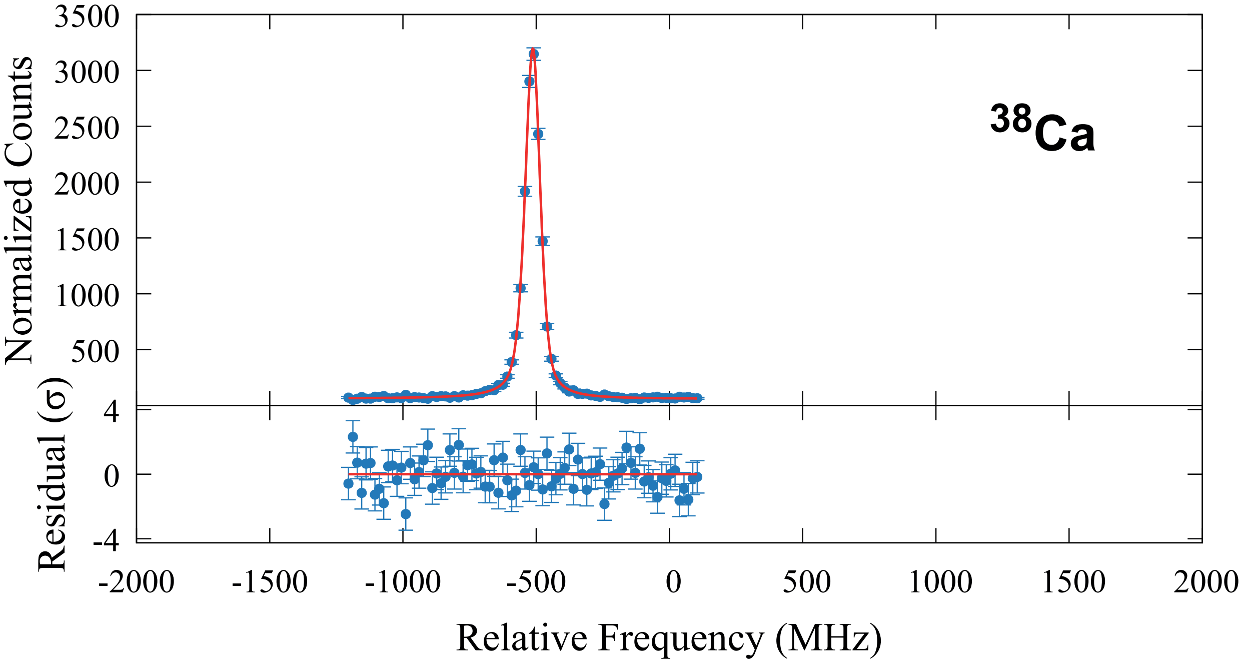

Figure 3.3: The spectrum measured for ^{38}Ca, along with the residuals from the fit using a pseudo-Voigt function as described in Section 3.2.

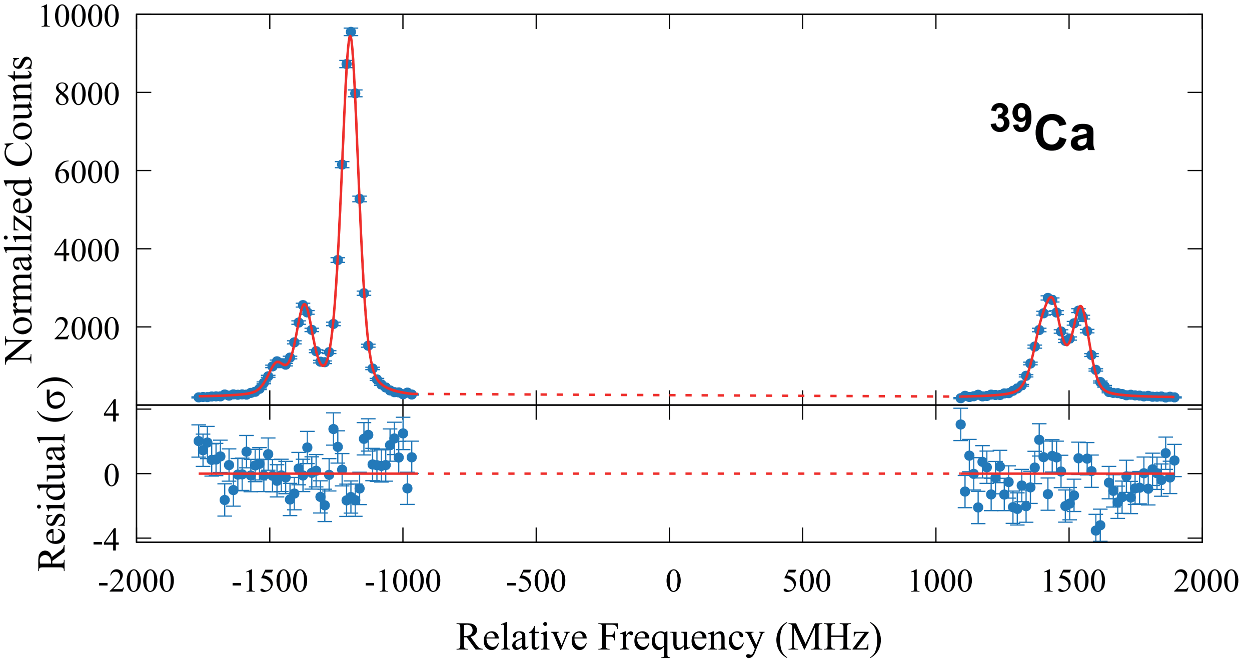

Figure 3.4: The hyperfine spectrum measured for ^{39}Ca, along with the residuals from the fit using six pseudo-Voigt functions as described in Section 3.2.

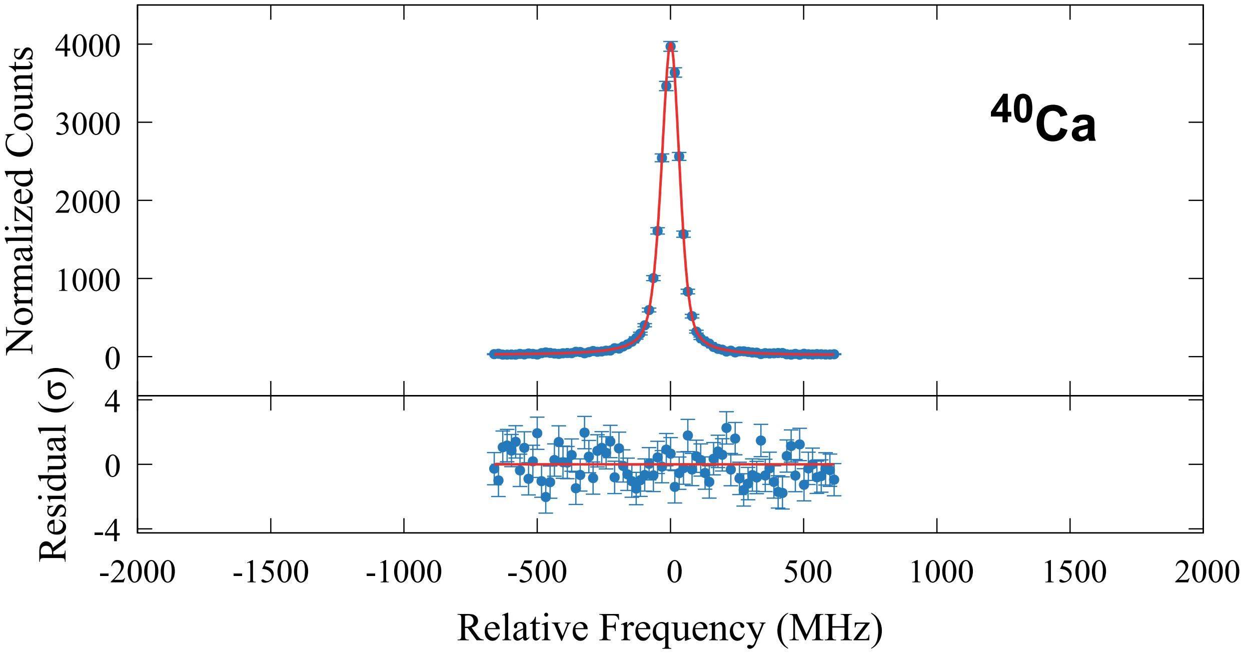

Figure 3.5: A typical spectrum measured for the reference ^{40}Ca, along with the residuals from the fit using a pseudo-Voigt function as described in Section 3.2.

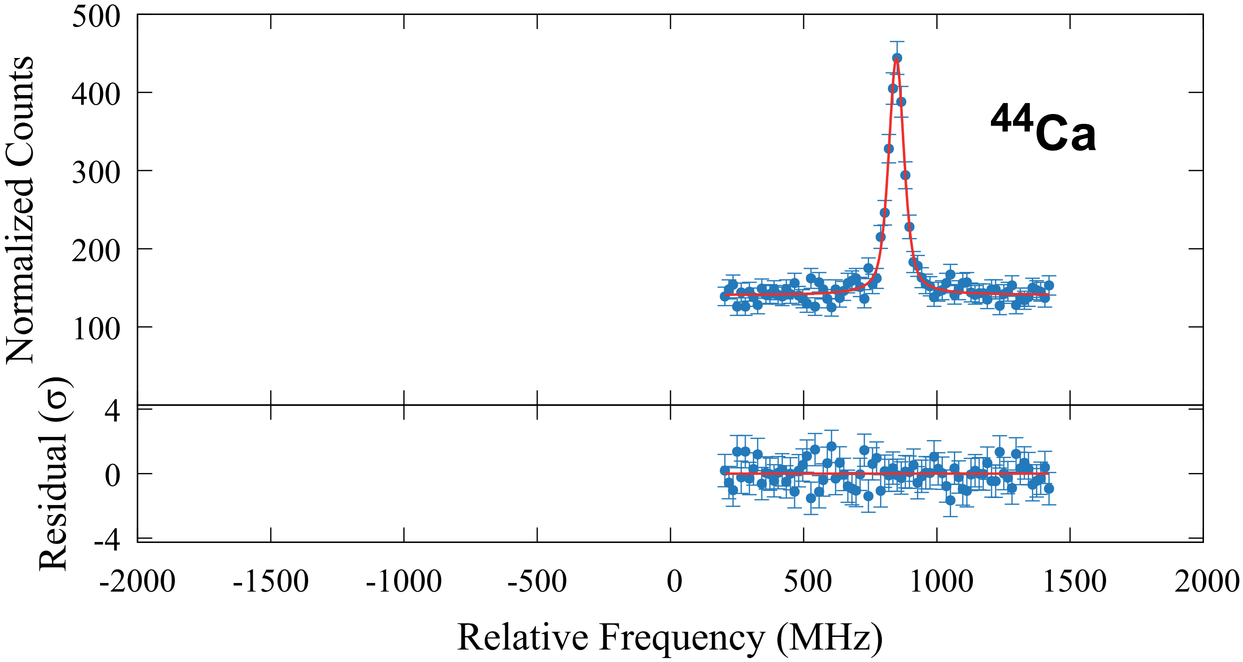

Figure 3.6: A typical spectrum measured for the calibration ^{44}Ca, along with the residuals from the fit using a pseudo-Voigt function as described in Section 3.2.

^{43}Ca II$(I = 7/2)$, $A^{\mathrm{hf}}_{\mathrm{R}}(^2S_{1/2}) = -806.402\,071\,60(8)$ MHz [53] and $\mu_{\mathrm{R}} = -1.317643(7)\mu_N$ [54], were used with the above ratio to derive the magnetic moments of ^{37,39}Ca. A precise measurement of $B^{\mathrm{hf}}_{\mathrm{R}}(^2P_{3/2})$ does not exist however, so the spectroscopic electric quadrupole moments of ^{37,39}Ca were derived from Equation 2.7 using a theoretical value of $eV_{zz} = 1.513(7)\,\mathrm{MHz/fm}^2$ [55]. The resulting nuclear moments are shown in Table 3.2. For a complete discussion of these results, including the an examination of the doubly-magic nature of ^{36}Ca, please refer to ref. [37].

Table 3.2: The nuclear moments of ^{37,39}Ca obtained in this work. The total uncertainty is reported in the parentheses. $Q(^{39}\mathrm{Ca})$ is in agreement with the previous experimental value of 3.6(7) e^2fm^2 [56], although the sign of $Q(^{39}\mathrm{Ca})$ is experimentally determined here for the first time. $\mu(^{39}\mathrm{Ca})$ reported here does not take into account the hf anomaly, which the previous and more precise β-NMR measurement, +1.0217(1) μ_N [57], is insensitive to. For more discussion of these results, see ref. [37].

A	I^π	μ (μ_N)	Q (e^2fm^2)
37	$3/2^+$	+0.7453(72)	-15(11)
39	$3/2^+$	+1.0204(3)	+3.82(27)

3.4 Charge radii

The measured spectra shown in Section 3.2 were used to extract the charge radii of ^{36,37,38,39}Ca relative to ^{40}Ca. Variation in the differential mean-square charge-radius can be determined by a careful evaluation of the isotope shift.

3.4.1 Isotope shift

When comparing an atomic transition in two isotopes of the same element, the energy or frequency of the transition undergoes a slight change, due to the change in the mass and size of the nucleus. This difference in frequency between an isotope A and A' is known as the isotope shift (IS),

$$\delta\nu^{AA'} = \nu^{A'} - \nu^{A}. \tag{3.7}$$

The variation between these isotopes arises from two primary sources, the mass shift (MS) due to the change in mass of nucleus, and the field shift (FS) from the change in the volume of the electric field at the nucleus

$$\delta\nu_{\mathrm{IS}}^{AA'} = \delta\nu_{\mathrm{MS}}^{AA'} + \delta\nu_{\mathrm{FS}}^{AA'} \tag{3.8}$$

An excellent explanation of these contributions to the IS can be found in ref. [22], and are summarized in Figure 3.7. To extract the charge radii, the field shift term is of primary interest. Here, the specific factors used for Ca will be discussed.

The mass shift can be expressed as

$$\delta\nu_{\mathrm{MS}}^{AA'} = \frac{M_A - M_{A'}}{M_A M_{A'}}(K_{\mathrm{NMS}} + K_{\mathrm{SMS}}) \tag{3.9}$$

where K_{NMS} and K_{SMS} are the normal mass shift and specific mass shift coefficients respectively, and M represents the mass of the isotope. In the case of medium-mass nuclei, where the relativistic corrections and screening effects don't need to be considered [22], the field shift can be represented as

$$\delta\nu_{\mathrm{FS}}^{AA'} = F\delta\langle r_c^2\rangle^{AA'} \tag{3.10}$$

where $\delta\langle r_c^2\rangle^{AA'}$ is the difference of the mean-square charge radius between nuclei A and A'. The field shift coefficient, F, must be determined for the specific element and transition being studied. Due to the necessity of an interaction between the charge volume of the nucleus and the wavefunction of the electron, this field shift coefficient is largest for transitions involving s type electron orbitals, as they have more likelihood of being found within the nucleus. This coefficient F does have some slight variation between isotopes [58], however in the case of these medium-mass nuclei, it is small enough to be negligible, allowing the isotope shift to be expressed as

$$\delta\nu_{\mathrm{IS}}^{AA'} = \frac{M_A - M_{A'}}{M_A M_{A'}}(K_{\mathrm{NMS}} + K_{\mathrm{SMS}}) + F\delta\langle r_c^2\rangle^{AA'} \tag{3.11}$$

3.4.2 King plot

One major benefit of studying the Ca isotopic chain is the thorough research which has been performed on the stable isotopes. By dividing each side of Equation 3.11 by $(M_A - M_{A'})/M_A M_{A'}$ a linear relationship can be obtained between the isotope shift and the ms charge radius

$$\delta\nu_{\mathrm{IS}}^{AA'}\frac{M_A M_{A'}}{M_A - M_{A'}} = k + F\frac{M_A M_{A'}}{M_A - M_{A'}}\delta\langle r_c^2\rangle^{AA'} \tag{3.12}$$

allowing the mass shift coefficient $k = K_{\mathrm{NMS}} + K_{\mathrm{SMS}}$ to be extracted from the intercept, and the field shift coefficient to be extracted from the slope.

Plotting isotopes with a known differential mean-square charge radius and isotope shift in such a manner is known as a King plot [60]. This technique can be used even when absolute charge radii are not known, by allowing a ratio of the atomic factors between two different transitions to be obtained, as is shown in Figure 3.8. For some elements, the precision obtained by such a linear fit is insufficient due to few isotopes or a small variation in isotope shift or charge radius. This would then require the use of semi-empirical calculations to

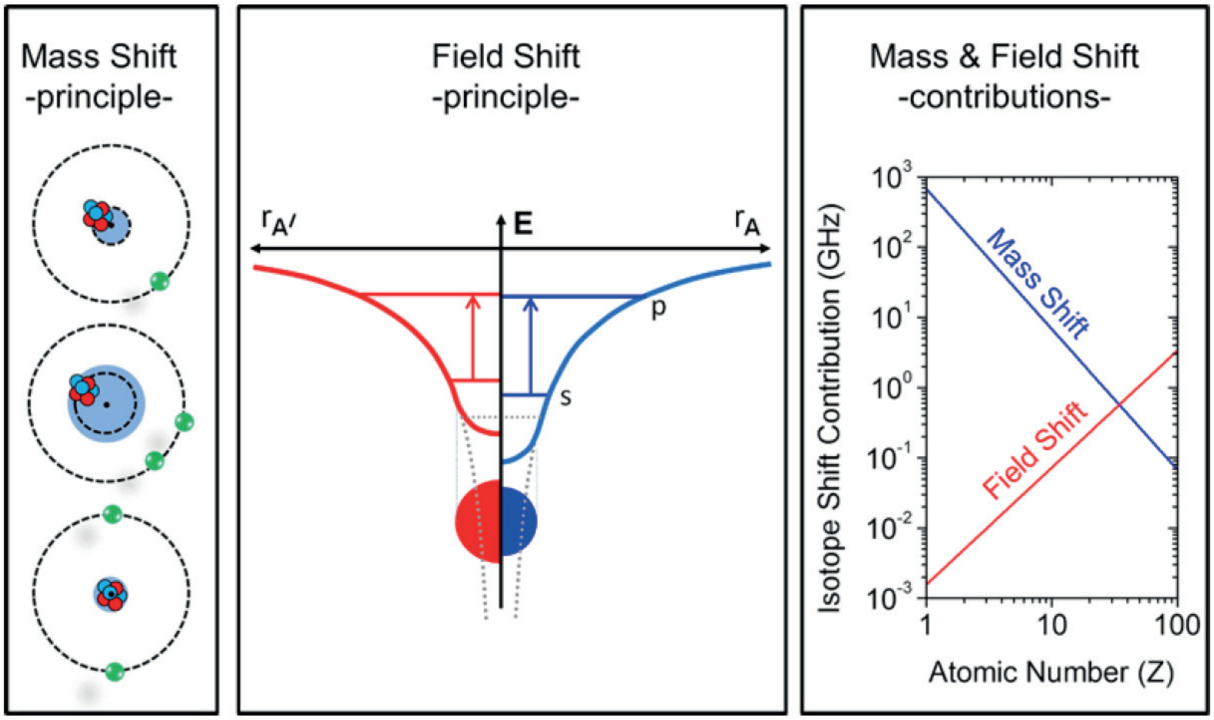
Mass Shift
-principle-
Field Shift
-principle-
$r_{A'}$
E
r_A
p
s
Mass & Field Shift
-contributions-
Isotope Shift Contribution (GHz)
10^3
10^2
10^1
10^0
10^{-1}
10^{-2}
10^{-3}
Mass Shift
Field Shift
1
10
100
Atomic Number (Z)

Figure 3.7: Diagram from ref. [22] describing the mass shift and field shift principle. The left panel shows the mass shift. At the top, is a representation of the normal mass shift (NMS) which arises from the balance of momentum between the nucleus and each electron, while the middle and lower diagrams depict the specific mass shift (SMS) which varies depending on the momentum correlation between the electrons in the atomic system. The center panel describes the field shift. A pure Coulomb potential for a point-like nucleus is shown by the dotted line. Variations in the charge volume of the nucleus affect the energy levels of the electrons due to the probability of the electrons being within the nucleus. The horizontal dotted line represents the energy of an *s*-electron for a point-like nucleus, while the red and blue levels on the left and right show the energy levels shifted due to the volume of the nucleus A' and A respectively. The right section provides an idea of the relative contribution to the isotope shift of each effect, versus the atomic number. As the field shift is the component sensitive to the charge-radius, the charge radius becomes difficult to extract for lighter isotopes, where the mass shift dominates.

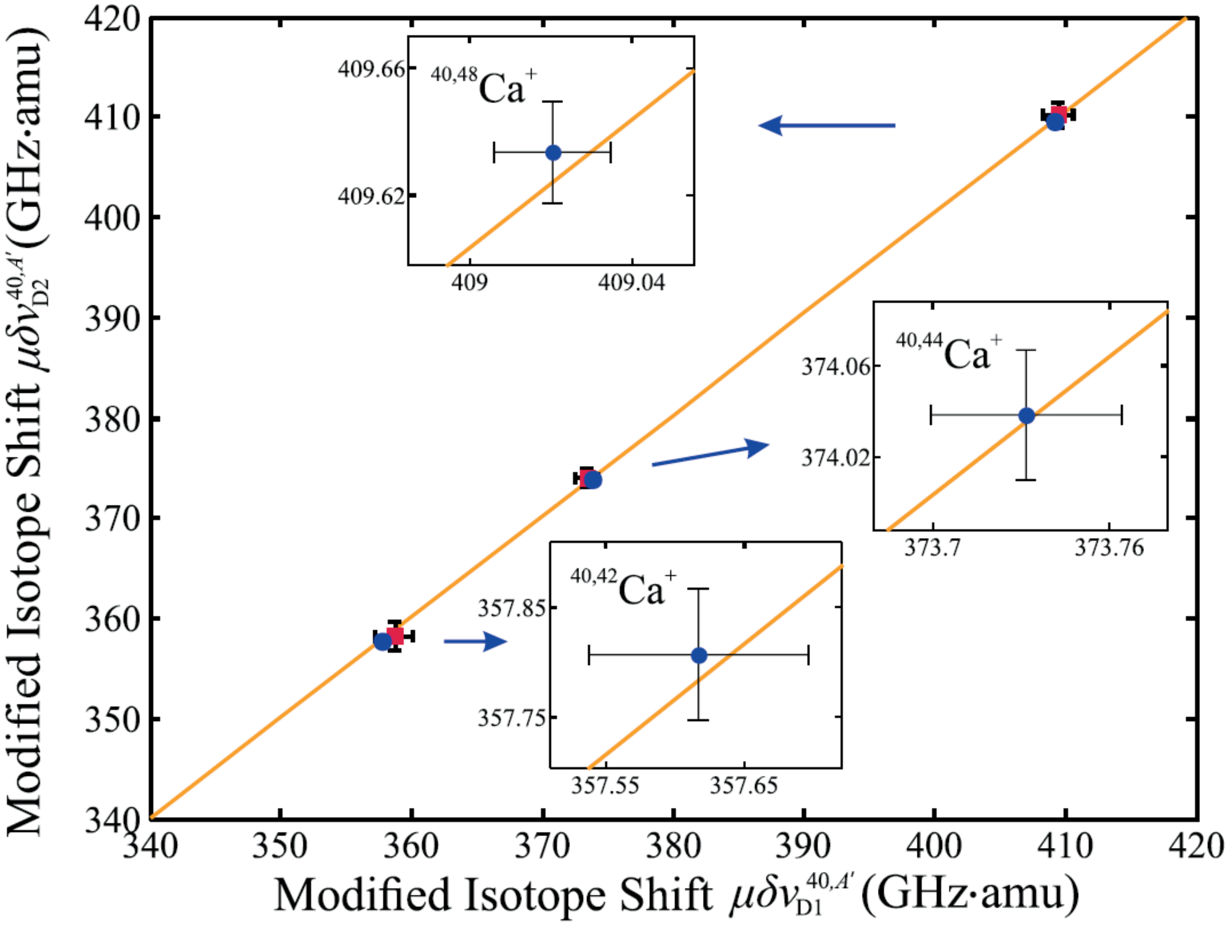

Figure 3.8: King plot from ref. [59] comparing the modified isotope shift of the D1 and D2 transitions in Ca. Previous data points are shown in red, while the blue circles are those measured in that work. Both the vertical and horizontal axes are plotting the "modified" isotope shift, which is the left hand side of Equation 3.12. Here μ represents the expression involving the masses. The high degree of precision and the excellent linearity of the points gives good cause to neglect higher order effects which may cause F to vary between isotopes.

deduce the atomic factors, such as in the case of the Fe measured recently at BECOLA [21]. In the case of Ca, however, the King plot has been used to extract these atomic factors with much higher precision than empirical calculations are able to provide. The atomic factors of the $^2S_{1/2} \leftrightarrow {}^2P_{3/2}$ (D2) transition were determined to be

$$k = 409.5(42)\,\mathrm{GHz\,amu} \tag{3.13}$$

$$F = -284.7(82)\,\mathrm{MHz/fm^2} \tag{3.14}$$

from a 3-dimensional King plot involving both the D1 and D2 transitions [59], and were used in the present study.

3.4.3 Results

Using these precise evaluations of the atomic factors for the D2 transition, and the centroid position of each isotope's spectrum in Section 3.2.2, the differential mean-square charge radius can be obtained. The absolute charge radii of each isotope can then be obtained using the experimentally known radius of ^{40}Ca. The rms charge radius of ^{40}Ca, 3.4776(19) fm^2 [4], has been obtained from a combination of electron scattering, muon scattering, and optical isotope shift data as described in ref. [4]. A combination of the electron and muon scattering data for ^{40}Ca listed in ref. [61] was performed using the *EXCEL* formula described in ref. [61]. Following this, two methods of combined analysis of the absolute scattering measurements and optical isotope shifts between stable Ca isotopes were used as described in refs. [62, 63]. These allow the absolute, model-independent scattering data to be constrained by the precise, relative optical isotope shift measurements.

These results are shown in Table 3.3, and plotted in Figure 4.1 along with several the-

Table 3.3: Isotope shifts, deduced differential mean-square charge radii, and absolute charge radii. The numbers in parentheses are the statistical and systematic uncertainties, respectively. The differential ms charge radius of ^{39}Ca relative to ^{40}Ca is consistent with the previous value of $-0.127(20)\,\mathrm{fm}^2$ [64]. Rms charge radii were obtained using the charge radius of ^{40}Ca 3.4776(19) fm from ref. [4].

A	$\delta\nu^{40,A}$ (MHz)	$\delta\langle r^2\rangle^{40,A}$ (fm^2)	R (fm)
36	−1073.8(60)(43)	−0.196(21)(16)	3.449(3)(3)
37	−766.1(47)(49)	−0.205(15)(17)	3.448(2)(3)
38	−513.1(3)(17)	−0.0797(11)(63)	3.4661(2)(21)
39	−230.5(2)(18)	−0.1060(7)(64)	3.4623(1)(21)

Table 3.4: Sources of uncertainty in the differential ms charge radii, $\delta\langle r^2\rangle^{40,A}$. Statistical uncertainty comes from the fit of the spectra. The calibration uncertainty is from the fluctuations in the extracted calibration voltage, described in Section 3.1. Atomic factor uncertainty is due to the total uncertainty from the atomic factors, k and F as noted in Equations 3.13 and 3.14.

A	Statistical (fm^2)	Calibration (fm^2)	Atomic factors (fm^2)
36	0.021	0.0151	0.004
37	0.015	0.0172	0.003
38	0.0011	0.0060	0.002
39	0.0007	0.0063	0.001

oretical models. The systematic uncertainties for the differential ms charge radii come primarily from the calibration uncertainty described in Section 3.1, and are shown in detail in Table 3.4. When deducing the absolute charge radii, the uncertainty in the known value of $R(^{40}\mathrm{Ca})$ also contributes. While ^{36,37,38}Ca are first-time measurements of the charge radii, $\delta\langle r^2\rangle^{40,39}$ has been determined previously as $-0.127(16)\,\mathrm{fm}^2$ [64]. Our result for ^{39}Ca ($-0.1060(7)(64)\mathrm{fm}^2$)is in agreement with the previous measurement, and reduces the uncertainty by a factor of 3.

These charge radii lighter than the $N = 20$ shell closure tend to become smaller as neutrons are removed, which is a different behavior to the increase observed below the

$N = 28$ shell closure. Although this type of steady trend across the shell closure has been observed in neighboring elements Ar and K [65] [23], an understanding of this weakening of the shell closure has only been explained qualitatively as a balance of the monopole and quadrupole proton-core polarizations on either side of $N = 20$, and was not modeled well by existing models of charge-radii [23].

Chapter 4

Discussion

4.1 Modeling charge radii

Nuclear Density Functional Theory (DFT) has been used with great success to reproduce important features in ground-state observables, including magic number “kinks” in charge radii, and binding energies of nuclei [25, 66]. The self-consistent mean-field method provides a valuable description of complex, many-body, nuclei which are beyond the reach of *ab initio* methods due to computational limitations. DFT models employ an effective interaction which serves as a substitute for the true nucleon-nucleon interaction, and the expectation value of the energy is then minimized [67]. The approach is similar to the DFT used in electronic systems [68], however, in electronic systems, *ab initio* calculations have been able to derive robust energy functionals. In nuclear DFT, the composite structure of the nucleon has prevented a useful direct derivation of energy functionals, rather the form of the most effective energy functionals is derived based on various considerations, and their parameters are determined using fits to empirical nuclear data [66, 69]. This phenomenological approach requires careful consideration of the form of the functional, and the experimental values used to parametrize the model.

Several DFT models are compared to the experimental data in Figure 4.1. One form is the Skyrme energy density functional, which has been used for over 40 years [70]. Here, the SV-min (HFB) parametrization [69] of this functional was compared to the new experimental values. This parametrization uses 224 experimental data points including binding energies, diffraction radii, surface thickness, charge radii, and spin-orbit splitting. While this functional does an adequate job describing the overall trend of the radii, local fluctuations, such as the odd-even staggering and minima at the magic numbers ($N = 20, 28$) are not well described.

The second functional used is the more modern Fayans model, which adds surface and pairing terms, which are dependent on nuclear density gradients [25, 67]. In addition to the 224 data points used in the SV-min parametrization, differential ms charge radii of Ca isotopes ($\delta\langle r^2\rangle^{48,40}$, $\delta\langle r^2\rangle^{48,44}$, and $\delta\langle r^2\rangle^{52,48}$) were also used to parametrize the Fayans functional, Fy(Δr,BCS) [25]. Through these additional terms, and the direct input of differential charge radii, the microscopic details of the calcium chain can be reproduced quite well, despite an exaggeration of the odd-even staggering. When moving to unstable nuclei however, Fy(Δr,BCS) fails to fully reproduce the sharp increase on the neutron-rich side [26], and diverges dramatically from these new results reported here on the neutron-deficient side. When this parametrization was developed, it was examined with a focus on well-bound nuclei, and so the Hartree-Fock (HF)+Bardeen-Cooper-Schrieffer (BCS) approach was used [25].

The HF+BCS method is an approximation of the Hartree-Fock-Bogolyubov (HFB) equation which serves well for localized, well-bound states. It reduces the number of coupled equations, which must be solved in the HFB method, however it cannot be used when dealing with exotic nuclei near the drip lines [66, 71]. In the case of these neutron-deficient (proton-rich) Ca isotopes, the effect of loosely-bound protons becomes crucial to reproduce the charge radii. The 20 protons in the Ca nucleus produce a closed $0d_{3/2}$ shell in the single-particle picture, and the next orbital, $0f_{7/2}$, lies above the Fermi energy. When moving to the proton-rich nuclei (^{36,37,38}Ca), this first excited canonical HFB state rises above the

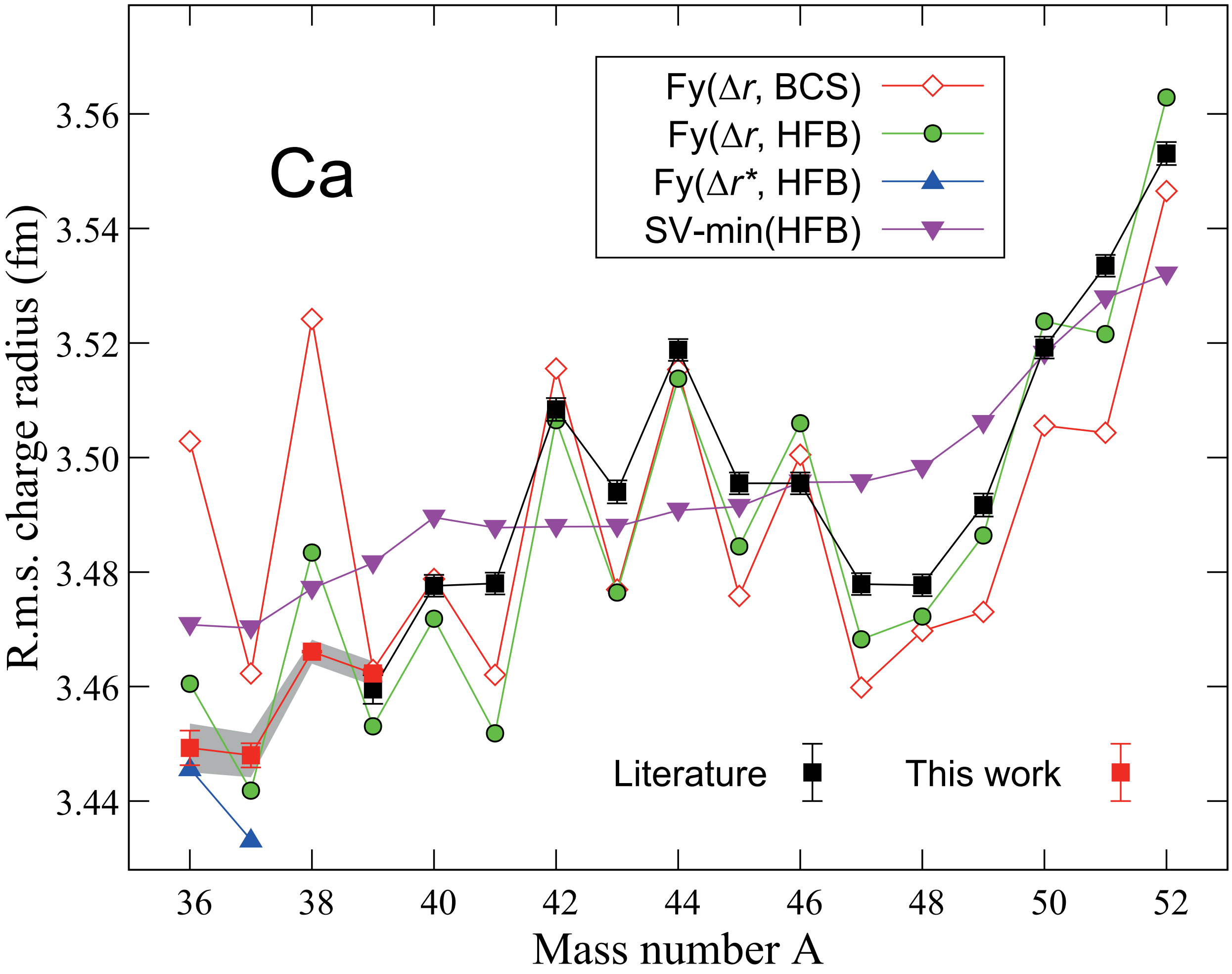

Figure 4.1: The charge radii measured in this work (red squares) and previous experimental values (black squares) are compared to DFT predictions of SV-min (HFB), Fy(Δr,BCS), Fy(Δr,HFB), and Fy(Δr^{*},HFB) models. The values of Fy(Δr^{*},HFB) for $A > 37$ are very close to Fy(Δr,HFB) results; hence, they are not shown. The rms. charge radii were obtained using the known charge radius of ^{40}Ca (ref. [4]), and its error has been incorporated into the systematic uncertainty (the gray band). These values are shown in Table 3.3.

Coulomb barrier, becoming unbound as shown in Figure 4.2(a) [36]. In this case, the pair densities given by the BCS approximation are not localized, and nonzero occupations of these unbound states lead to the appearance of an unphysical gas component, giving dramatically increasing single-proton rms radii as shown in Figure 4.2(b), and the very large radii and staggering of the proton-rich Ca isotopes in Figure 4.1.

To correctly model the behavior in this region, Fy(Δr,HFB) was created using the full HFB approach. In addition, while Fy(Δr,BCS) used neutron and proton odd-even binding energy staggering, $\Delta_E^{(3)}$, the Fy(Δr,HFB) parametrization uses Δ_E^{ee}, which derives from even-even nuclei [25]. This change in parameters is better for open-systems [72], and was confirmed to have very little effect on the Fy(Δr,BCS) model [36].

Fy(Δr,HFB), produces single-proton states which do not suffer from drastic growth as they rise above the Fermi energy [36]. The single-proton radii of ^{36}Ca states are shown in Figure 4.2(b), and the occupations in (c) of the same figure. As shown, this model reduces the size of the unbound states. While Fy(Δr,BCS) shows large radii for these states, the occupations are greatly reduced. Despite this reduction in occupation, the charge radii predicted by Fy(Δr,BCS) still greatly overestimate the neutron-deficient radii measured here. Amazingly, the new model Fy(Δr,HFB) not only improves the agreement on the neutron-deficient side, but also improves the behavior of the charge radii on the neutron-rich side, where recent measurements found the radii to be unexpectedly large [26].

Finally, Fy(Δr^*,HFB) uses the same experimental inputs as Fy(Δr,HFB), but also includes the new $\delta\langle r^2\rangle^{36,40}$ measurement from this work. The charge radii obtained using these new HFB Fayans models are shown in Figure 4.1. Fy(Δr^*,HFB) improves agreement for ^{36,37}Ca, while the rest of the chain is largely identical to Fy(Δr,HFB), so only these two values have been included in Figure 4.1. Odd-even staggering is consistently overestimated

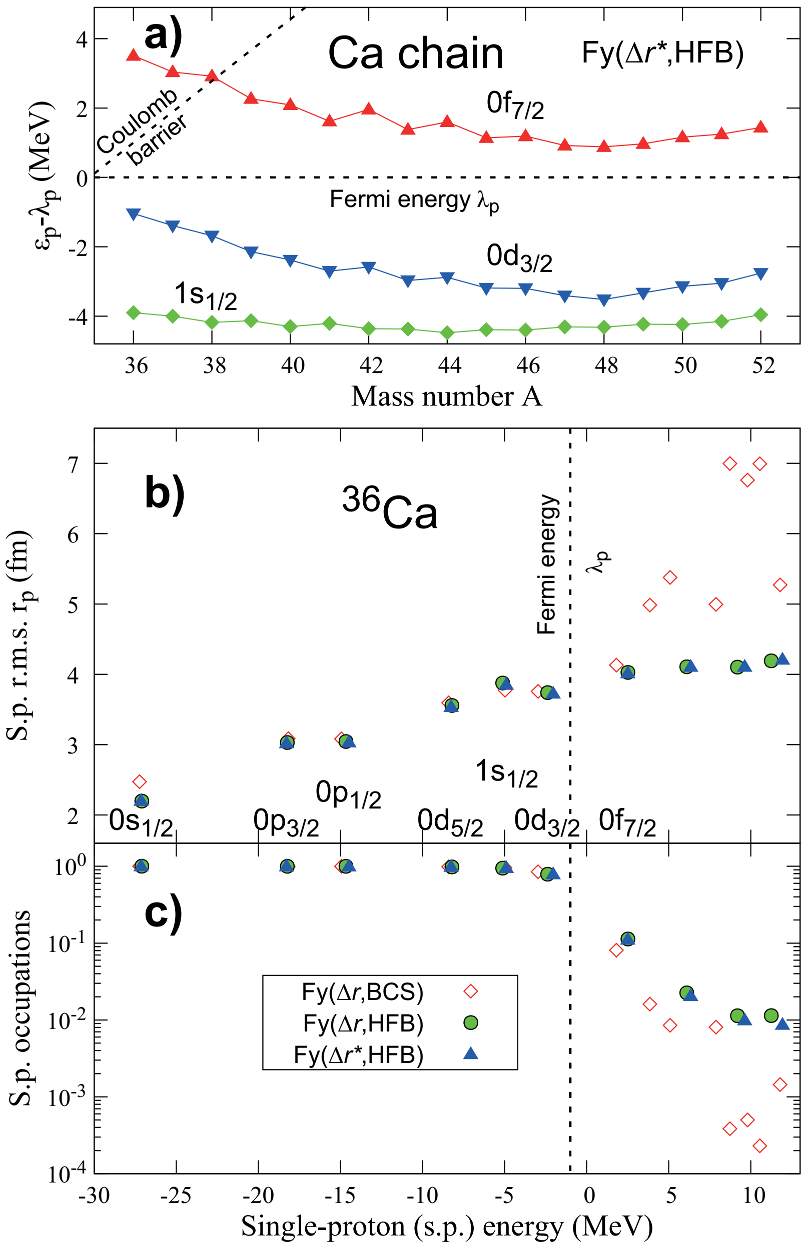

Figure 4.2: Graphs showing the energy levels, radii, and occupations of the single proton states in the Ca chain. The upper graph, a), highlights the weakly-bound nature of the valence protons. As shown by the red triangles, the single proton energy of the $0f_{7/2}$ orbital rises above the Coulomb barrier and becomes unbound in the case of $^{36-38}$Ca. Graphs b) and c) display the single-proton rms radii and occupations, respectively. In the case of the Fy(Δr,BCS) approach, the single-proton radius increases in a non-physical way as the states rise above the Fermi energy and continuum effects come into play (red diamonds). With a realistic pairing interaction, these unbound states do not grow so dramatically in size, as shown by the Fy(Δr,HFB) and Fy(Δr^*,HFB) points (green circles and blue triangles).

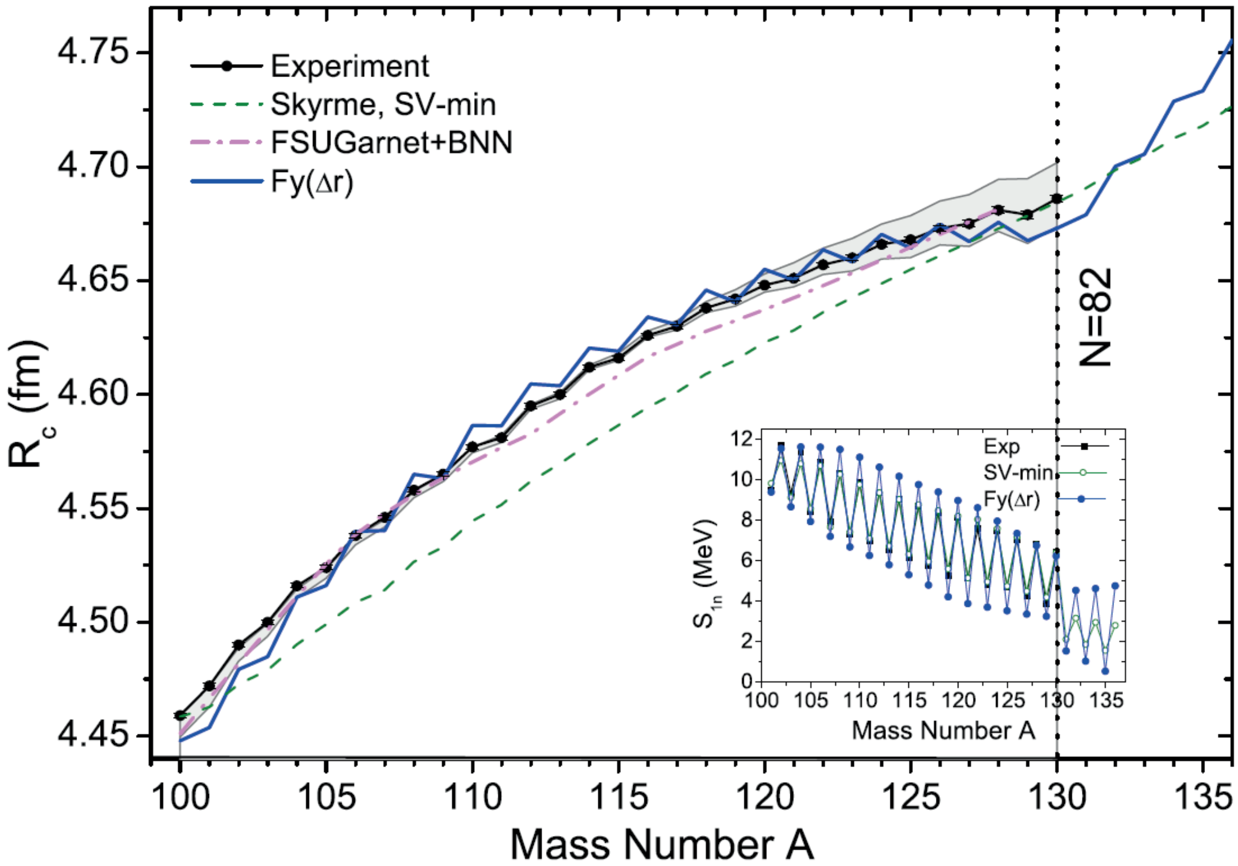

Figure 4.3: Nuclear charge radii of cadmium isotopes. Figure taken from reference [73]. Experimental values and several models are shown. The gray band represents the systematic uncertainty of the experimental values, arising from the uncertainty of the field-shift constant. The inset also shows the corresponding one-neutron separation energies. The agreement of the Fayans functional is quite good, although some overestimation of the odd-even staggering is present here as well.

across the chain, but this is a minor discrepancy when considering the good agreement of the major features. The significant improvement over the Fy(Δr,BCS) predictions on both ends of this isotopic chain, especially given the challenging behavior of the calcium radii, highlights the fact that these density gradient dependent pairing-effects using the full HFB formalism are a critical step towards developing a global model of charge-radii. Conversely, these results also emphasize how important charge radii data are in order to pin down the form of the pairing energy density functional.

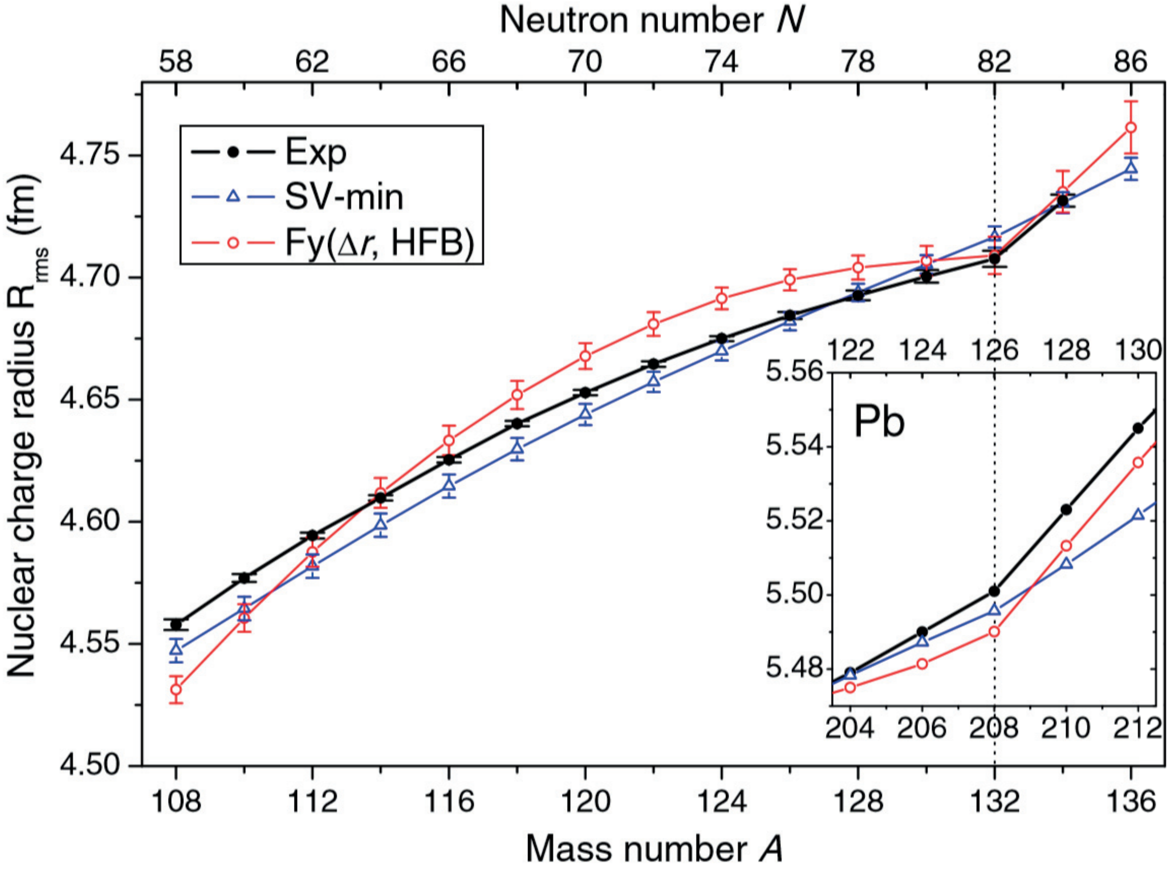

Figure 4.4: Nuclear charge radii of tin isotopes. Figure taken from reference [74]. Experimental values and several models are shown. The inset also shows the behavior of the Fy(Δr,HFB) model in the vicinity of ^{208}Pb. The ability of this Fayans functional to reproduce these kink-structures in heavy isotopes without additional tuning is quite remarkable.

This improvement to the Fayans model is especially useful considering the behavior of this functional in other isotopic chains. The Fy(Δr,BCS) model has been shown to be effective at reproducing the much heavier charge radii, $^{100-130}$Cd ($Z = 48$) [73], and the Fy(Δr,HFB) has been shown to reproduce the kink-structure recently observed around ^{132}Sn [74], as well as ^{208}Pb. Experimental charge radii and model predictions in these regions are shown in Figure 4.3, and Figure 4.4. This broad applicability of the Fayans functional shows great promise for use across the entire chart of the nuclides. The demonstration here of its ability to correctly deal with proton-rich nuclei when pairing effects are accounted for in a proper manner, shows that the Fayans model is flexible enough to apply to a wide range of masses and also can account for behaviors which occur far from stability.

4.2 Empirical extrapolation

Another tool to understand the behavior of this chain of charge radii is to examine the empirical relationships between neighboring charge radii. In a recent study, four primary relationships were identified which allow charge radii to be predicted from known neighbors [75]. These $in - jp(i, j = 1, 2)$ charge radii relations are explained in Figure 4.5.

In general, these relationships allow a robust prediction of charge radii when neighboring nuclides, separated by 1 or 2 protons or neutrons, are known. In reference [75], many charge radii were predicted, and it was noted that radii which deviate significantly from these empirical relationships may suggest interesting local physics, such as sudden variations in shape. These predicted values are overlaid with the experimental calcium chain in Figure 4.6. Across the entire calcium chain, these predictions perform reasonably well. The area with the most significant discrepancy are isotopes lighter than ^{40}Ca, which are under-predicted,

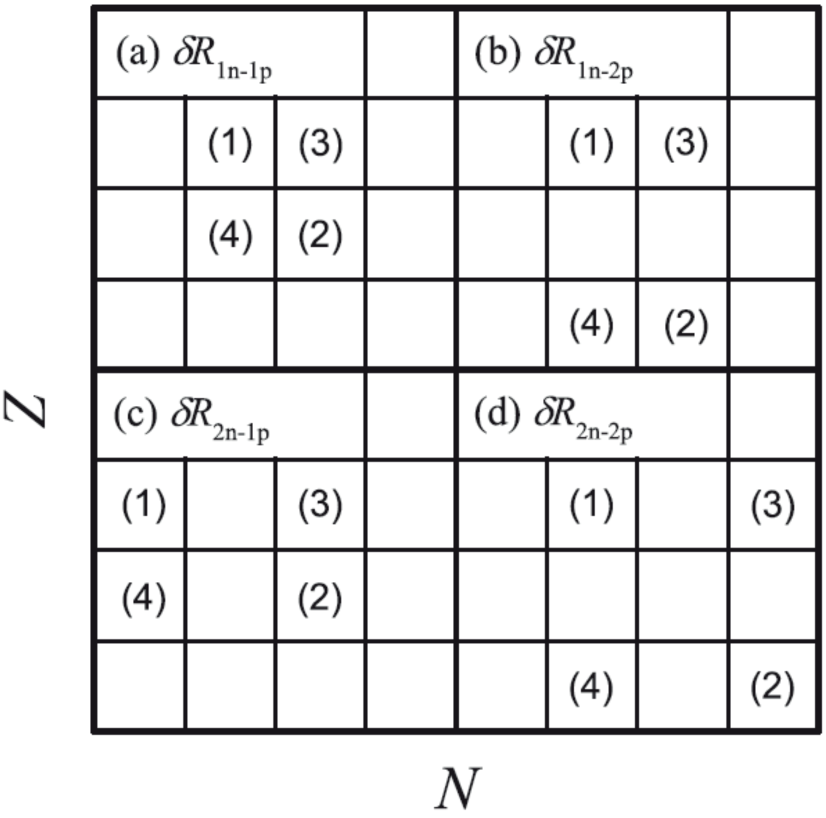
(a) $\delta R_{1n\text{-}1p}$
(1)
(3)
(4)
(2)
(b) $\delta R_{1n\text{-}2p}$
(1)
(3)
(4)
(2)
(c) $\delta R_{2n\text{-}1p}$
(1)
(3)
(4)
(2)
(d) $\delta R_{2n\text{-}2p}$
(1)
(3)
(4)
(2)
Z
N

Figure 4.5: Figure from reference [75]. This figure shows the relative locations of the nuclides used in the four empirical charge radii relationships. In all four cases, $\delta R_{in-jp} = R(1) + R(2) - R(3) - R(4) = 0$, allowing the prediction of a charge radius from the other three. This relationship is most robust for (a), where there is only a step of 1 proton or neutron between the four nuclides being compared, but holds reasonably well for the other three relationships as well.

suggesting that these nuclei are growing larger than neighboring nuclei would suggest, due to the weakly-bound protons when moving further from stability. The strong agreement of these empirical relationships across the entire calcium chain highlights the fact that there is no unique local effect occurring in the calcium isotopes, rather they present a complicated pattern of charge radii which is also suggested by neighboring nuclei. This strengthens the argument that these Ca isotopes can be used as a benchmark for charge radii models, and suggests that a model which performs well across this region can be applied to other elements as well.

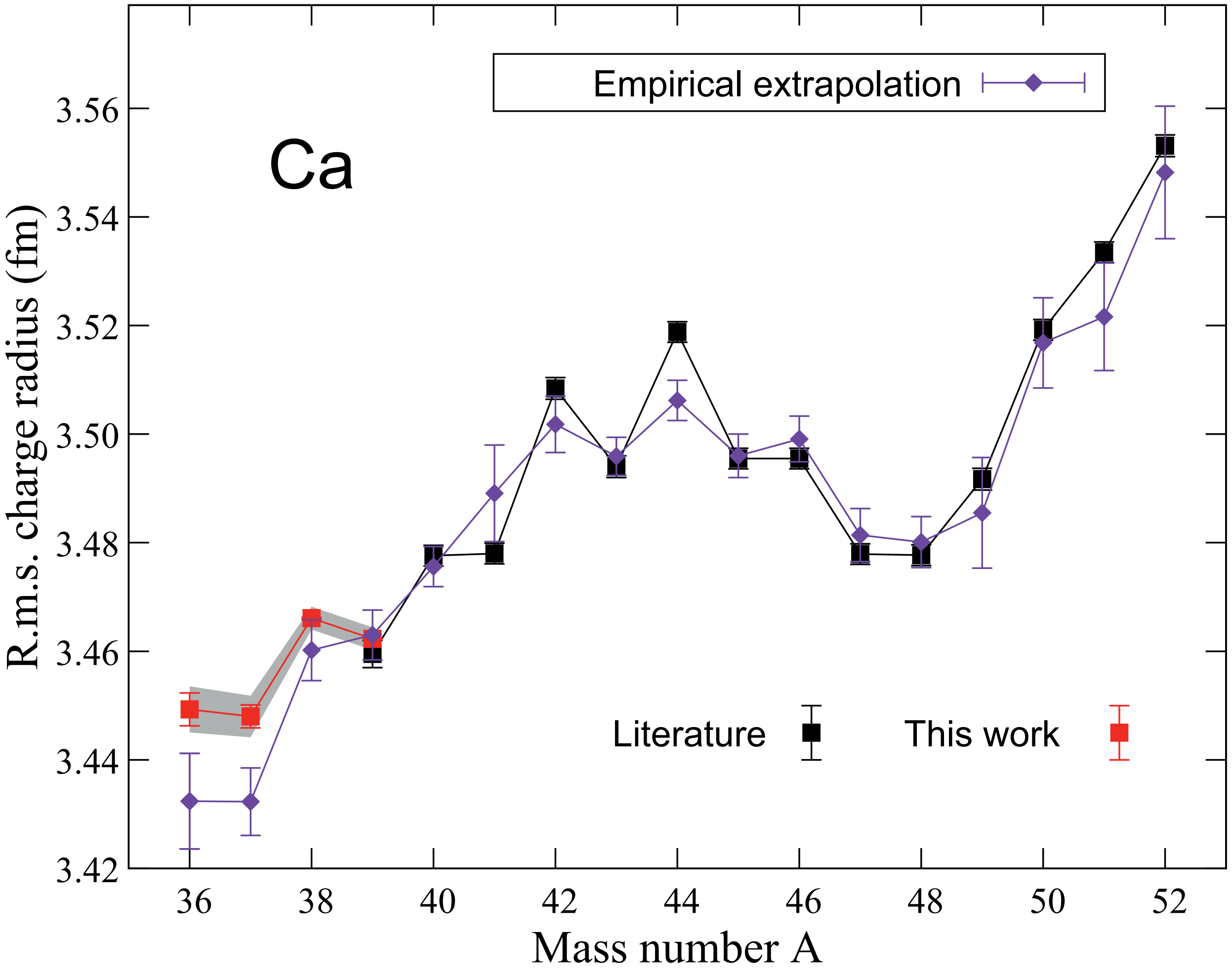

Figure 4.6: Empirical predictions of charge radii shown here in purple diamonds are taken from reference [75]. These predictions use some combinations of the four relations shown in Figure 4.5. Experimental charge radii are shown using the red and black squares. Large deviations from the empirical predictions can suggest sudden variations in shape or density of the nucleus. It is interesting to note that while previous theories dramatically over predicted the size of the proton-rich nuclei in this chain, these empirical predictions are reasonably accurate, and in fact under predict nuclei below $A = 40$, which is to be expected considering the effect of the weakly-bound protons in these isotopes. This highlights the fact that there is no sudden change of behavior of the charge radii in this region, and strengthens the belief that a model which performs well in this chain may be applicable across the nuclear chart.

Chapter 5

Conclusion

The hyperfine spectra of calcium isotopes ^{36,37,38,39}Ca were measured. These measurements have advanced the bunched-beam CLS technique at BECOLA; the first use of the new PDS, offline production of calcium ions, and calibration using multiple stable isotopes were a success. The measurement of ^{36}Ca ($T_{1/2} = 102\,\mathrm{ms}$) using 50 ions/s and 33 h of data was the most sensitive measurement performed at BECOLA to date. Fortunately, it was possible to obtain a large fraction of calcium ions from the gas cell in their singly ionized state, as opposed to doubly ionized. This allowed the measurement to be performed on the Ca II $4s\ ^2S_{1/2} \leftrightarrow 4p\ ^2P_{3/2}$ (393.3663 nm) transition, using frequency doubled light from the Ti:Sapphire laser. Due to the fact that charge exchange was not required to obtain singly-charged ions, the background reduction of the new PDS was effective, and provided an increased SNR over the previous system. The additional statistics from the fact that two identical systems were installed also helped to achieve this new level of sensitivity.

The hyperfine spectra had linewidths of approximately 75 MHz, and the isotope shifts were obtained using reference measurements of ^{40}Ca. These isotope shifts were extracted with less than 6 MHz of statistical uncertainty. Uncertainty in the high voltage of the cooler/buncher was minimized by using two stable isotopes, ^{40,44}Ca, and their known IS for calibration, leading to less than 5 MHz of systematic uncertainty in the IS for each isotope. From the isotope shifts, the differential mean-square charge radius relative to ^{40}Ca was obtained for each isotope. Thanks to the careful studies which the stable calcium isotopes have received, the atomic factors required to deduce these radii are precisely known, allowing the charge radii to be extracted with a total uncertainty of less than 0.005 fm for ^{36}Ca, and 0.002 fm for ^{39}Ca (see Table 3.3) [36]. This is a first time result for the charge radii of ^{36,37,38}Ca, and ^{39}Ca is in agreement with previous experimental data while increasing precision by a factor of three.

These measurements highlight the importance of utilizing the bunched-beam CLS technique in facilities with differing methods of isotope production. The success of this technique at ISOL facilities is be complemented by these experiments at the NSCL, as the in-flight production of rare isotopes provides access to short-lived neutron-deficient isotopes which are more difficult to produce at ISOL facilities [35]. In conjunction with measurements of neutron-rich calcium isotopes from such a facility [26], a full chain of the calcium charge radii from neutron-deficient to neutron-rich has now been measured. Such a long chain, spanning across the doubly-magic nuclei ^{40,48}Ca and climbing out of the valley of stability on both sides has provided an excellent opportunity to challenge nuclear theories which predict charge radii. Indeed, even the most successful DFT model to date (Fy(Δr,BCS)) showed promise throughout the stable isotopes but did not correctly capture the behavior of the unstable isotopes [36]. The sharp increase beyond $A = 48$ was under-predicted, and the isotopes below $A = 40$ were severely overpredicted, despite the fact that empirical relationship can predict these radii well [75]. This issue highlighted the fact that the BCS pairing approximation breaks down when applied to loosely bound nucleons [66, 71]. Due to the fact that the first excited proton shell, $0f_{7/2}$, rises above the coulomb barrier and into the continuum as neutrons are removed, the effects of proton pairing in these unbound orbitals becomes significant. By incorporating the more physically correct HFB pairing approximation, Fy(Δr,HFB) performs better across the entire chain, accurately modeling the trend of these new experimental measurements on the neutron-deficient side, and even improving the agreement on the neutron-rich side [36]. Such a dramatic improvement and the ability to model this complicated chain of isotopes highlights the flexibility of the Fayans model. This model has also shown good results when applied to the heavier Cd, Sn, and Pb chains [73, 74] and is a fundamental step towards developing a global model of nuclear charge radii.

Although obtaining new measurements of nuclear observables can be useful in its own right, the measurements here have accomplished even more. These measurements have pushed the sensitivity of the bunched-beam collinear laser spectroscopy even further, and the successful results have provided critical experimental values which have increased our understanding of nuclear structure. The extension of the chain of calcium charge radii to the isotopes ^{36,37,38}Ca has challenged the most advanced theories, and by reformulating the Fayans model with a careful consideration of proton pairing in weakly-bound states, its flexibility and applicability as a global model of charge radii have taken a crucial step forward. In the future, as the Facility for Rare Isotope Beams (FRIB) comes online at MSU, access to unstable isotopes at BECOLA will be greatly increased [76]. By reaching to even more exotic Ca isotopes, measuring neighboring isotopic chains such as Sc and mirror-nuclei, BECOLA will to continue to further test and refine our understanding of nuclear structure.

APPENDICES

APPENDIX A

Hardware

A.1 Photon detection system

A.1.1 Optical simulations

Prior to the manufacturing of the new PDS, simulations were performed using FRED, a raytracing simulation for optical systems. In these simulations, an arbitrary amount of signal and background were generated, and the fraction of each arriving at the PMT were evaluated. Signal was approximated as rays emanating in random directions from a cylindrical volume, where the laser beam and ion beam overlap. Background photons were simulated using rays originating at random points within a circle placed just outside the PDS, emanating in random directions within the hemisphere towards the PDS.

This simulation was performed using both a model of the old PDS, as well as the new design. While the simulated signal can easily be assumed to be identical between each system, there is some difficulty in deciding how to ideally compare the simulation of background photons between the two systems, as the old and new systems have different diameter openings at differing distance from the center of the PDS. The background source was placed at the edge of the elliptical region for the new system, however when this geometry is directly copied to the old system, there is a gap between the source and the short tube leading to the ellipsoidal region. To account for this difference, simulations of the old system were also performed with the background source moved toward the center of the PDS, to sit flush with the tube. These three simulations, one with the new system, and two variations using the old system were used to give an estimated range for the comparison of the old and new systems.

For the existing PDS, the rays were collected at the plane of the PMT, and the results are shown in Figure A.2. In the new system, the rays were analyzed at the focal plane of the elliptical section to determine the appropriate position of the aperture to select the focused signal, and the rays were then also collected at the PMT following the CPC, as shown in Figure A.3. The fractional acceptance of signal and background were determined for each system in the simulations, and are listed in Table A.1.

The decision to use a 20° CPC was made by examining the angular distribution of photons at the focal plane of the new system. As shown in Figure A.4, the background and signal angles are fairly well separated. The same cannot be said for the old system, so a CPC added to the existing setup would not be helpful, as shown in Figure A.5.

Figure A.6 shows the simulated acceptance of the signal from various points within the detection region. While the old system collects a large amount of signal at the center, the new system has a more consistent acceptance throughout the detection region. Ultimately, this variation in the position along the beamline where signal is collected is not important, the primary interest is the total signal and background acceptance of each system.

In order to compare the SNR of each system, the signal and background counts of offline Ca runs taken with the existing system were used. From the simulations, the ratio between the signal acceptance of the new and old systems was used to scale the signal counts, while the ratio of the background was used to scale the background counts. In this way, the signal and background from actual measurements using the old system can be compared to the

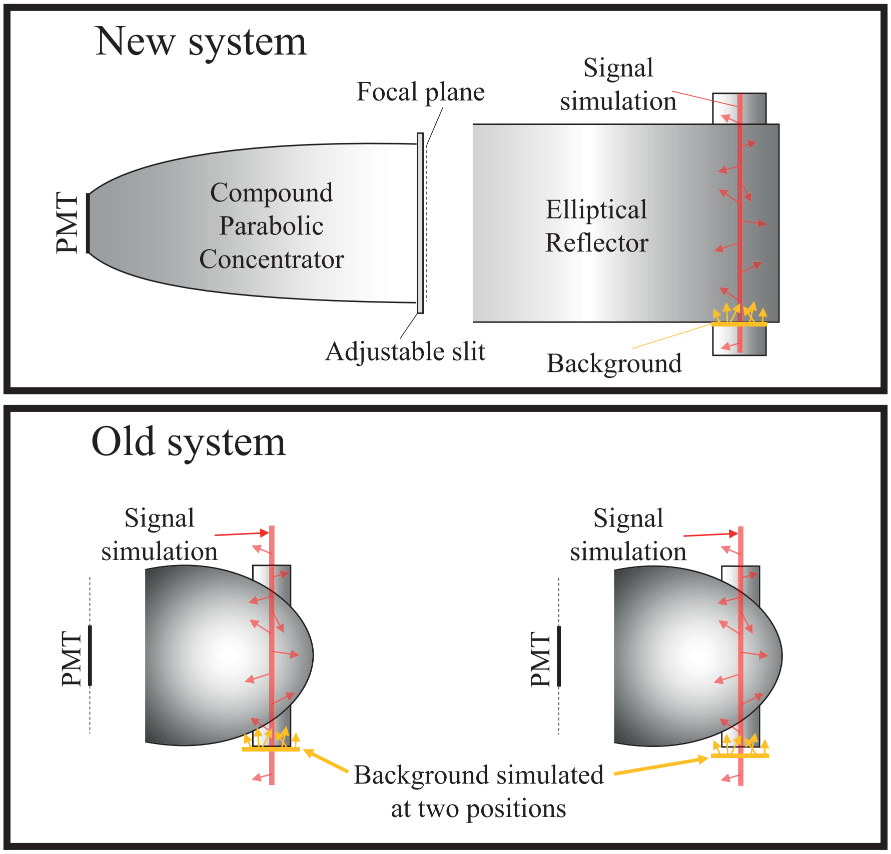
New system
Focal plane
Signal simulation
PMT
Compound Parabolic Concentrator
Elliptical Reflector
Adjustable slit
Background
Old system
Signal simulation
PMT
Signal simulation
PMT
Background simulated at two positions

Figure A.1: Schematic showing the three simulation setups. Raytracing simulations were performed in FRED using perfectly reflective surfaces. The new system was simulated with a cylindrical volume emitting rays in random directions, while the background was simulated as rays emitted in random directions from within the area of a circle placed at the entrance to the elliptical region. The old system was simulated twice, once with the sources positioned identically to the new system, shown on the right, and again with the background source moved closer to be flush with the system, as shown on the left. These two simulations of the old system were used to evaluate the stability of the simulations and obtain a range of expected values.

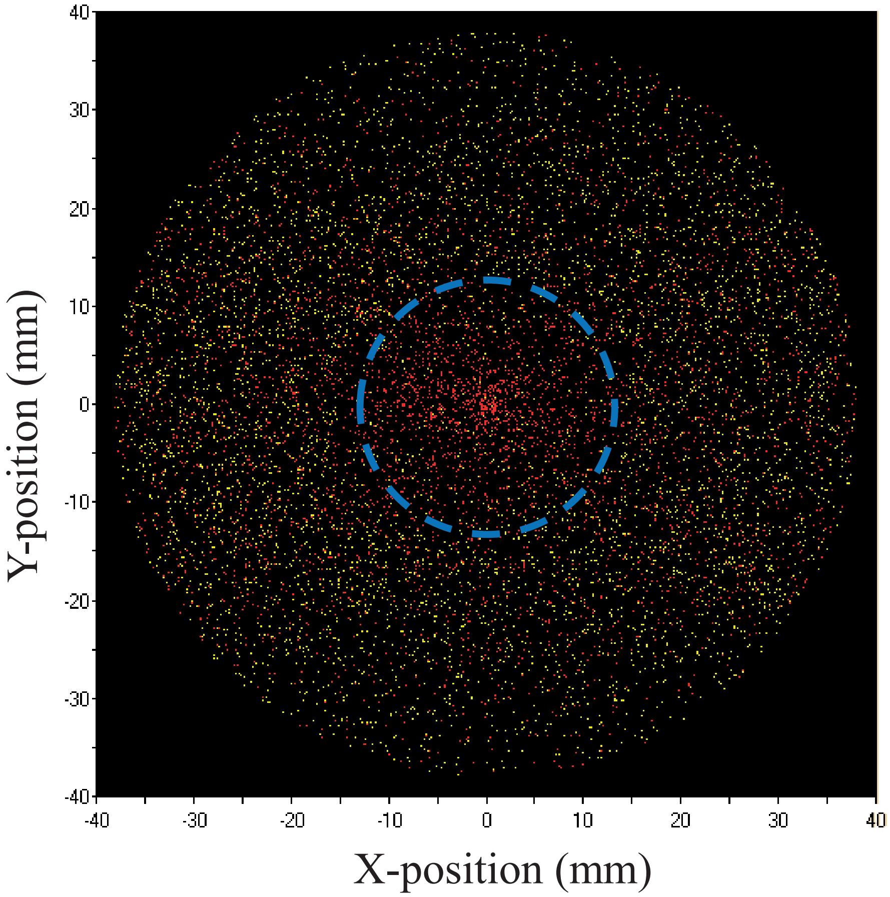

Figure A.2: Simulation showing the geometric distribution of photons arriving at the focal plane using the existing PDS. The blue dashed circle indicates the geometric acceptance of the PMT, collecting the majority of the signal (red points), and excluding a portion of the background (yellow points). In this simulation, 44.8 % of the signal photons reach the focal plane, while 25–40 % of the background photons simulated arrive at the focal plane. In the area covered by the PMT, 13.4 % of the signal, and 1.5–2.6 % of the background were collected. The range of values for the background are due to a variation in the position of the simulated background source as described in Section A.1.1.

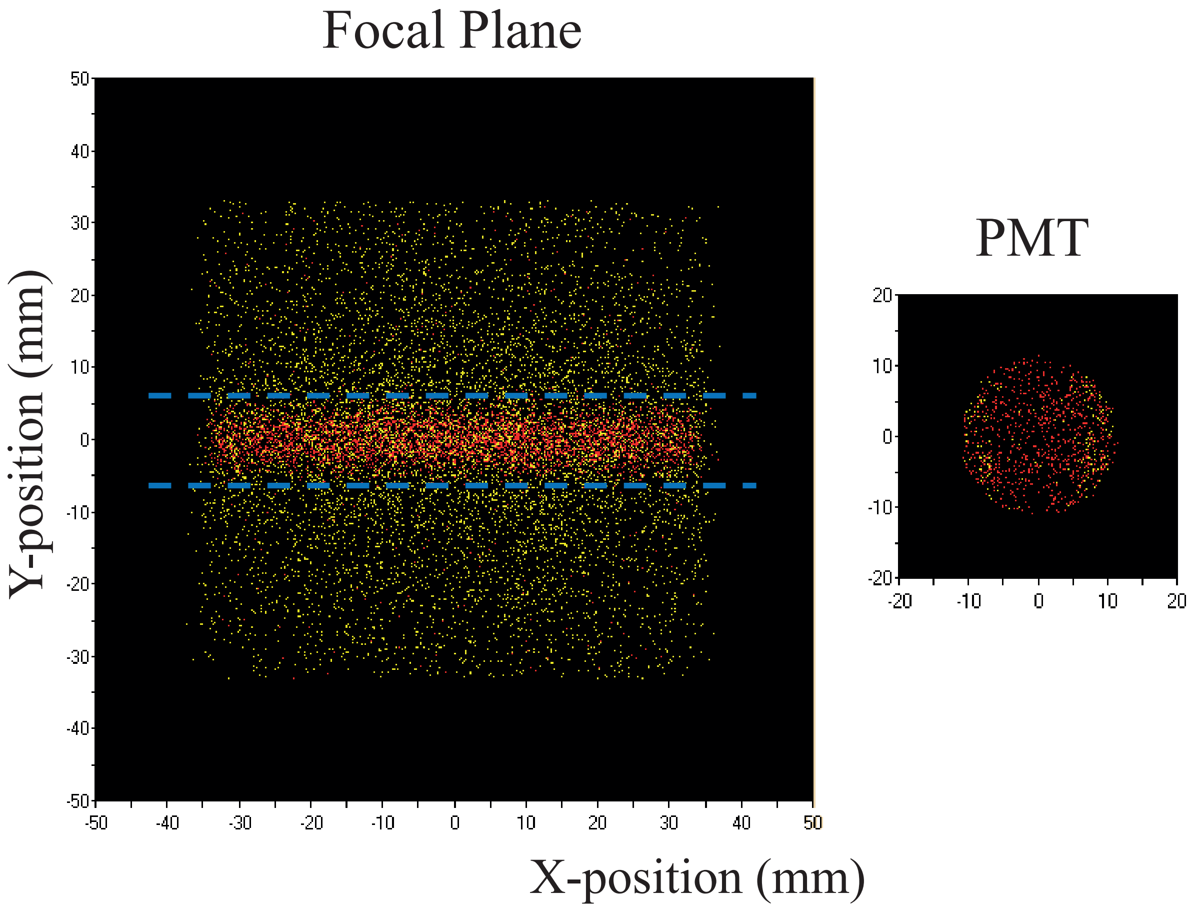

Figure A.3: Simulation showing the geometric distribution of photons arriving at the focal plane (left) and the PMT (right) with the new PDS. The blue dashed line indicates the geometric cutoff of the aperture at the focal plane, collecting the majority of the signal (red points), and excluding a portion of the background (yellow points). In this simulation, 42.9 % of the signal photons pass through the aperture of the focal plane, compared to only 15.3 % of the background photons. Following the CPC, the PMT accepts 8.3 % of the signal, and only 0.21 % of the background photons.

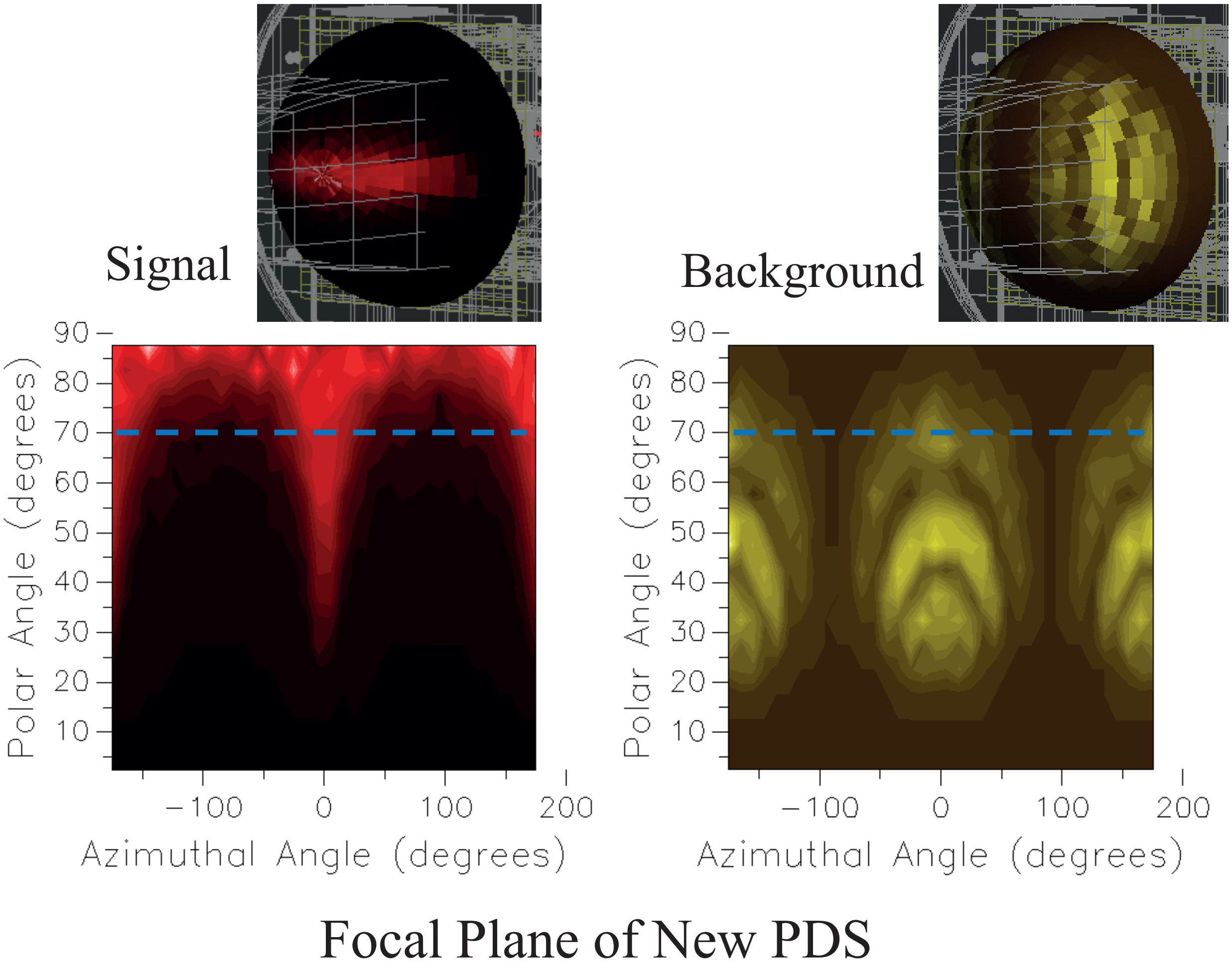

Figure A.4: Simulation results describing the angular distribution of photons arriving at the focal plane of the new PDS. Signal is shown in red, and background in yellow. The polar angle of 0° corresponds to the perimeter of the hemisphere, while an azimuthal angle of 0° or ±180° corresponds to the beam axis. The angular distribution is also shown projected onto a hemisphere above each graph, the center of the hemisphere faces the PMT. The blue dashed line indicates the angular cutoff chosen for the CPC. Photons arriving with a polar angle less than 70° are rejected excluding a large part of the background

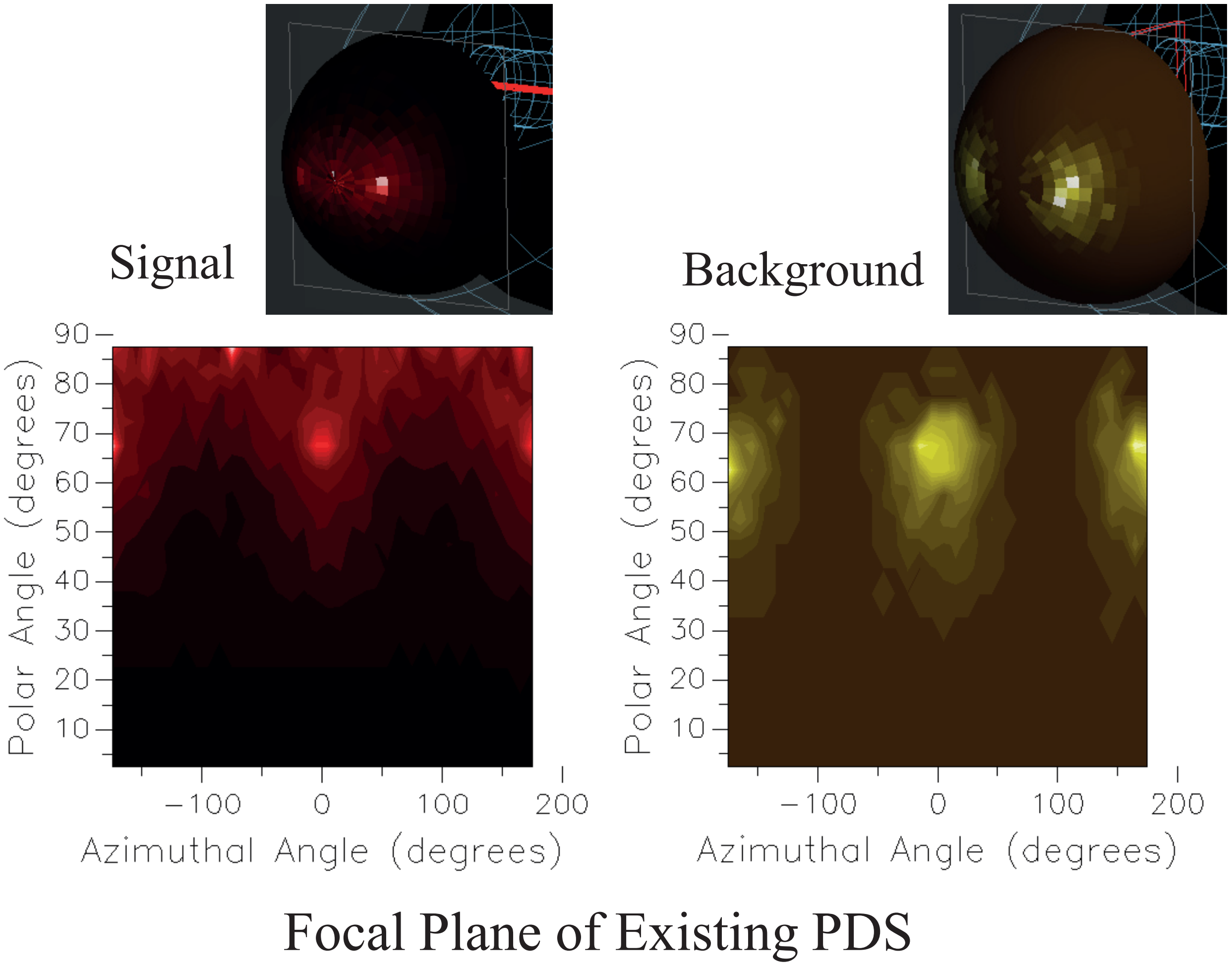

Figure A.5: Simulation results describing the angular distribution of photons arriving at the focal plane of the old PDS. Signal is shown in red, and background in yellow. The polar angle of 0° corresponds to the perimeter of the hemisphere, while an azimuthal angle of 0° or ±180° corresponds to the beam axis. The angular distribution is also shown projected onto a hemisphere above each graph, the center of the hemisphere faces the PMT. As shown, the primary intensity of both the signal and background lie at the same polar angle, preventing any improvement from adding a CPC to the existing system.

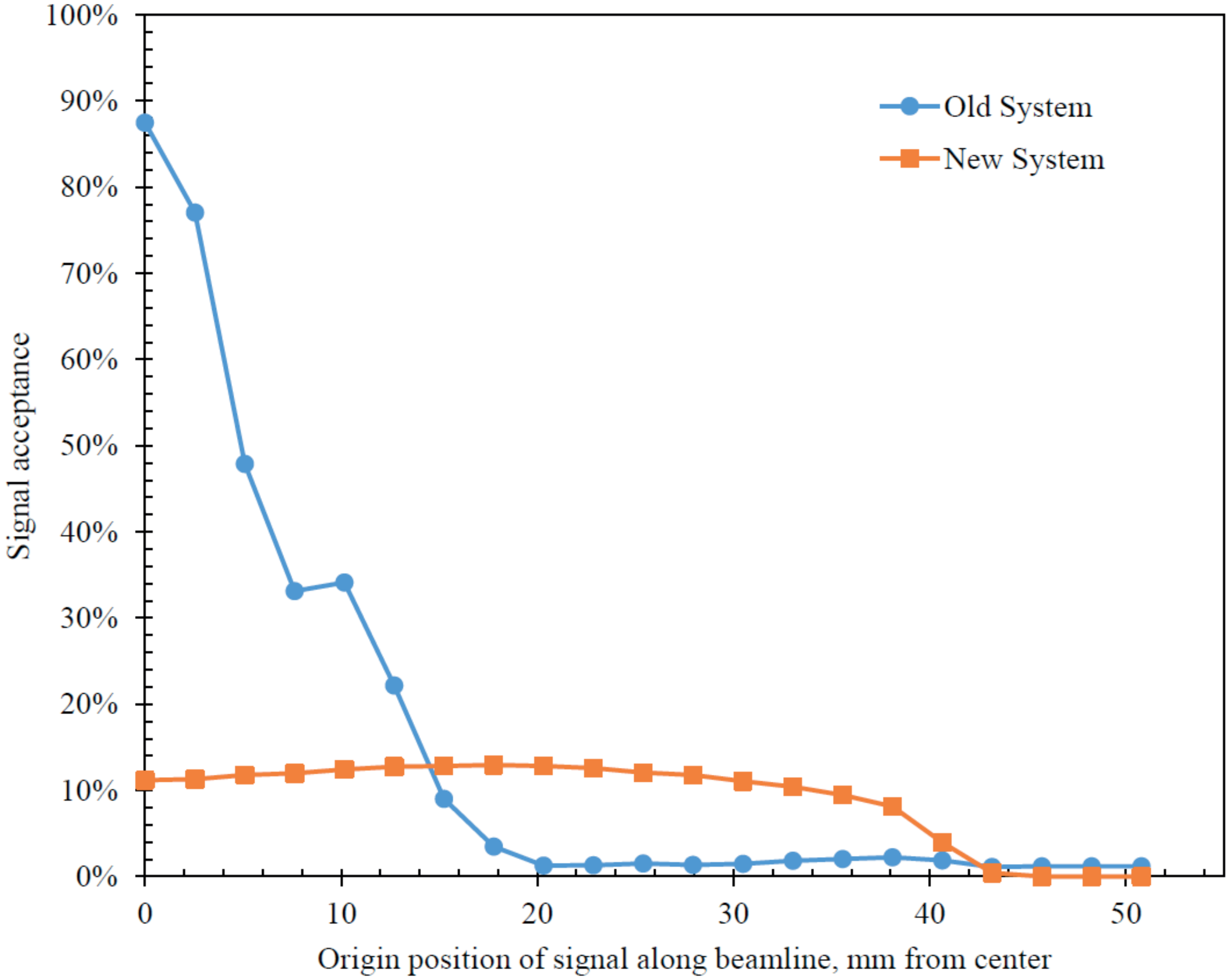

Figure A.6: This simulation highlights the difference in signal collection of the two systems. While the old system collects a large fraction of the signal at the center of the detection region (the focus of the ellipsoid), the new system collects signal more consistently across the entire region. The total acceptance of the new system (area under this curve) is still less than the old system, however, the increase in noise rejection allows it to outperform the old system for the Ca II measurement.

simulated performance of the new system for the measurement of Ca ions.

While this simple ratio of signal and background simulation takes into account background from stray laser light, more care is required when the charge-exchange cell is used in an experiment. To examine the effects in these conditions, data taken at BECOLA using ^{53}Fe were used. The signal and background in this case were divided into three categories: signal from the laser-atom interaction, background from atomic decays subsequent to the charge exchange, and background from stray laser light. Using bunched beam spectroscopy, the rates from each of these categories can be measured experimentally. When the atom bunch is not present, the recorded rates indicate the background due purely to the stray laser light. At the window of time where the bunch is present, yet the scanning voltage is off-resonance, the "glow" from the charge exchange process can be counted above the laser background. Finally, where the resonant peak of the spectrum is measured, the rates of all three combine together.

This allows the extraction of each category of photon counts separately and, each can then be treated them according to the appropriate simulation method. The laser-atom interaction and the decays from the charge exchange will be accepted by the system according to the signal in the simulation, as they are produced directly by the beam passing through the system, while the stray light is modeled using the background in the simulation.

For the Ca experiment, because a transition in Ca II is being used, the charge exchange cell is not necessary, and thus there is no background related to the decay from higher atomic states produced in the charge exchange process.

The signal and background levels from data taken for ^{56}Fe using charge exchange, and ^{40}Ca with no charge exchange were used in conjunction with the simulations in order to estimate the SNR which could be achieved with the new system. When charge exchange is being performed, comparison to the simulation becomes less direct, as a non-trivial amount of background is produced by the ions due to excited atomic states decaying from the charge exchange process. This background is being introduced directly from the beam path, and so is scaled based on the simulated acceptance of the signal, while the background from the laser must be scaled according to the simulated background. Because this beam-related background cannot be reduced using this design, the relative reduction in signal collection compared to the existing system leads to a reduction in SNR for a measurement involving charge-exchange. When examining stable isotopes of Ca which were measured offline at BECOLA without charge exchange, the new system's background rejection is much more effective, and in the simulations it performed better than the old system despite the slight reduction in signal. These results are shown in Table A.1.

Based on these simulations, the new design including a 20° CPC was constructed and installed at BECOLA, inserted into the beamline just following the existing detection region. The new system includes two separate detection regions, each with their own elliptical reflector, CPC, and PMT, further increasing the measurement capability compared to the previous system.

A.1.2 Installation

In order to install the system into the beamline, a custom beam pipe cross was fabricated to provide 8 in CF flanges on each end, while four flanges on the sides allow for the high voltage passthrough to control the detection region, and the windows which allow the photons to be collected outside of the vacuum. A schematic of this section of beam pipe is shown in Figure A.7. The two new detection regions use identical designs, with one oriented upward, and the other downward from the beamline.

Table A.1: The design of the new PDS was compared to the existing system using simulations within FRED, a ray-tracing tool. Signal photons were simulated using rays emitted in all directions from random points within the volume of a cylinder, approximating the overlapping laser and ion beam. Background photons were approximated by rays originating from random points within a circle, and emanating in a random direction in the hemisphere facing the PDS. For the old system, this background source was simulated in two different positions (see Section A.1.1) leading to the ranges of background acceptance and SNR. Both systems were simulated with perfect reflectance. The fraction of signal and background reaching the detector were compared to several actual measurements using reference ions and the existing system, in order to determine the appropriate ratio of incoming signal and background photons. The SNR in the table are extrapolated from the simulations and these reference measurements, assigning the measurement from the existing system an SNR of 1. Due to the fact that the ^{56}Fe measurement requires the charge-exchange cell, there is an additional background source coming from the ion beam itself, which is collected in the same way as the signal. Because of this, the strategy employed by the new system, to minimize noise even at the cost of some signal, is not as effective, due to the fact that the noise from the charge-exchange process cannot be reduced this way.

System	Signal Acceptance	Background Acceptance	SNR for ^{40}Ca	SNR for ^{56}Fe
Existing system	13.36 %	1.45–2.65 %	1	1
New system	8.42 %	0.24 %	1.5-2.0	0.94-0.97

Installation of the system required special care due to the tight space of the assembly within the beam pipe. A "dirty" assembly was completed outside of the beamline first, in order to evaluate which components could be installed from the side flanges, and which needed to be put in the beam pipe cross before it was inserted into the BECOLA beamline. Following this, the components were disassembled completely and wiped down with methanol, in order to clean them for vacuum. During the reassembly, thin reflective sheets were installed on the optical surfaces, allowing a highly reflective surface without the lengthy manufacturing time of hand-polishing techniques. The reflectivity of these sheets is shown in Figure A.8.

The main support of the PDS uses four rods that run the length of the beam cross. The frame supporting these rods and insulating them from the beam pipe is shown in Figure A.9.

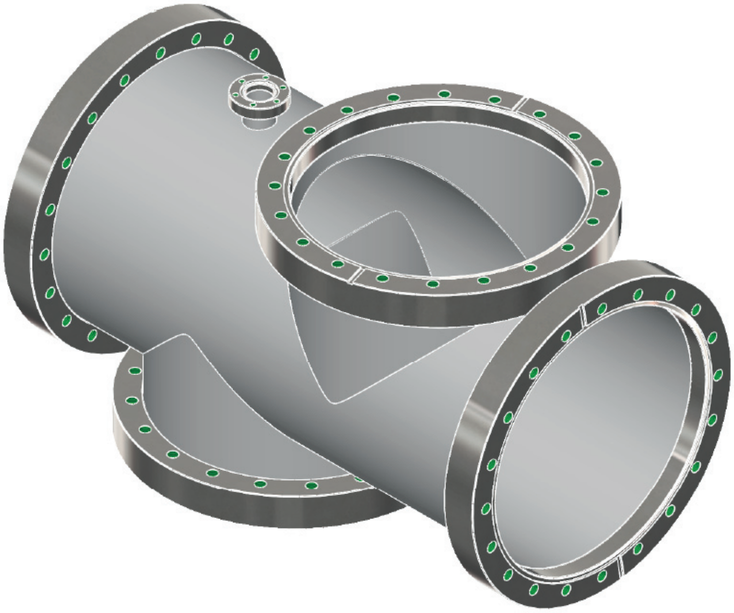

Figure A.7: A schematic of the beampipe used to enclose the two new detection regions. The 8 in flanges on the top and bottom, which are offset from one another, are the location of the two new detection regions. A small flange opposite each allows a high voltage feedthrough in order to apply the scanning potential to the detection region, as shown in Figure A.12.

This frame assembly was installed into the beam cross, and the beam cross was then inserted into the BECOLA beamline. Alignment was then performed using a telescope at the end of the beamline to ensure that the front and back of this new PDS were collinear with the old PDS and the apertures within the BECOLA beamline. Adjustments were made by reaching through the large side flanges of the cross, and rotating the double-threaded brass screws. These screws have one end threaded left-handed, and the other end right-handed. Rotating these screws then allows the 3D printed insulating feet to be shifted outward or inward, allowing the four support rods to be aligned properly with the beam axis and electrically isolated from the beam pipe.

With the four support rods installed and aligned, the elliptical regions were then installed through the side flanges in the beam pipe. Each elliptical region was assembled as shown in Figure A.10 and then attached to two of the support rods as shown in Figure A.11. A short

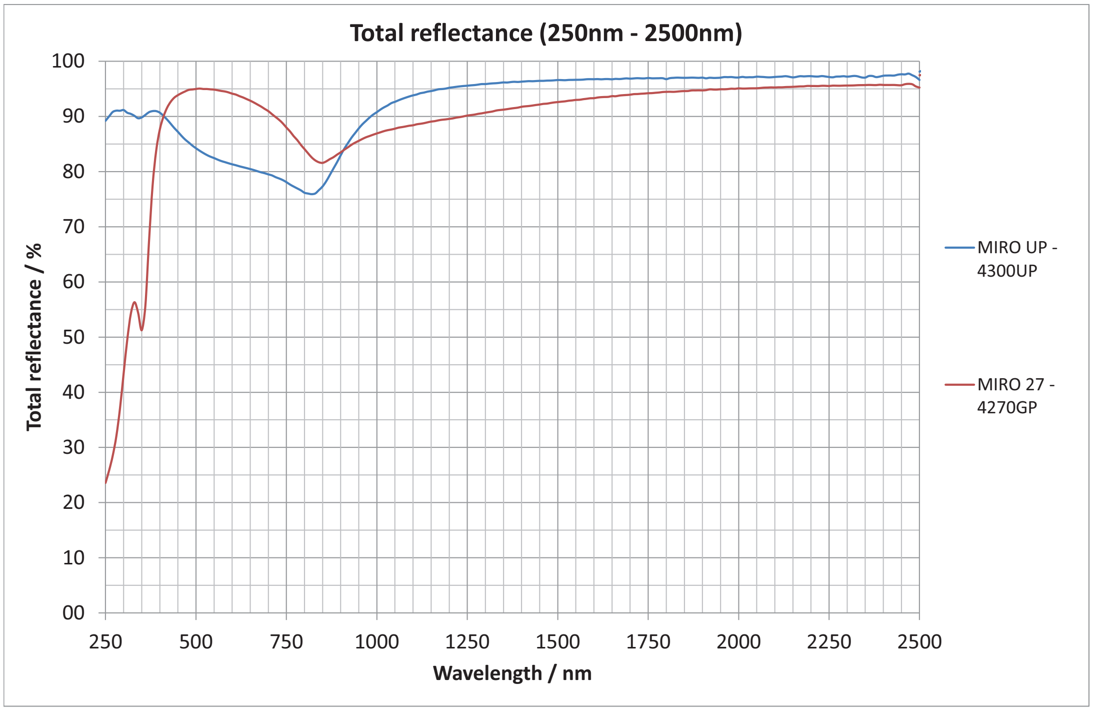

Figure A.8: Reflection data for the aluminum sheeting used for the reflective surfaces of the new PDS. The MIRO 4300UP was used, in order to allow for good reflectivity throughout the UV range (250–450 nm).

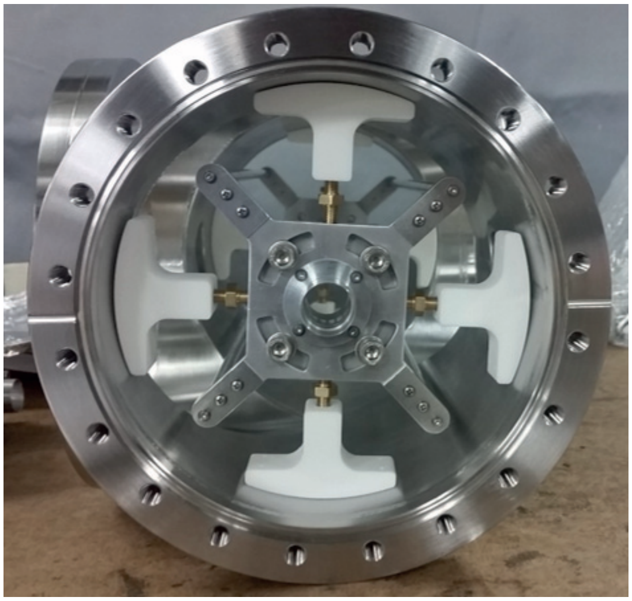

Figure A.9: Looking from the end of the beam cross, the internal supports of the PDS are shown. Four white insulating feet support it within the beam pipe, and the four main support rods are pointing away from the viewer, from the ends of the aluminum × in the center of the beam pipe. The small tube at the center of the × is where the laser and ion beams travel. Alignment of this main frame was accomplished by rotating the double-threaded brass connectors next to the insulators.

length of interlocking pipe was also attached to the sides of each elliptical region, so that there are no gaps in the potential along the beam axis. A high voltage feedthrough was then installed in order to apply the scanning potential to the regions, as shown in Figure A.12.

Next, the windows were attached to the side flanges, and the beamline was pumped down to vacuum once again. The CPCs were assembled as shown in Figure A.13 and attached to the front of each side window, along with two plates for the adjustable aperture. The complete exterior assembly including the aperture, CPC, and PMT mounting hardware is shown in Figure A.14.

Finally, each exterior assembly was enclosed with a light-proof cloth, to prevent light leakage reaching the PMTs. Brass threaded rods which allow for adjustment of the apertures protrude far enough that they can be adjusted without removing the light-proofing wrap.

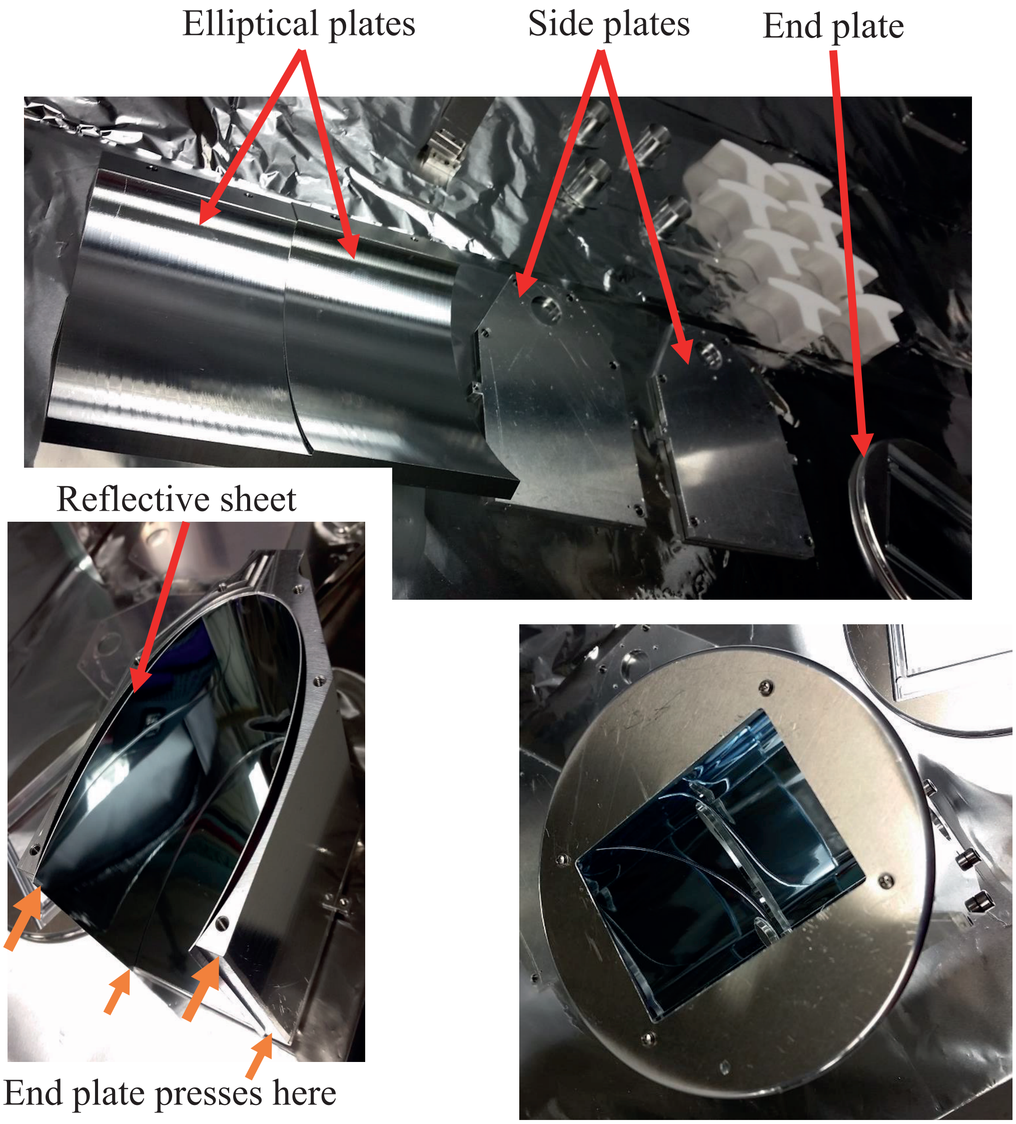
Elliptical plates
Side plates
End plate
Reflective sheet
End plate presses here

Figure A.10: Photographs showing the assembly of an elliptical reflector. On the top, the parts are shown prior to assembly. The left image shows the assembly minus one side plate, and the end plate. When the end plate is attached, it pushes the reflective sheet in flush with the end of the elliptical plates, causing it to bow further outward and lay flat against the elliptical plates. The right photo shows the final assembly, looking in through the window of the end plate. Not shown here is the metal mesh which covers this window in order to ensure that the entire detection region is enclosed by the desired potential when scanning.

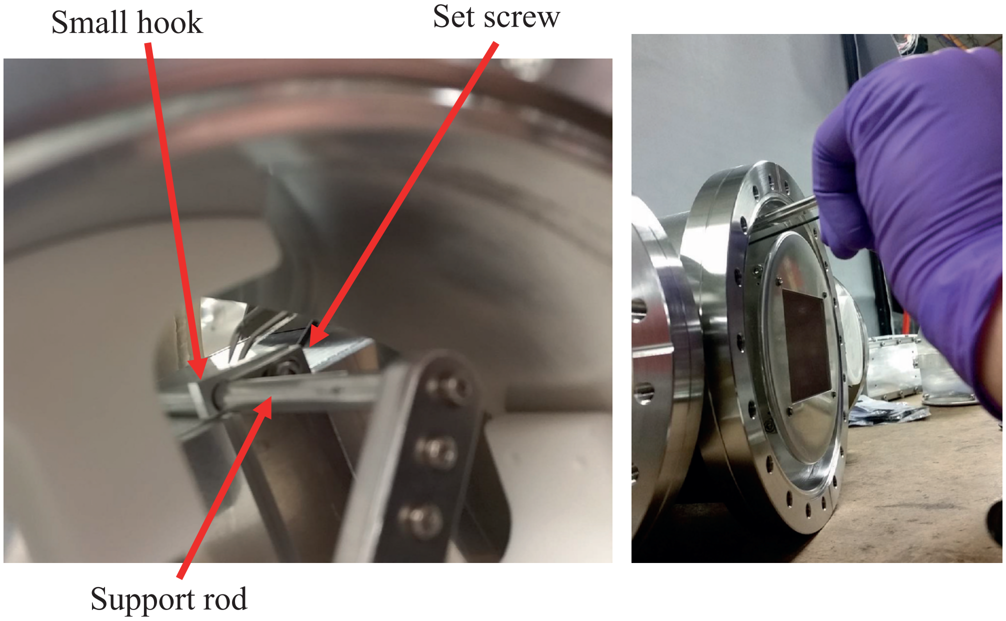

Figure A.11: Photographs showing how the elliptical reflectors are attached to the support rods. On the left the interior of the beam pipe is shown. A small “J” shaped hook holds the elliptical reflector assembly up against the support rods. It is locked in place with a set screw on the side facing out the side flange, and so it can be accessed from outside with careful use of tweezers and a long hex wrench, as shown in the photo on the right.

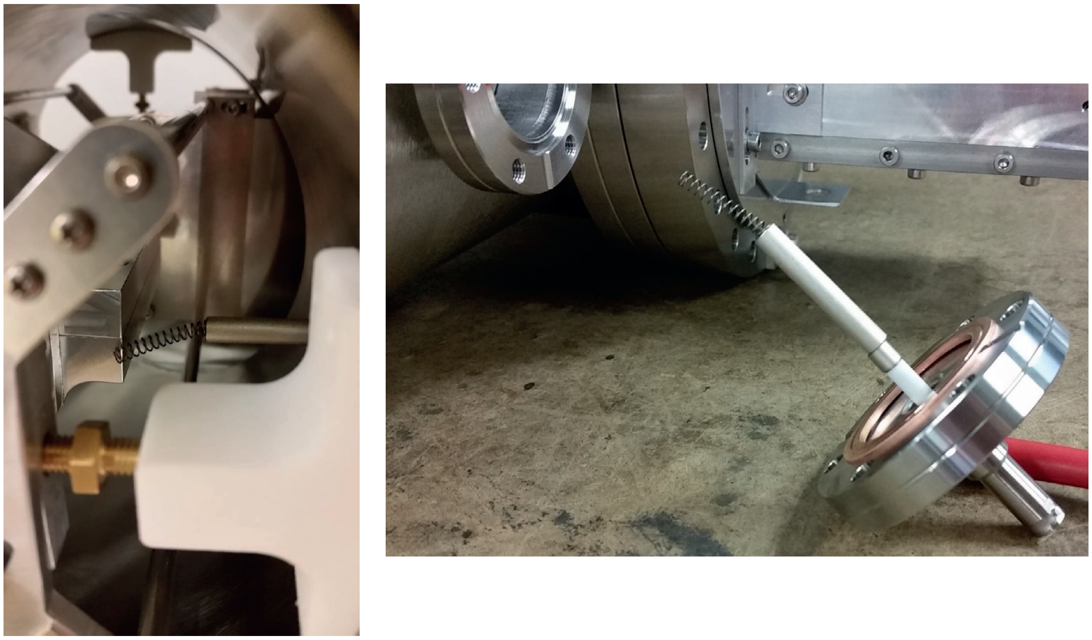

Figure A.12: Photographs showing the installation of the high voltage feedthrough used for the scanning potential. A small spring allows contact with the back of one of the elliptical reflectors. The left photo shows the high voltage conductor in contact with the system, while the right shows the feedthrough removed from the system.

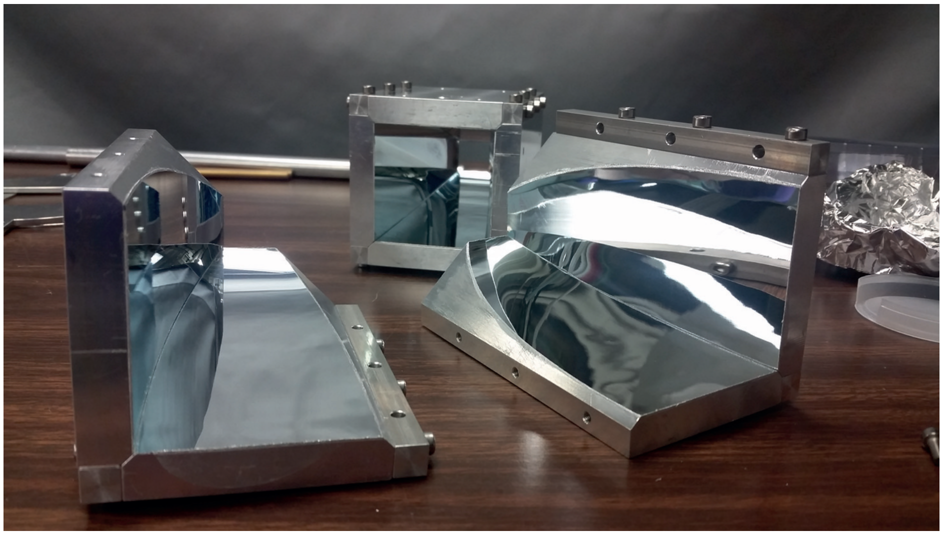

Figure A.13: A photograph of the CPC assembly. Two halves of one CPC are shown in the foreground, while in the back, a fully assembled CPC can be seen. The wide side attaches to the side window of the beam pipe, and the PMT is attached to the narrow end.

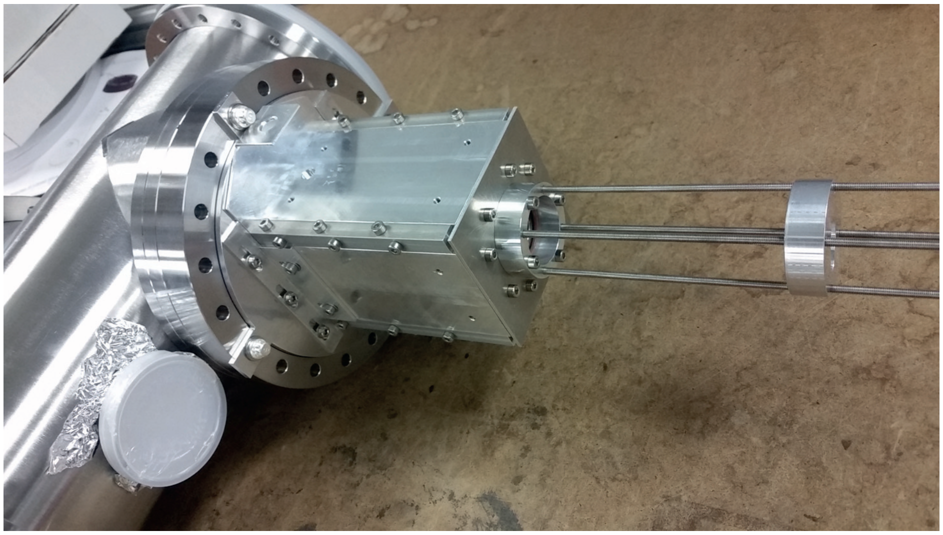

Figure A.14: A photograph showing the assembly of the exterior components of the PDS. An adjustable aperture of aluminum plates is attached to the window, with the CPC following. At the right end of the CPC, the mounting hardware for a PMT is shown. The face of the PMT presses up against a rubber O-ring on the CPC, while the back end is held tightly using a plate held by threaded rods protruding from the CPC.

Two rows of Velcro strips were used to attach the light proofing cloth, and dark counts in each PMT were less than 100 /s.

A.1.3 Further simulations

In order to understand the two peak structure seen at the focal plane (see Section 2.3.2.2), several more simulations were performed. Three potential sources of this unexpected profile were identified: A misalignment of the PDS with the source of the signal (possibly on the order of 0.5 mm), a misalignment of the PDS relative to the window on the beamline (on the order of 3 mm), or finally, a slight deviation from the elliptical shape at the point with the strongest curvature (due to a slight crease needed in the foil to allow it to bend into shape).

The simulation was repeated using each of these possible deviations from the ideal design of the system. It was found that while all three possibilities can cause a slight reduction in signal at the center of the focal plane, the simulation most closely resembling the observed structure involved a combination of deformation in the ellipse, and an offset of the beam from the focus of the ellipse. These results are shown in Figure A.15. Although the reflective foil is convenient and only a small section at the sharpest point of the ellipse shows a significant deformation, this region does represent a significant solid angle of the signal due to its proximity to the beams. In the future, these elliptical surfaces may be hand polished, rather than using the foil. This may provide a more accurate elliptical geometry, and allow a better focused single peak of signal at the focal plane.

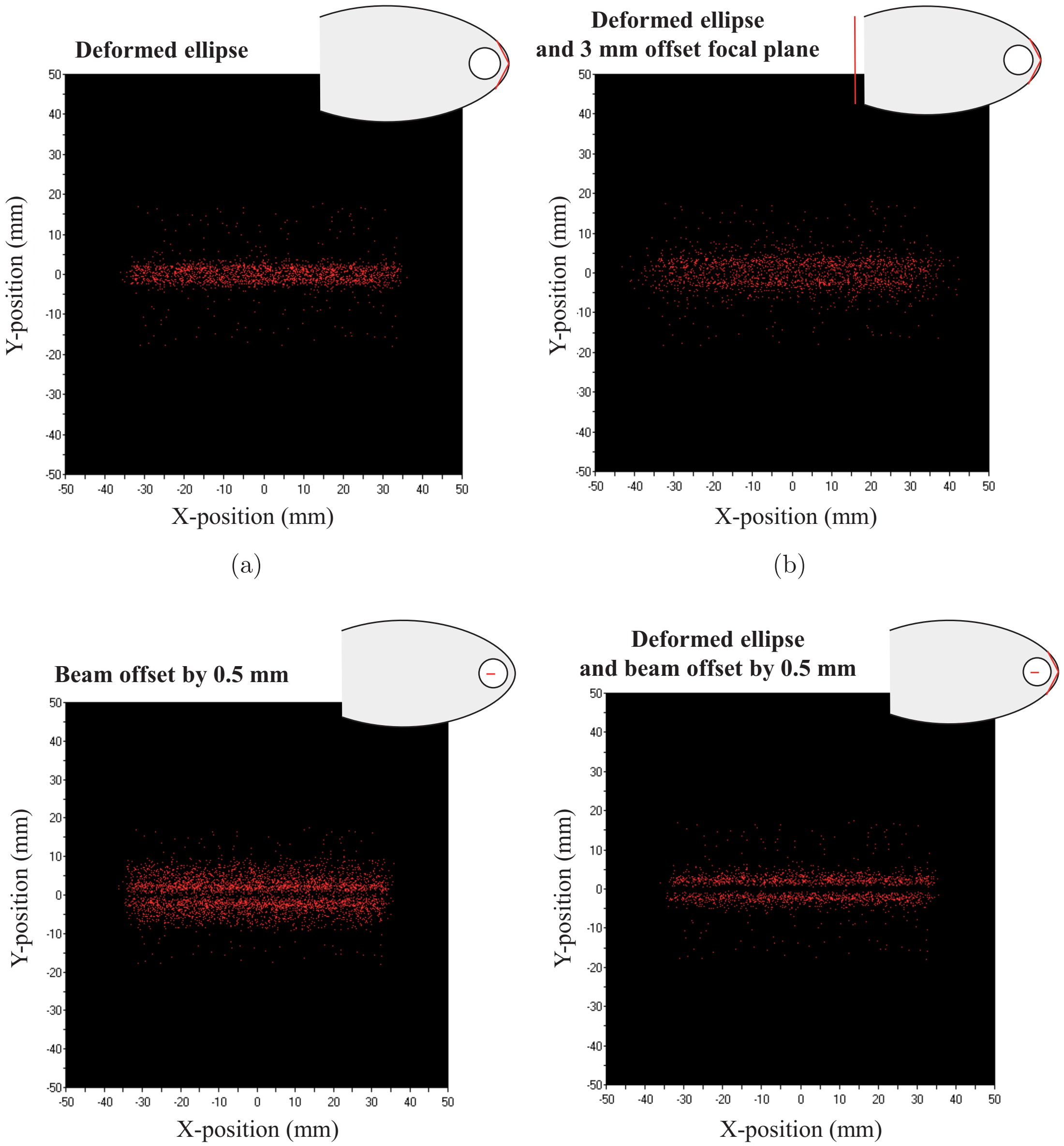

(a) (b)

(c) (d)

Figure A.15: Several simulations incorporating possible systematic differences which may be present in the actual detection system. (a) Shows the effect of adding a slight crease to the point of the ellipse, something which occurs in the actual system due to the thickness of the foil used to create the reflective surface. (b) Shows how the "splitting" of the signal is exaggerated further if the location of the aperture is slightly off from the true focal plane. (c) Shows another possible source of the two-peak structure, by slightly offsetting the source of the signal from the focus of the elliptical region. (d) Shows the simulation which was best able to match the experimentally observed signal profile, using a combination of a (a) and (c). In a future modification to the system, the elliptical regions may be hand polished rather than using the reflective foils, in order to more accurately produce the elliptical shape.

A.2 PIG source

The Penning Ionization Gauge (PIG) source is a versatile plasma sputtering source that was constructed at BECOLA in 2015. An anode, with a large opening, sits at the center of the plasma, while a cathode and anti-cathode sit on either side. These are surrounded by a magnetic field, and a buffer gas is fed into the source in order to sustain a plasma. A small hole in the cathode allows the ions generated in the source (both ions from the buffer gas, as well as those sputtered off of the cathodes) to be extracted in a beam. Any conductive element that can be machined to the dimensions required for the cathode can be used in the source. Several elements have been used as cathodes to produce reference ions so far including Fe, Ni, Sc, Zr, and now in this experiment, a Sn-Ca alloy was used.

Recent upgrades to the PIG source were mentioned in Section 2.3.1.1 and a few more technical details, which may be useful for future operation or experiments, are described here.

A.2.1 Mass flow controller

Prior to this experiment, a mass flow controller (MFC) was obtained in order to allow a better control of the flow of gas into the PIG source. The device in use at the time of this writing is from Bronkhorst, model number F-200CV-002-AGD-22-V. The MFC and surrounding components can be see in Figure A.16. An identical MFC has also been purchased as a backup, and is in storage.

This MFC uses a 9-pin D-sub connector for both power supply and control interface. It has two primary control modes, digital and analog. Because it utilizes a single connector for device power and both of these control modes, a custom “T” connector was created. One end of this connector goes into the MFC, and two 9-pin connectors are on the other end. One of these connectors allows connection to the analog control pins, and the power supply for the device. The other can be connected to a PC for RS232 communication (of course this can only be connected when the high voltage system is OFF). A schematic indicating the wiring of this connector is shown in Figure A.17.

When operating in the digital mode, and connected via RS232 (only when the high voltage is OFF) the gas flow can be controlled using the Bronkhorst control software. In the analog control mode, the device controls the flow of gas based on a current applied to pin 3, while a readout of the gas flow is provided by a current output on pin 2. These currents are in a range from 4–20 mA and are in use now to control the device via the PLC system in the electronics rack within the high voltage cage. These currents can be controlled and read as a percentage on the PIG source control page.

In order to enable this analog control, the control mode was selected using the configuration software while the device was connected to the computer via RS232. This control mode selection has already been performed for the backup MFC as well, so a direct swap of the two should not yield any change in behavior or operation of the system.

Two challenges arose when installing the MFC, isolating the high voltage, and preventing gas leakage while the MFC was closed. To remedy these issues, the MFC sits on a rubber insulator, on a bracket protruding from the wall, so that there is no leakage current when the system is brought up to high voltage, and a shutoff valve is installed directly following the MFC. When not operating the PIG source, this green shutoff valve can be closed to prevent any gas leaking through into the system.

When changing the gas attached to the MFC, it is important to flow the gas through the long rubber tube for a few minutes to clear the line (3 min seems sufficient). While the gas

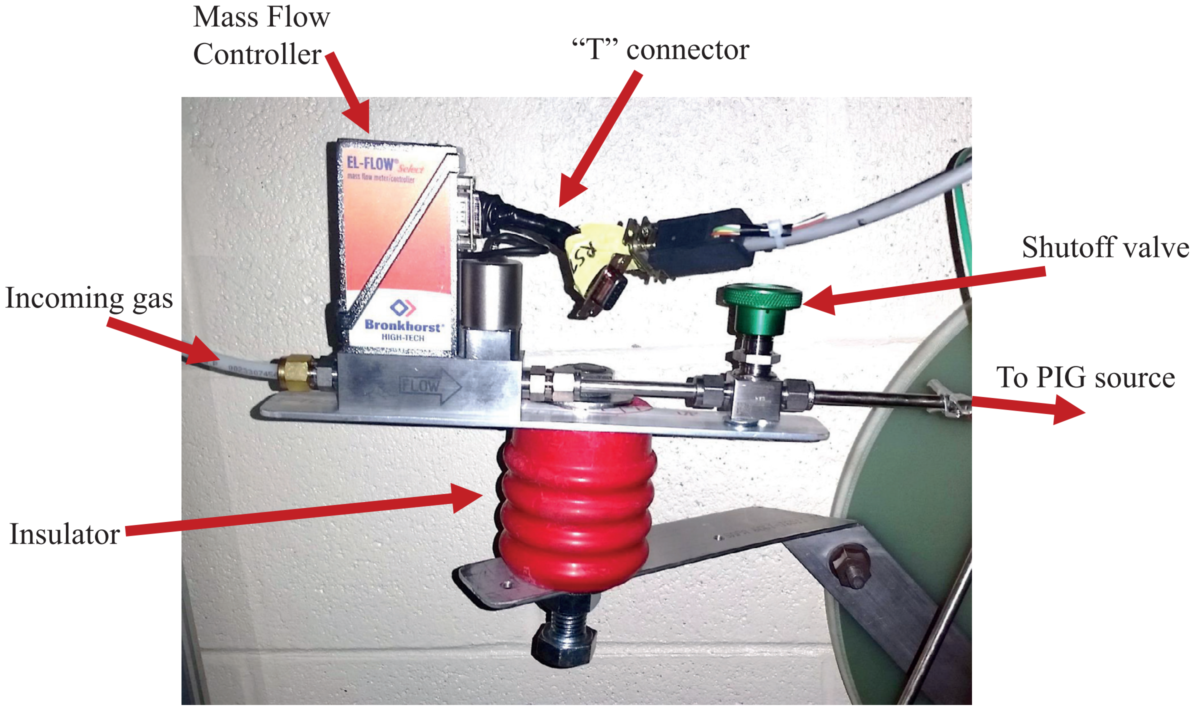
Mass Flow
Controller
“T” connector
Shutoff valve
Incoming gas
To PIG source
Insulator
EL-FLOW Select
Bronkhorst HIGH-TECH
FLOW

Figure A.16: Photograph of the MFC and surrounding components. The open 9-pin connector seen on the “T” connector can be attached to a computer via an RS232 serial cable when the system is not on high voltage. The insulator is necessary to prevent current leakage when the PIG source is raised on the high voltage. Originally, the bent aluminum bracket was thought to be sufficient, however there was an excessive amount of leakage current when the MFC was connected there directly. When not operating the PIG source, the shutoff valve can be closed to allow a better vacuum in the PIG source.

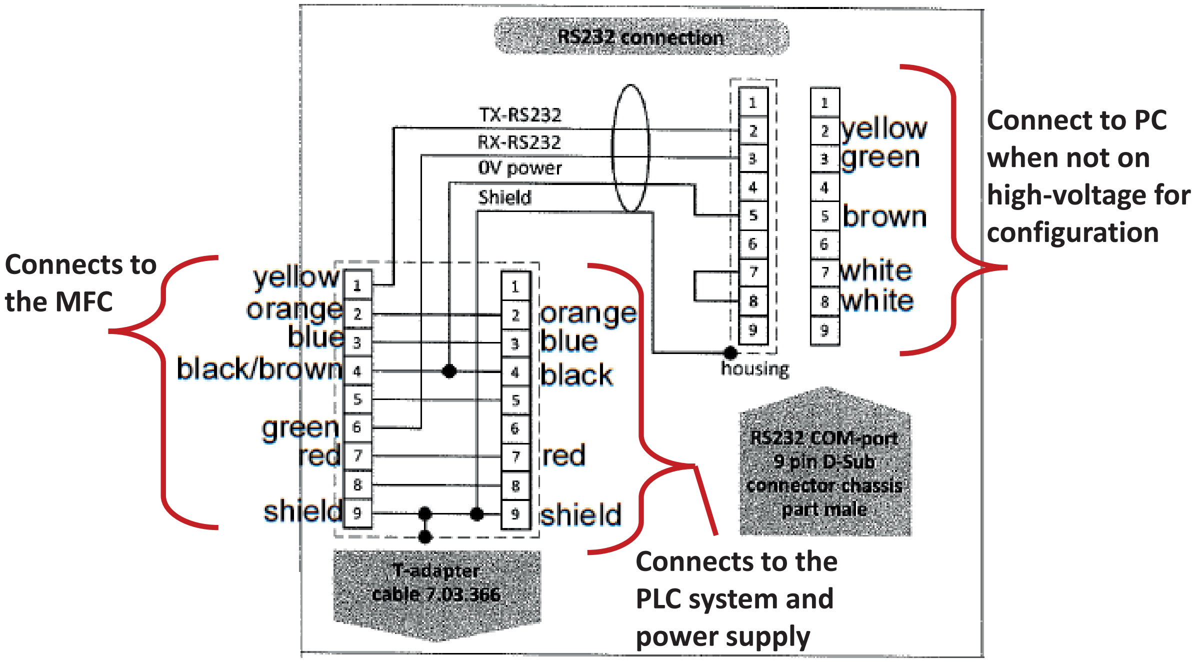
RS232 connection
TX-RS232
RX-RS232
0V power
Shield
Connect to PC when not on high-voltage for configuration
yellow
green
brown
white
white
housing
Connects to the MFC
yellow
orange
blue
black/brown
green
red
shield
orange
blue
black
red
shield
RS232 COM-port 9 pin D-Sub connector chassis part male
T-adapter cable 7.03.366
Connects to the PLC system and power supply

Figure A.17: Schematic showing the wiring of the custom "T" connector being used for the MFC. The diagram is taken from the manual provided by Bronkhorst, and color labels are added to indicate the actual wires used within the connector. The left side of this figure connects to the MFC, and the connection on the lower right allows for power and analog controls to be attached. The upper right connector is used for serial communication with a PC, and is not usually connected.

is still flushing out the line, it can then be connected to the MFC. If the line is not flushed out, changes in pressure, despite the MFC flow appearing stable, will be seen for the first hours of the PIG source operation. This is due to the gradually changing composition of the gas entering the MFC.

When operating the MFC, a small spike in pressure may be seen when gas flow is first initiated. This is normal, and should quickly stabilize. The control range of the MFC is given in percent of the maximum flow. It is rated for a maximum of $0.7\,\mathrm{ml_n/min}$, but the actual flow rate depends on the gas being used. The minimum controllable flow is around $2\,\%$ of the max range.

Additional technical specifications from Bronkhorst and the calibration certificate of the MFC purchased by BECOLA can be found in my documentation in the BECOLA directory.

A.2.2 Higher charge states

Although singly-ionized calcium was used as a reference in the online experiment, several offline tests were performed to examine doubly-charged calcium ions from the reference source, in case the majority of the rare calcium ions delivered to BECOLA turned out to be doubly-charged. Tests were performed with the cooler RF set to $5.34\,\mathrm{MHz}$, $900\,\mathrm{V_{pp}}$, and the bunching region set to $1.2\,\mathrm{MHz}$, $56\,\mathrm{V_{pp}}$. At this setting, no singly-charged ions were seen using laser spectroscopy, and so it was assumed that the beam consisted entirely of doubly-charged ions.

Following the CEC, the ion beam current was measured using a Faraday cup (FC) with and without a $50\,\mathrm{V}$ repeller potential. The difference in these currents allows a measurement related to the number of particles present, regardless of charge (assuming each charge state produces the same number of secondary electrons when impinging on the FC). By comparing this “total particle” measurement to the current measured with a voltage applied to the ion-kicker which is located just after the CEC, the fraction of the beam consisting of neutral atoms is obtained. The total beam current of the charged particles can be found using the FC measurement without the kicker, and without the 50 V repeller potential. Using the beam current measured before the CEC, assuming a transmission of 98 % (measured prior to heating the CEC), and taking into account the fraction of neutral atoms measured, the fraction of singly- and doubly-charged ions can be obtained. This measurement was performed as the CEC was warmed up, and the results are shown in Figure A.18. Large error bars have been placed on these results, as the assumptions above that the transmission was consistent, and all charge states produce the same amount of secondary electrons when striking the FC are far from perfect. Indeed, some extrapolations suggest a negative fraction of doubly-charged ions, an obvious impossibility, but the general trend does reveal that the cross sections for both single and double charge exchange do increase with temperature, and the presence of both singly-charged ions and neutral Ca was confirmed using CLS.

A.3 DVM interface

Two digital volt meters (DVMs) are used to precisely record voltages in the BECOLA system. One is used in conjunction with the large $10,000:1$ voltage divider connected to the cooler/buncher high voltage (the FuG power supply). The second is connected to the small chip based $1,000:1$ voltage divider which is connected to the scanning potential (the Matsusada power supply). These two meters are an Agilent 34410A, and a newer, but compatible model, Agilent 34465A.

The lab’s EPICS system is used to communicate with these DVMs and configure their

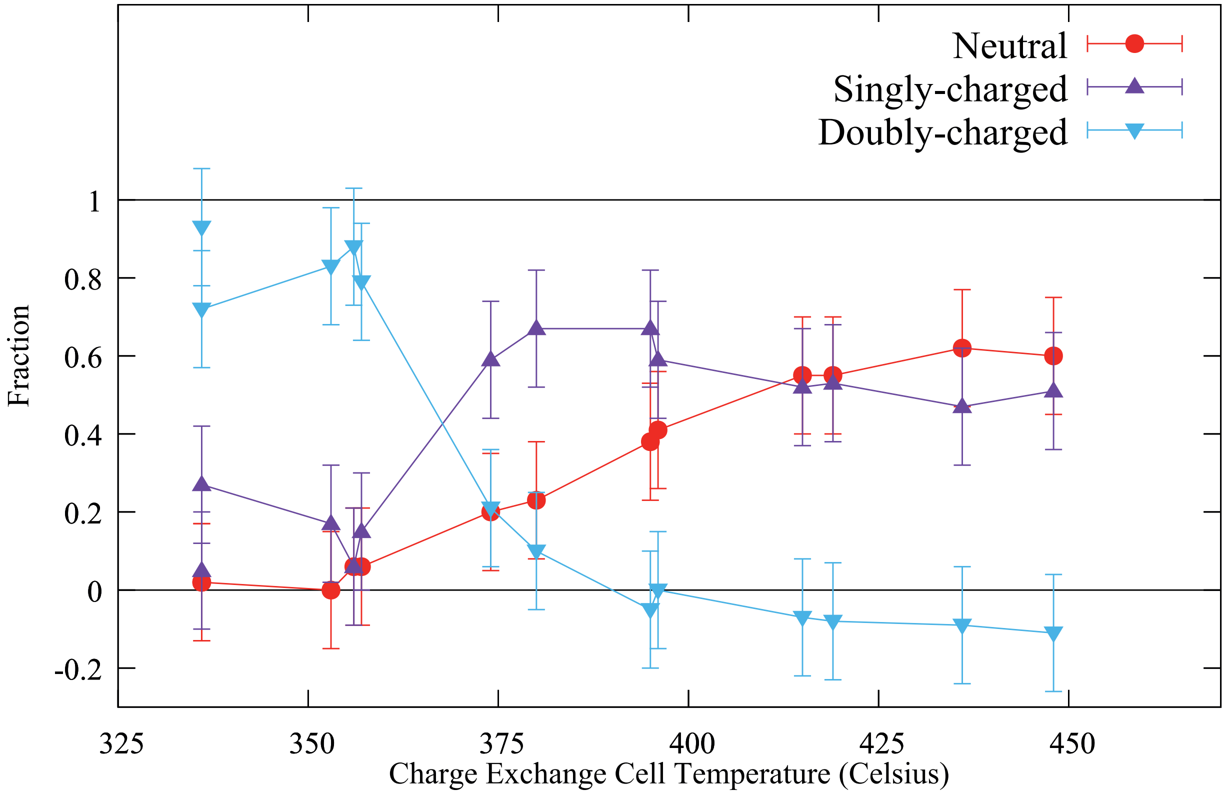

Figure A.18: Data taken using doubly-charged ^{40}Ca ions. The cooler/buncher was set to allow doubly-charged ^{40}Ca ions to pass through, and singly-charged ions were rejected (verified using spectroscopy). As the CEC temperature was increased, ion beam currents were measured after the CEC with and without the ion kicker. By measuring the total current from the doubly-charged ion beam prior to the CEC, assuming a total transmission through the CEC of 98 %, and measuring the neutral and charged beam current, the fraction of atoms in each charge state can be determined. While this method is not very precise, it does show that the cross section for the double and single charge exchange process increases with temperature.

Table A.2: These channels are used to control the DVMs. Identical channels exist for `MTER_N0002`. `V_RD` is the channel where the voltage is actually displayed. `POLL_TXT` is the SCPI message sent to poll the device. Using a command other than the one shown here may inadvertently reset the measurement settings on the device. `V_RD.SCAN` is used to determine how often the voltage is read. `RST_CMD` must be set to `1` each time the DVM is power cycled, in order to run the `RST_TXT` commands. The `SCPI` channels can be used to send commands and queries to the DVM, if a query is sent the response is shown in the reply channel. The commands in the `RST_TXT` channels here reset the DVM, then configure the voltage range and precision, and finally enable the high impedance mode. Note that a higher precision and thus slower polling rate is used for the FuG, while a lower precision and faster polling rate is used for the Matsusada. For more details on the SCPI commands which are recognized by the DVMs, see the SCPI programming guide from Agilent.

Channel	Typical Setting
`DBEC_BCLS:MTER_N0001:V_RD`	read channel
`_DBEC_BCLS:MTER_N0001:POLL_TXT`	`READ?`
`DBEC_BCLS:MTER_N0001:V_RD.SCAN`	`5` (FuG) `.5` (Matsusada)
`DBEC_BCLS:MTER_N0001:RST_CMD`	`0`
`_DBEC_BCLS:MTER_N0001:SCPI_CMD`	send SCPI commands
`_DBEC_BCLS:MTER_N0001:SCPI_QUERY`	send SCPI queries
`_DBEC_BCLS:MTER_N0001:SCPI_REPLY`	read channel
`_dev_DBEC_BCLS:MTER_N0001:RST_TXT.AA`	`*RST`
`_dev_DBEC_BCLS:MTER_N0001:RST_TXT.BB`	`CONF:VOLT:DC 10,3E-7` (FuG) `CONF:VOLT:DC 10,3E-6` (Matsusada)
`_dev_DBEC_BCLS:MTER_N0001:RST_TXT.CC`	`VOLT:IMP:AUTO ON`
`_dev_DBEC_BCLS:MTER_N0001:RST_TXT.DD`	empty

settings. This allows these voltages to be archived, as well as making them available to be read on a channel that is recorded into the data files by the BECOLA DAQ during experiments. The control method used is a serial communication interface, SCPI. In order to obtain precise measurements which are refreshed at the appropriate rate, several configuration options should be changed from the defaults. The high-impedance mode should be turned on, and the measurement range and precision should be set accordingly. Higher precision measurements require integration over a larger number of power-line cycles (the 60 Hz AC powering the device).

For a recording of the stable high voltage for the cooler/buncher, the precision is more important than the time between measurements, so the measuring mode with the least uncertainty (100 power-line cycles) is used to record a new measurement every 1.6 s. In the case of the scanning voltage, where the voltage is changed every few seconds, a higher polling-rate is required, so a higher uncertainty is preferred.

These settings to configure and read from the DVMs are contained in the EPICS system. The main channel prefix for the two BECOLA DVMs are `DBEC_BCLS:MTER_N0001` and `DBEC_BCLS:MTER_N0002`. There are a number of related channels which can be used for configuration of how the system polls the device, and the example channels from here forward will use `MTER_N0001`, but replacing this with `MTER_N0002` will yield the same channels for the second DVM. The voltage can be read using the sub-channel `:V_RD`, and `:V_RD.SCAN` determines how frequently the device is polled. A reset of the meter can be performed by setting the `:RST_CMD` channel to `1`. This channel will quickly set itself back to `0`, but the four commands stored in channels `_dev_DBEC_BCLS:MTER_N0001:RST_TXT.AA`, `:RST_TXT.BB`, `:RST_TXT.CC`, and `:RST_TXT.DD` will be sent to the volt meter. The parameters stored in these text channels should be the SCPI commands desired to reset the device and configure it. An explanation of the settings used currently for the two DVMs is shown in Table A.2.

There are four other configuration channels with a different prefix, `_DBEC_BCLS:MTER_N0001` (note the `_`). These channels are `:POLL_TXT`, which holds the SCPI command used to poll the device, `:SCPI_CMD` and `:SCPI_QUERY`, which can be used to send a command or query to the device, and `:SCPI_REPLY` which will update to show the response from the device in the case of a query.

Several Agilent DVMs are used by the electronics group in temporary setups under the channels `HPTEST1-HPTEST4`. The channels they use for configuration take a slightly different format but have similar purposes. The channels for these DVMs, as well as all the BECOLA DVM channels mentioned in this section can be seen in the QTparam file located in the BECOLA folder at `controls\dvm_settings.prm`. The HPTEST channels should not be used as examples, as the SCPI commands they use are typically not well configured. They use `MEAS:VOLT:DC?` as the SCPI command used to poll the device, which resets the measurement settings to defaults each measurement. More details about the HPTEST channels, including reviewing their logs through the EPICS system, can be found in the “High Voltage Monitoring” document in my folder in the BECOLA directory.

When running an experiment, it is important to check that both DVMs are configured properly. After power-cycling the DVM, be sure to send the value `1` to the reset channel to run the configuration commands. After this has been done, the DVMs display should indicate that it is using a manual range, and the “Hi-Z” impedance mode. The voltage readouts can then be monitored with QtChart live. They will also be recorded for each scan point in the experiment, and saved into the data files as described in Appendix B.

A.4 Waveform generator interface

In order to produce the RF field for the RFQ traps in the cooler/buncher, two waveform generators are used. The lower waveform generator in the rack, a BK Precision 4078B, has two separate output channels, which are used to power the two out-of-phase electrode pairs in the downstream bunching section. To control this device, because it is raised on the high voltage with the entire cooler/buncher, fiber-optic network cables are the only way to enter the high voltage cage.

Unfortunately, the 4078B can only be controlled via USB. The device has an ethernet port

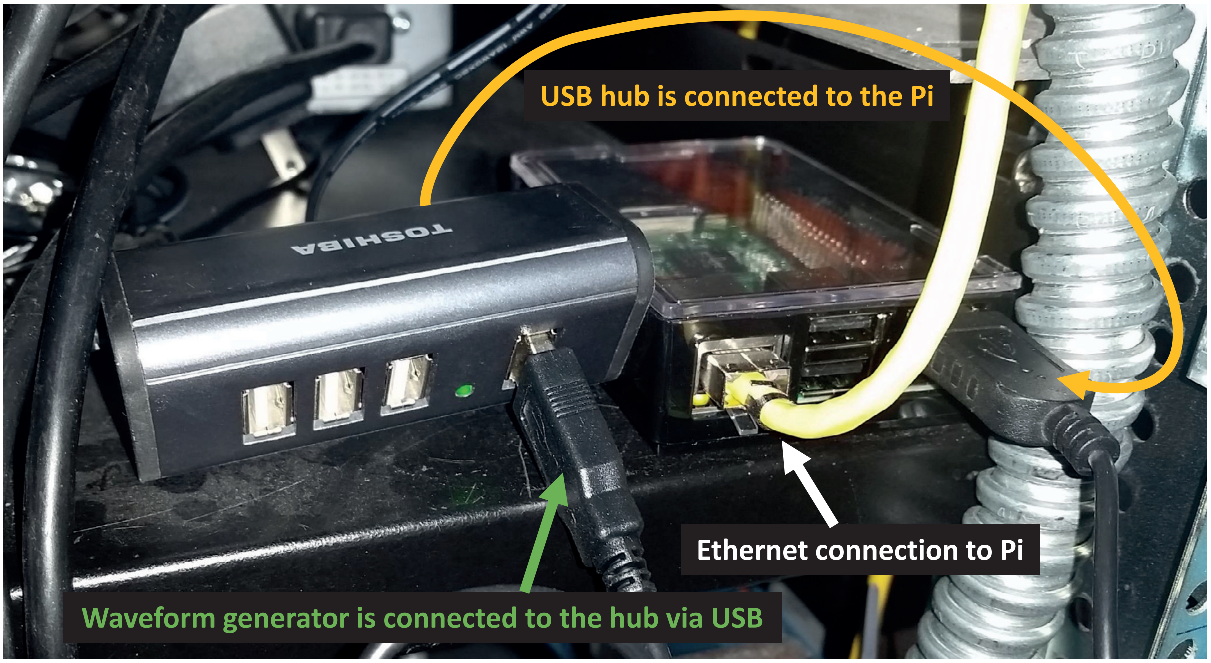
USB hub is connected to the Pi
TOSHIBA
Ethernet connection to Pi
Waveform generator is connected to the hub via USB

Figure A.19: Photograph of the Raspberry Pi 3B+ and its connections used to interface with the waveform generator. This is in the rack inside the high voltage cage. Rather than connect the waveform generator directly to the Pi, a USB hub must be placed in between, otherwise the Pi does not recognize the device.

on the back panel, but as far as I can determine from the documentation and contact with the manufacturer's support, it is a non-functional port. The predecessor to this waveform generator possessed a serial communication port, and so an ethernet to serial converter was used to control the device remotely. Unfortunately, that waveform generator was damaged when a high voltage spark occurred, and the communication through the serial port was broken. To bring the same functionality to this new model, the ethernet cable is connected to a Raspberry Pi, which essentially functions as an ethernet to USB adapter.

A Raspberry Pi 3B+ is used which has the Raspbian operating system (Debian-based

Linux distribution), and a small Python script runs constantly to listen on the network for the packets from the IOC which were previously sent to the ethernet to serial adapter, and the commands are interpreted, and sent to the waveform generator with the USBTMC protocol. If a query is sent to the waveform generator, the response is sent back on the ethernet to the IOC. Because of some sloppiness in the USB specification adherence of either the Pi or the BK4078B, USB communication is not possible without the use of a simple, non-powered USB hub between the Pi and the waveform generator. These connections are shown in Figure A.19.

The Pi is configured with a startup script which runs automatically and initiates the Python script, so aside from perhaps occasionally power-cycling the Pi and the waveform generator, no steps should be needed to initiate the connection. For the full details of how the Raspberry Pi is configured, with regard to the network, and the Python packages used for the USB connection, a README file is included alongside all the relevant scripts in my directory, under `"Documentation\BK 4078B Interface"`. A spare Raspberry Pi is in one of the cabinets, but has not yet been configured.

APPENDIX B

Software tools

For this experiment, I performed my analysis using a number of scripts in ROOT. Other experimenters have used scripting such as Mathematica, Python, and Origin. The methods used to calibrate and analyze the data have been described within the main chapters, however these technical details may be useful to future experimenters who may be utilizing or building off of the codes I have used. The scripts detailed below are all located within my folder in the BECOLA directory, under `"ROOT Analysis Tools\"`, but are intended to be run using ROOT on the fishtank.

B.1 BECOLA analysis with ROOT

B.1.1 ROOT file structure

The DAQ at BECOLA stores the data in `.mda` files, which use a binary format. Prior to analysis with any script or program, it is useful to convert these data into ASCII files, allowing them to be read as text. These ASCII files are large and take some time to read, so to perform the analysis in ROOT, I convert the data into another binary format, a ROOT Tree, to allow it to be read quickly when compiling the histograms and performing fits.

To quickly convert from `.mda` files, there is a PERL script called `mdaconvert_ajm_regions.pl` which looks for `.mda` files within a `data` directory, and runs `mda2ascii_64` on each file, using the options `-mt1f`. After creating `.asc` files for each run, it then uses ROOT to run `rootscripts/asc_to_root_v5.C`, which will create a `.ROOT` file for each run, containing the data in a Tree. These scripts are built on the ones developed by Dominic Rossi.

After converting the data using the above methods, analysis can be performed using the tools described in Section B.1.2. Here I will describe the basic format of the ASCII files, as well as the ROOT Tree.

Data from the DAQ is taken in several dimensions. Currently, the data is stored in a 5-D format. To read the appropriate values from the ASCII file, a line with more than 12 numbers is identified as the start of a specific measurement. There are 31 columns in these lines, and they hold the following information:

- `1`: 5-D index (beginning from 1) the scan or run number (saved to the ROOT tree as `run`).
- `2`: 4-D index (beginning from 1) the region number (saved to the ROOT tree as `region`).
- `3`: 3-D index (beginning from 1) the voltage step number (saved to the ROOT tree as `vstep`).
- `4`: 2-D index (beginning from 1) unused dimension, always 1 (saved to the ROOT tree as `p4`).
- `5`: 1-D index (beginning from 1) the time bin number (1-1024).
- `6`: 5-D positioner (beginning from 0) similar to `1` but counting from 0 (saved to the ROOT tree as `run_bin`).
- `7`: 4-D positioner (beginning from 0) similar to `2` but counting from 0 (saved to the ROOT tree as `region_bin`).
- `8`: 3-D positioner (beginning from 0) similar to `3` but counting from 0 (saved to the ROOT tree as `vbin`).
- `9`: 3-D detector 1, DAC voltage setting (saved to the ROOT tree as `dac_set`).
- `10`: 3-D detector 2, DAC raw voltage reading (saved to the ROOT tree as `raw_dac`).
- `11`: 3-D detector 3, `VD_D1285` the DAC voltage reading (saved to the ROOT tree as `dac_read_plc`).
- `12`: 3-D detector 4, `MTER_N0001` Matsusada voltage divider reading (saved to the ROOT tree as `dac_read_dvm`).
- `13`: 3-D detector 5, `HPTEST1` unused DVM reading (saved to the ROOT tree as `hptest1_read`).

- `14:` 3-D detector 6, `MTER_N0002` FuG DVM reading (saved to the ROOT tree as `bcb_voltage_read`).
- `15:` 2-D positioner, (beginning from 0) similar to `4` but counting from 0 (saved to the ROOT tree as `p15`).
- `16:` 1-D detector 1, The time (in seconds) of this specific time bin (saved to the ROOT tree as an array called `time`).
- `17:` 1-D detector 2, channel 0 counts recorded in this specific bin, typically the PMT from the old detection system (saved to the ROOT tree as an array called `phot`).
- `18:` 1-D detector 3, channel 1 counts recorded in this specific bin, typically the PMT from the upstream new detection system (saved to the ROOT tree as an array called `sciup`).
- `19:` 1-D detector 4, channel 2 counts recorded in this specific bin, typically the PMT from the downstream new detection system (saved to the ROOT tree as an array called `sci_dn`).
- `20-31:` 1-D detector 5-17, channel 3-15 counts recorded in this specific bin, typically unused (saved to the ROOT tree as arrays called `scal4-scal16`).

1024 rows of this format are read in to give a single entry into the ROOT tree. From these 1024 rows, as indicated above, the 1-D detector and 1-D index values are combined into an array. In this format the data can easily be compiled into 2D histograms, as each entry in the Tree contains the complete data from a single voltage step.

A simple example script, showing how one of these ROOT trees can be compiled into a 2D (time, voltage) histogram can be found in my folder:

`"ROOT Analysis Tools\Reading from ASCII\becolatree.C"`.

This file can be compiled in ROOT, and the `becolatree_run` function can then be executed. Although this file does not carefully bin the data, it can be useful to understand how ROOT Trees work, and how to compile the data to begin performing fits.

B.1.2 Analysis tools

The complete set of scripts used for analysis is located in `"ROOT Analysis Tools\e16003"`. A description of the procedure used to perform the analysis can be found in `Procedure.txt`.

Each script is meant to be compiled and run using ROOT on the `fishtank`. For example, the first step to process the data uses `caSections.C`. This program has a list grouping the files into sections, and will perform the time cut, and flatten the section into a 1D histogram. The macro files, `SectionMacro1NoDVM` and `SectionMacro2NoDVM` contain a list of calls to the function in `caSections.C`. The way that these lists were generated can be seen in the `FinalAnalysis` Excel spreadsheet, located in the `Excel Files` folder. On the "Run Summary" page, several columns at the far right generate lists of function calls to be run on each section. Note that some time cutoffs are hard coded here based on data from multiple sections combined, or for channel 2, shifted based on the time cuts from channel 1.

To perform the first step described in `Procedure.txt`, the program should be compiled and loaded into ROOT, and then the macros can be executed, using the following commands within the ROOT command prompt:

```
>.L caSections.C++
>.x SectionMacro1NoDVM
>.x SectionMacro2NoDVM
```

This produces a 1D histogram for each section, and from this, the calibration using the ^{40,44}Ca data can be performed. Using `calib40_44.C` and `Macro4044.C`, calibrated fits of the reference isotopes can be obtained. In the "Section Calibration" page of the Excel file, each set of 40 and 44 data gives a "Specific Calibration" in column F, neighboring calibrations are then averaged to determine an "Average Calibration" in column G.

This "Average Calibration" voltage was then used for the rare isotope data for each section, it can be found in the "CalibFitMacro" files. Now that each section has been calibrated, the sections of each rare isotope can then be combined together. There are many scripts present to do these combinations, in general, they are named according to the isotope

(36, 37, or 38) and then the channel (1 or 2), and in some cases will also have C1 or C2 in the name, to indicate that they use a calibration obtained from channel 1, or channel 2.

When these section combinations are performed, the resulting histograms are calibrated and shifted so that the 0 point is the centroid of ^{40}Ca. The results of these fits, and the combination of channel 1 and channel 2 data to determine the isotope shift and uncertainty are in the Excel file, on the “Final Results” page.

There are also several ROOT scripts that can be used to create better plots (showing the residuals of the fit alongside the data). These are named in a straightforward manner.

Another Excel file is also included, “ChargeRadii Plot” which takes the isotope shifts, and converts them into the differential and absolute charge radii using the atomic factors.

APPENDIX C

Personal contributions

C.1 Publications

- Charge radii of neutron-deficient ^{36,37,38}K

  Phys. Rev. C 92, 014305, July 7, 2015

  I was responsible for the operation of a pair of electro-optic modulators for this experiment. I simulated the resulting frequency spectrum of the laser light for several different frequency configurations, then set up the required electronics to drive them at these frequencies and used an interferometer to evaluate their real life behavior. I also wrote a detailed set of instructions for their operation during the run of the experiment, and took shifts during the experiment.

- Population distribution subsequent to charge exchange of 29.85 keV Ni^{+} on sodium vapor

  Spectrochimica Acta Part B, 113, 16-21, November 1, 2015

  I participated in the data collection for this experiment, including the operation of the PIG source, and provided comments on the paper.

- Charge radii of neutron deficient ^{52,53}Fe produced by projectile fragmentation

  Phys. Rev. Lett. 117, 252501, December 15, 2016

For this work, I was responsible for the laser system. Through several modifications to the optical system where the laser is introduced to the beamline, I was able to improve the collimation of the laser system and reduce the laser background by a factor of 3. During the run of the experiment I was in charge of changing frequencies and aligning the laser as needed, as well as leading a shift. I also performed an independent data analysis for this experiment in order to verify the results.

- First determination of ground-state electromagnetic moments of ^{53}Fe

  Phys. Rev. C 96, 054314, November 16, 2017

  This paper uses the same experimental data as the publication mentioned above. I prepared the first draft of the Experiment and Result section, as well as the Discussion sections regarding the Buck-Perez systematic relation and Isoscalar spin expectation value. I also helped prepare the figures and edited the final draft for submission.

- Proton superfluidity and charge radii in proton-rich calcium isotopes

  Nature Physics, 15, 432-436, February, 2019

  I was responsible for simulating and installing the upgraded PDS as described in this thesis, including leading the data collection and analysis used to characterize the new detector and decide the configuration used during the online experiment. I was responsible for operating the offline ion-source during this experiment, including the installation and setup of an MFC, and preliminary tests leading up to the experiment using various buffer gases, charge states, and the CEC. I also performed the SNR calculations used to select the bunch release period for the short-lived isotopes. Following the online experiment, I performed the calibration of the data and the extraction of the charge radii. I wrote the portions of the paper describing the experiment and extraction of the charge radii, led the editing process, and helped prepare the figures.

- Ground-state electromagnetic moments of ^{37}Ca

  Phys. Rev. C, 99, 061301(R), June, 2019

  This paper examines the nuclear moments extracted from the same experimental data as the paper mentioned above. I provided the calibrated data, and performed a parallel analysis of the nuclear moments to confirm the results. I also helped prepare the figures and provided comments on the manuscript.

C.2 Presentations

- Off-line production of transition metal ions for collinear laser spectroscopy at BECOLA/NSCL

  7th International Conference on Laser Probing (LAP2015), East Lansing, MI, June 7, 2015. *(Poster/Talk)*

- Charge radii measurements at BECOLA

  Low Energy Community Meeting, East Lansing, MI, August 21-22, 2015. *(Talk)*

- Population distribution following atomic charge exchange of 29.85 keV Ni^+ on a sodium vapor

  Division of Nuclear Physics Meeting of the American Physical Society, Santa Fe, NM, October 28-31, 2015. *(Talk)*

- Charge radii and nuclear moments of ^{52,53}Fe, and the shell-closure signature at $N = 28$

  Nuclear Structure, Knoxville, TN, July 24-29, 2016. *(Poster/Talk)*

- Toward charge radii measurements of neutron-deficient Ca

  Division of Nuclear Physics Meeting of the American Physical Society, Vancouver, BC, Canada, October 13-16, 2016. *(Talk)*

- Collinear laser spectroscopy of stable Zr in preparation for future pulsed laser techniques

  NNSA Stewardship Science Academic Programs, Naperville, IL, April 12-13, 2017. *(Poster)*

- Nuclear moments of ^{53}Fe, and the shell-closure signature at $N = 28$

  Advancements in Radioactive Isotope Science, Keystone, CO, May 28-June 2, 2017. *(Poster)*

- Charge radii measurements of neutron-deficient Ca

  Division of Nuclear Physics Meeting of the American Physical Society, Pittsburgh, PA, October 25-28, 2017. *(Talk)*

- First determination of nuclear ground-state electromagnetic moments of $T = 3/2$ ^{37}Ca

  Nuclear Structure 2018, East Lansing, MI, August 5-10, 2018.*(Poster)*

- RFQ ion trap for laser spectroscopy measurements at BECOLA facility

  International Conference on Trapped Charged Particles and Fundamental Physics (TCP2018), Traverse City, MI, September 30-October 5, 2018. *(Talk)*

- Charge radii of neutron-deficient ^{36,37,38}Ca

  Joint Meeting of the Nuclear Physics Divisions of the APS and the JPS, Waikoloa Village, HI, October 23-27, 2018. *(Talk)*

REFERENCES

REFERENCES

[1] E. Rutherford. The structure of the atom. *The London, Edinburgh, and Dublin Philosophical Magazine and Journal of Science*, 27(159):488–498, 1914.

[2] R. Hofstadter. Electron scattering and nuclear structure. *Rev. Mod. Phys.*, 28:214–254, Jul 1956.

[3] D. Ni, Z. Ren, T. Dong, and Y. Qian. Nuclear charge radii of heavy and superheavy nuclei from the experimental α-decay energies and half-lives. *Phys. Rev. C*, 87:024310, Feb 2013.

[4] I. Angeli and K. P. Marinova. Table of experimental nuclear ground state charge radii: An update. *Atomic Data and Nuclear Data Tables*, 99:69–95, Jan 2013.

[5] I. Tanihata, H. Hamagaki, O. Hashimoto, Y. Shida, N. Yoshikawa, K. Sugimoto, O. Yamakawa, T. Kobayashi, and N. Takahashi. Measurements of interaction cross sections and nuclear radii in the light p-shell region. *Phys. Rev. Lett.*, 55:2676–2679, Dec 1985.

[6] R. Neugart and G. Neyens. *Nuclear Moments*, volume 700, pages 135–189. Aug 2006.

[7] J. Billowes and P. Campbell. High-resolution laser spectroscopy for the study of nuclear sizes and shapes. *Journal of Physics G: Nuclear and Particle Physics*, 21(6):707–739, Jun 1995.

[8] K.-R. Anton, S. L. Kaufman, W. Klempt, G. Moruzzi, R. Neugart, E.-W. Otten, and B. Schinzler. Collinear laser spectroscopy on fast atomic beams. *Phys. Rev. Lett.*, 40:642–645, Mar 1978.

[9] A. Nieminen, P. Campbell, J. Billowes, D. H. Forest, J. A. R. Griffith, J. Huikari, A. Jokinen, I. D. Moore, R. Moore, G. Tungate, and J. Äystö. On-line ion cooling and bunching for collinear laser spectroscopy. *Phys. Rev. Lett.*, 88:094801, Feb 2002.

[10] K. Blaum, J. Dilling, and W. Nörtershäuser. Precision atomic physics techniques for nuclear physics with radioactive beams. *Physica Scripta*, T152:014017, Jan 2013.

[11] M. Block. Recent trends in precision measurements of atomic and nuclear properties with lasers and ion traps. *Hyperfine Interactions*, 238(1):40, Feb 2017.

[12] E. W. Otten. *Nuclear Radii and Moments of Unstable Isotopes*, pages 517–638. Springer US, Boston, MA, 1989.

[13] H.-J. Kluge and W. Nörtershäuser. Lasers for nuclear physics. *Spectrochimica Acta Part B: Atomic Spectroscopy*, 58(6):1031 – 1045, 2003. LAP-2002 International Conference on Laser Probing.

[14] B. Cheal and K. T. Flanagan. Progress in laser spectroscopy at radioactive ion beam facilities. *Journal of Physics G: Nuclear and Particle Physics*, 37(11):113101, Sep 2010.

[15] N. J. Stone. Nuclear magnetic dipole and electric quadrupole moments: Their measurement and tabulation as accessible data. *Journal of Physical and Chemical Reference Data*, 44(3):031215, 2015.

[16] P. Campbell, I. D. Moore, and M. R. Pearson. Laser spectroscopy for nuclear structure physics. *Progress in Particle and Nuclear Physics*, 86:127 – 180, 2016.

[17] T. Otsuka, T. Suzuki, M. Honma, Y. Utsuno, N. Tsunoda, K. Tsukiyama, and M. Hjorth-Jensen. Novel features of nuclear forces and shell evolution in exotic nuclei. *Phys. Rev. Lett.*, 104:012501, Jan 2010.

[18] A. Poves. Shell model spectroscopy far from stability. *Journal of Physics G: Nuclear and Particle Physics*, 44(8):084002, Jun 2017.

[19] P.-G. Reinhard and W. Nazarewicz. Nuclear charge and neutron radii and nuclear matter: Trend analysis in Skyrme density-functional-theory approach. *Phys. Rev. C*, 93:051303, May 2016.

[20] R. D. Evans. *The Atomic Nucleus*. Krieger Publishing Company, 2003.

[21] K. Minamisono, D. M. Rossi, R. Beerwerth, S. Fritzsche, D. Garand, A. Klose, Y. Liu, B. Maaß, P. F. Mantica, A. J. Miller, P. Müller, W. Nazarewicz, W. Nörtershäuser, E. Olsen, M. R. Pearson, P.-G. Reinhard, E. E. Saperstein, C. Sumithrarachchi, and S. V. Tolokonnikov. Charge radii of neutron deficient ^{52,53}Fe produced by projectile fragmentation. *Phys. Rev. Lett.*, 117:252501, Dec 2016.

[22] W. Nörtershäuser and C. Geppert. *Nuclear Charge Radii of Light Elements and Recent Developments in Collinear Laser Spectroscopy*, pages 233–292. Springer Berlin Heidelberg, Berlin, Heidelberg, 2014.

[23] D. M. Rossi, K. Minamisono, H. B. Asberry, G. Bollen, B. A. Brown, K. Cooper, B. Isherwood, P. F. Mantica, A. J. Miller, D. J. Morrissey, R. Ringle, J. A. Rodriguez,

C. A. Ryder, A. Smith, R. Strum, and C. Sumithrarachchi. Charge radii of neutron-deficient ^{36}K and ^{37}K. *Phys. Rev. C*, 92:014305, Jul 2015.

[24] E. Caurier, K. Langanke, G. Martínez-Pinedo, F. Nowacki, and P. Vogel. Shell model description of isotope shifts in calcium. *Physics Letters B*, 522(3):240 – 244, 2001.

[25] P.-G. Reinhard and W. Nazarewicz. Toward a global description of nuclear charge radii: Exploring the Fayans energy density functional. *Phys. Rev. C*, 95:064328, Jun 2017.

[26] R. F. Garcia Ruiz, M. L. Bissell, K. Blaum, A. Ekström, N. Frömmgen, G. Hagen, M. Hammen, K. Hebeler, J. D. Holt, G. R. Jansen, M. Kowalska, K. Kreim, W. Nazarewicz, R. Neugart, G. Neyens, W. Nörtershäuser, T. Papenbrock, J. Papuga, A. Schwenk, J. Simonis, K. A. Wendt, and D. T. Yordanov. Unexpectedly large charge radii of neutron-rich calcium isotopes. *Nature Physics*, 12:594–598, Feb 2016. Article.

[27] H. Nakada. Further evidence for three-nucleon spin-orbit interaction in isotope shifts of nuclei with magic proton numbers. *Phys. Rev. C*, 92:044307, Oct 2015.

[28] F. Wienholtz, D. Beck, K. Blaum, C. Borgmann, M. Breitenfeldt, R. B. Cakirli, S. George, F. Herfurth, J. D. Holt, M. Kowalska, S. Kreim, D. Lunney, V. Manea, J. Menéndez, D. Neidherr, M. Rosenbusch, L. Schweikhard, A. Schwenk, J. Simonis, J. Stanja, R. N. Wolf, and K. Zuber. Masses of exotic calcium isotopes pin down nuclear forces. *Nature*, 498:346–349, Jun 2013.

[29] D. Steppenbeck, S. Takeuchi, N. Aoi, P. Doornenbal, M. Matsushita, H. Wang, H. Baba, N. Fukuda, S. Go, M. Honma, J. Lee, K. Matsui, S. Michimasa, T. Motobayashi, D. Nishimura, T. Otsuka, H. Sakurai, Y. Shiga, P.-A. Söderström, T. Sumikama, H. Suzuki, R. Taniuchi, Y. Utsuno, J. J. Valiente-Dobón, and K. Yoneda. Evidence for a new nuclear 'magic number' from the level structure of ^{54}Ca. *Nature*, 502:207–210, Oct 2013.

[30] W. Trinder, E. G. Adelberger, B. A. Brown, Z. Janas, H. Keller, K. Krumbholz, V. Kunze, P. Magnus, F. Meissner, A. Piechaczek, M. Pfützner, E. Roeckl, K. Rykaczewski, W.-D. Schmidt-Ott, and M. Weber. Study of the β decays of ^{37}Ca and ^{36}Ca. *Nuclear Physics A*, 620(2):191 – 213, 1997.

[31] K. Minamisono, B. R. Barquest, G. Bollen, K. Cooper, K. Hammerton, M. Hughes, P. F. Mantica, D. J. Morrissey, R. Ringle, J. A. Rodriguez, C. A. Ryder, D. M. Rossi, S. Schwarz, R. Strum, C. Sumithrarachchi, and D. Tarazona. Commissioning of the collinear laser spectroscopy facility BECOLA at NSCL/MSU. *Hyperfine Interactions*, 230(1):57–63, Apr 2015.

[32] D. M. Rossi, K. Minamisono, B. R. Barquest, G. Bollen, K. Cooper, M. Davis, K. Hammerton, M. Hughes, P. F. Mantica, D. J. Morrissey, R. Ringle, J. A. Rodriguez, C. A. Ryder, S. Schwarz, R. Strum, C. Sumithrarachchi, D. Tarazona, and S. Zhao. A field programmable gate array-based time-resolved scaler for collinear laser spectroscopy with bunched radioactive potassium beams. *Review of Scientific Instruments*, 85(9):093503, 2014.

[33] D. J. Morrissey, B. M. Sherrill, M. Steiner, A. Stolz, and I. Wiedenhoever. Commissioning the A1900 projectile fragment separator. *Nuclear Instruments and Methods in Physics Research Section B: Beam Interactions with Materials and Atoms*, 204:90 – 96, 2003. 14th International Conference on Electromagnetic Isotope Separators and Techniques Related to their Applications.

[34] K. Cooper, C .S. Sumithrarachchi, D. J. Morrissey, A. Levand, J. A. Rodriguez, G. Savard, S. Schwarz, and B. Zabransky. Extraction of thermalized projectile fragments from a large volume gas cell. *Nuclear Instruments and Methods in Physics Research Section A: Accelerators, Spectrometers, Detectors and Associated Equipment*, 763:543 – 546, 2014.

[35] J. Äystö. Development and applications of the IGISOL technique. *Nuclear Physics A*, 693(1):477 – 494, 2001. Radioactive Nuclear Beams.

[36] A. J. Miller, K. Minamisono, A. Klose, D. Garand, C. Kujawa, J. D. Lantis, Y. Liu, B. Maaß, P. F. Mantica, W. Nazarewicz, W. Nörtershäuser, S. V. Pineda, P.-G. Reinhard, D. M. Rossi, F. Sommer, C. Sumithrarachchi, A. Teigelhöfer, and J. Watkins. Proton superfluidity and charge radii in proton-rich calcium isotopes. *Nature Physics*, 15:432–436, Feb 2019.

[37] A. Klose, K. Minamisono, A. J. Miller, B. A. Brown, D. Garand, J. D. Holt, J. D. Lantis, Y. Liu, B. Maaß, W. Nörtershäuser, S. V. Pineda, D. M. Rossi, A. Schwenk, F. Sommer, C. Sumithrarachchi, A. Teigelhöfer, and J. Watkins. Ground-state electromagnetic moments of ^{37}Ca. *Phys. Rev. C*, 99:061301, Jun 2019.

[38] P. Campbell, H. L. Thayer, J. Billowes, P. Dendooven, K. T. Flanagan, D. H. Forest, J. A. R. Griffith, J. Huikari, A. Jokinen, R. Moore, A. Nieminen, G. Tungate, S. Zemlyanoi, and J. Äystö. Laser spectroscopy of cooled zirconium fission fragments. *Phys. Rev. Lett.*, 89:082501, Aug 2002.

[39] A. Nieminen, P. Campbell, J. Billowes, D. H. Forest, J. A. R. Griffith, J. Huikari, A. Jokinen, I. D. Moore, R. Moore, G. Tungate, and J. Äystö. Cooling and bunching of ion beams for collinear laser spectroscopy. *Nuclear Instruments and Methods in Physics Research Section B: Beam Interactions with Materials and Atoms*, 204:563 – 569, 2003.

14th International Conference on Electromagnetic Isotope Separators and Techniques Related to their Applications.

[40] C. A. Ryder, K. Minamisono, H. B. Asberry, B. Isherwood, P. F. Mantica, A. J. Miller, D. M. Rossi, and R. Strum. Population distribution subsequent to charge exchange of 29.85 keV Ni^+ on sodium vapor. *Spectrochimica Acta Part B*, 113:16–21, 2015.

[41] A. Kramida, Ralchenko, Yu., J. Reader, and NIST ASD Team. NIST Atomic Spectra Database (ver. 5.6.1), [Online]. Available: `https://physics.nist.gov/asd` National Institute of Standards and Technology, Gaithersburg, MD., 2018.

[42] National Nuclear Data Center, information extracted from the NuDat 2 database, `http://www.nndc.bnl.gov/nudat2/`, accessed in 2019.

[43] See `http://www.brocktoneo.com` for information on the laser-power controller., accessed in 2016.

[44] B. R. Barquest. *An advanced ion guide for beam cooling and bunching for collinear laser spectroscopy of rare isotopes*. PhD thesis, Michigan State University, 2014.

[45] B. R. Barquest, Bollen G., Mantica P. F., Minamisono K., Ringle R., Schwarz S., and Sumithrarachchi C. S. RFQ beam cooler and buncher for collinear laser spectroscopy of rare isotopes. *Nuclear Instruments and Methods in Physics Research Section A: Accelerators, Spectrometers, Detectors and Associated Equipment*, 866:18 – 28, 2017.

[46] S. L. Kaufman. High-resolution laser spectroscopy in fast beams. *Optics Communications*, 17(3):309 – 312, 1976.

[47] W. H. Wing, G. A. Ruff, W. E. Lamb, and J. J. Spezeski. Observation of the infrared spectrum of the hydrogen molecular ion Hd^+. *Phys. Rev. Lett.*, 36:1488–1491, Jun 1976.

[48] C. Shi, F. Gebert, C. Gorges, S. Kaufmann, W. Nörtershäuser, B. K. Sahoo, A. Surzhykov, V. A. Yerokhin, J. C. Berengut, F. Wolf, J. C. Heip, and P. O. Schmidt. Unexpectedly large difference of the electron density at the nucleus in the $4p\,{}^2\mathrm{P}_{1/2,3/2}$ fine-structure doublet of Ca^+. *Applied Physics B*, 123(1):2, Dec 2016.

[49] A. Belafhal. The shape of spectral lines: Widths and equivalent widths of the Voigt profile. *Optics Communications*, 177(1):111 – 118, 2000.

[50] P. Thompson, D. E. Cox, and J. B. Hastings. Rietveld refinement of Debye–Scherrer synchrotron X-ray data from Al_2O_3. *Journal of Applied Crystallography*, 20(2):79–83, Apr 1987.

[51] A. L. Stancik and E. B. Brauns. A simple asymmetric lineshape for fitting infrared absorption spectra. *Vibrational Spectroscopy*, 47:66–69, 2008.

[52] R. F. Garcia Ruiz, M. L. Bissell, K. Blaum, N. Frömmgen, M. Hammen, J. D. Holt, M. Kowalska, K. Kreim, J. Menéndez, R. Neugart, G. Neyens, W. Nörtershäuser, F. Nowacki, J. Papuga, A. Poves, A. Schwenk, J. Simonis, and D. T. Yordanov. Ground-state electromagnetic moments of calcium isotopes. *Phys. Rev. C*, 91:041304, Apr 2015.

[53] F. Arbes, M. Benzing, Th. Gudjons, F. Kurth, and G. Werth. Precise determination of the ground state hyperfine structure splitting of ^{43}Ca II. *Zeitschrift für Physik D Atoms, Molecules and Clusters*, 31(1):27–30, Mar 1994.

[54] O. Lutz, A. Schwenk, and A. Uhl. Nuclear magnetic resonance studies of ^{4}3Ca. *Zeitschrift für Naturforschung A*, 28:1534–1536, Sep 1973.

[55] B. K. Sahoo. Nuclear quadrupole moment of ^{43}Ca and hyperfine-structure studies of its singly charged ion. *Phys. Rev. A*, 80:012515, Jul 2009.

[56] K. Matsuta, T. Onishi, M. Fukuda, T. Minamisono, H. Akai, M. Sasaki, T. Yamaguchi, T. Miyake, K. Sato, K. Minamisono, F. Ohsumi, Y. Muramoto, S. Oui, C. Ha, K. Tanaka, K. Kidera, A. Morishita, A. Kitagawa, M. Torikoshi, M. Kanazawa, T. Nishio, S. Koda, T. Ohtsubo, S. Fukuda, Y. Nojiri, S. Momota, A. Ozawa, K. Yoshida, T. Suzuki, T. Kobayashi, I. Tanihata, S. S. Hanna, J. R. Alonso, G. F. Krebs, and T. J. M. Symons. Electromagnetic moments of short lived β emitters ^{21}F,^{23}Mg, ^{27}Si and ^{39}Ca. *Hyperfine Interactions*, 120(1):673–677, Sep 1999.

[57] T. Minamisono, J. W. Hugg, D. G. Mavis, T. K. Saylor, H. F. Glavish, and S. S. Hanna. Measurement of the magnetic moment of ^{39}Ca by use of a polarized proton beam and NMR detection. *Physics Letters B*, 61(2):155 – 157, 1976.

[58] W. Nörtershäuser, R. Sánchez, G. Ewald, A. Dax, J. Behr, P. Bricault, B. A. Bushaw, J. Dilling, M. Dombsky, G. W. F. Drake, S. Götte, H.-J. Kluge, Th. Kühl, J. Lassen, C. D. P. Levy, K. Pachucki, M. Pearson, M. Puchalski, A. Wojtaszek, Z.-C. Yan, and C. Zimmermann. Isotope-shift measurements of stable and short-lived lithium isotopes for nuclear-charge-radii determination. *Phys. Rev. A*, 83:012516, Jan 2011.

[59] C. Shi, F. Gebert, C. Gorges, S. Kaufmann, W. Nörtershäuser, B. K. Sahoo, A. Surzhykov, V. A. Yerokhin, J. C. Berengut, F. Wolf, J. C. Heip, and P. O. Schmidt.

Unexpectedly large difference of the electron density at the nucleus in the $4p\,^2\mathrm{P}_{1/2,3/2}$ fine-structure doublet of Ca^+. *Applied Physics B*, 123(1):2, Dec 2016.

[60] W. H. King. Comments on the article “Peculiarities of the isotope shift in the samarium spectrum”. *J. Opt. Soc. Am.*, 53(5):638–639, May 1963.

[61] I. Angeli. Table of nuclear root mean square charge radii. *IAEA Nuclear Data Section*, INDC(HUN)–033, 1999.

[62] E. G. Nadjakov, K. P. Marinova, and Y. P. Gangrsky. Systematics of nuclear charge radii. *Atomic Data and Nuclear Data Tables*, 56(1):133 – 157, 1994.

[63] I. Angeli. A consistent set of nuclear rms charge radii: Properties of the radius surface $R(N, Z)$. *Atomic Data and Nuclear Data Tables*, 87(2):185 – 206, 2004.

[64] L. Vermeeren, P. Lievens, R. E. Silverans, U. Georg, M. Keim, A. Klein, R. Neugart, M. Neuroth, F. Buchinger, and the ISOLDE Collaboration. The mean square nuclear charge radius of $^{39}\mathrm{Ca}$. *Journal of Physics G: Nuclear and Particle Physics*, 22(10):1517–1520, Oct 1996.

[65] A. Klein, B. A. Brown, U. Georg, M. Keim, P. Lievens, R. Neugart, M. Neuroth, R. E. Silverans, L. Vermeeren, and the ISOLDE Collaboration. Moments and mean square charge radii of short-lived argon isotopes. *Nuclear Physics A*, 607(1):1 – 22, 1996.

[66] M. Bender, P.-H. Heenen, and P.-G. Reinhard. Self-consistent mean-field models for nuclear structure. *Rev. Mod. Phys.*, 75:121–180, Jan 2003.

[67] S. A. Fayans, S. V. Tolokonnikov, E. L. Trykov, and D. Zawischa. Nuclear isotope shifts within the local energy-density functional approach. *Nuclear Physics A*, 676(1):49 – 119, 2000.

[68] R. M. Dreizler and E. K. U. Gross. *Density Functional Theory: An Approach to the Quantum Many-Body Problem.* Springer Berlin Heidelberg, 2012.

[69] P. Klüpfel, P.-G. Reinhard, T. J. Bürvenich, and J. A. Maruhn. Variations on a theme by Skyrme: A systematic study of adjustments of model parameters. *Phys. Rev. C*, 79:034310, Mar 2009.

[70] D. Vautherin and D. M. Brink. Hartree-Fock calculations with Skyrme’s interaction. I. Spherical nuclei. *Phys. Rev. C*, 5:626–647, Mar 1972.

[71] J. Dobaczewski, W. Nazarewicz, T. R. Werner, J. F. Berger, C. R. Chinn, and J. Dechargé. Mean-field description of ground-state properties of drip-line nuclei: Pairing and continuum effects. *Phys. Rev. C*, 53:2809–2840, Jun 1996.

[72] N. Hinohara and W. Nazarewicz. Pairing Nambu-Goldstone modes within nuclear density functional theory. *Phys. Rev. Lett.*, 116:152502, Apr 2016.

[73] M. Hammen, W. Nörtershäuser, D. L. Balabanski, M. L. Bissell, K. Blaum, I. Budinčević, B. Cheal, K. T. Flanagan, N. Frömmgen, G. Georgiev, Ch. Geppert, M. Kowalska, K. Kreim, A. Krieger, W. Nazarewicz, R. Neugart, G. Neyens, J. Papuga, P.-G. Reinhard, M. M. Rajabali, S. Schmidt, and D. T. Yordanov. From calcium to cadmium: Testing the pairing functional through charge radii measurements of $^{100-130}$Cd. *Phys. Rev. Lett.*, 121:102501, Sep 2018.

[74] C. Gorges, L. V. Rodríguez, D. L. Balabanski, M. L. Bissell, K. Blaum, B. Cheal, R. F. Garcia Ruiz, G. Georgiev, W. Gins, H. Heylen, A. Kanellakopoulos, S. Kaufmann, M. Kowalska, V. Lagaki, S. Lechner, B. Maaß, S. Malbrunot-Ettenauer, W. Nazarewicz, R. Neugart, G. Neyens, W. Nörtershäuser, P.-G. Reinhard, S. Sailer, R. Sánchez, S. Schmidt, L. Wehner, C. Wraith, L. Xie, Z. Y. Xu, X. F. Yang, and D. T. Yordanov. Laser spectroscopy of neutron-rich tin isotopes: A discontinuity in charge radii across the $N = 82$ shell closure. *Phys. Rev. Lett.*, 122:192502, May 2019.

[75] M. Bao, Y. Lu, Y. M. Zhao, and A. Arima. Predictions of nuclear charge radii. *Phys. Rev. C*, 94:064315, Dec 2016.

[76] A. Gade and B. M. Sherrill. NSCL and FRIB at Michigan State University: Nuclear science at the limits of stability. *Physica Scripta*, 91(5):053003, Apr 2016.